Characterisation of materials under thermal and electrical stimuli using in-situ electron microscopy and MEMS technology

TCD School of Physics
Author: Cathal Mc Auley
Supervisor: Prof. Valeria Nicolosi

Declaration of Authorship

I, Cathal Mc Auley, declare that this thesis titled, " Characterisation of materials under thermal and electrical stimuli using in-situ electron microscopy and MEMS technology" and work presented in it are my own.

I declare that this thesis has not been submitted as an exercise for a degree at this or any other university and it is entirely my own work.

I agree to deposit this thesis in the University's open access institutional repository or allow the Library to do so on my behalf, subject to Irish Copyright Legislation and Trinity College Library conditions of use and acknowledgement.

Signed Date

Abstract

To incorporate nanomaterials into functional devices we need to fully understand the materials characteristics. This includes electrical, optical, mechanical and most important for us the thermal properties. The focus of my work is developing techniques to allow the *in-situ* electron microscopy characterisation of materials for the Prof Nicolosi group in CRANN. In this thesis I am presenting my work describing some new and novel techniques to characterise and synthesise nanomaterials.

I will demonstrate new methods to characterise the physical properties and characteristics of the Micro Electro Mechanical Systems (MEMS) heating chip during heating experiments, I will show how a MEMS heating chip can be modified by circuit edit using Focused Ion Beam (FIB) to enable electrical measurements *in-situ* in Scanning Electron Microscope (SEM) and Transmission Electron Microscope (TEM). I will outline a new novel technique for lamella fabrication and the transfer of the lamella to the MEMS heating chip to enable heating experiments on thin films.

Developing controlled and reproducible material synthesis techniques have become a major goal, where the nanoscale dimensions and morphology directly determine the properties of the materials. This thesis details my work characterizing materials such as Black Phosphorus (BP) and Lead Oxide (PbO) under thermal and electrical stimuli using *in-situ* electron microscopy and MEMS technology.

Keywords

Micro Electro Mechanical Systems
Transmission Electron Microscope
In-situ electron microscopy
Nanomaterials

Acknowledgements

I would like to thank my project supervisor Prof. Valeria Nicolosi for providing me the opportunity to pursue a Masters by research. Over the last few years, she has given me so much support and guidance with my work which I am very grateful. I would like to thank Dr. Eoin Mc McCarthy, Mr. Dermot Daly, Mr. Clive Downing, Mr. Keith Boland, Dr. Clodagh Dooley, Dr. Dileep Krishnan, Dr. Andrés Seral-Ascaso, Dr. João Coelho, Mr. Stephen Porter, Ms. Megan Canavan, and Dr. Edmund Long for my training and support especially FIB / TEM support and characterisation. All the other Valerians and friends for their support and advice on this journey. Finally, by no way least I would like to thank my wonderful wife Martina and beautiful children Luke, Killian, and Laoise who have always been there for me.

Contents

Table of Figures

Table of Tables

Introduction

In-situ heating experiments in Transmission Electron Microscope (TEM) and Scanning Electron Microscope (SEM) enable real-time observations of thermally activated processes such as the evolution of stress in thin films [1] recrystallization processes [2], abnormal grain growth [3], inter diffusion [4] dislocation propagation [5] and *in-situ* material synthesis [6] .

However, until now most TEM specimens used for *in-situ* experiments have been 3 mm diameter samples prepared by conventional preparation techniques or by means of drop casting the sample in solution onto a TEM grid. These dispersions directly onto the TEM grid are difficult to control and tend not to be very repeatable. Such specimens geometries and lack of process control make *in-situ* heating experiments very challenging. As both of these preparation techniques require the entire 3mm sample to be heated during analysis, it is difficult to accurately control the heating at the test specimen. The heating of the entire sample also results in sample drift during analysis due to the thermal expansion of the sample holder.

Preliminary experiments in the furnace type heating stage in SEM resulted in a number of these issues. Although water cooling was used to mitigate excessive heating of the specimen stage, it became very difficult to balance heating power and cooling rate to set an equilibrium temperature.

Recent developments in Micro Electro Mechanical Systems (MEMS) based heating stages opens new opportunities for easy fast and reliable *in-situ* heating experiment [7][8]. Furthermore this MEMS technology can be enhanced by Focus Ion Beam (FIB) circuit edit to allow electrical measurement, contacting of materials using electron beam and ion beam deposition using FIB.

However approaches for TEM specimen preparation for MEMS have not been fully optimized. Here we report on developments in the fabrication of TEM specimens for *in-situ* heating experiments using MEMS based heating system and demonstrate how the MEMS can be modified to enable electrical testing in SEM and TEM. We illustrate the development of novel specimen preparation methods developed and present results obtained from lead oxide (PbO) thin film deposited on a strontium titanate (STO) substrate by pulsed laser deposition.

1.1 Two Dimensional Materials

In this thesis, two dimensional (2D) materials are broadly defined to include multilayers, hetero-structures, nano-flakes, nano-sheets and layered thin films whose total thickness vary from an atomic layer to tens of nanometers.

2D materials have applications in a wide variety of areas from electronic devices to catalysis, and from information storage to medicine. There is a large array of 2D materials now being researched following on from the isolation of graphene in 2004 [9]. With such a multitude of materials available, conducting, insulating and semiconducting materials monolayers comprising of single elements such as phosphorene, borophene, germanene and silicene are currently being investigated. Other 2D materials feature different atoms alternating in the same layer some examples include boron nitride, transitions metal dichalcogenides (TMDs) and MXenes. The combination of 2D layers into van der Waals heterostructures in which different monolayers are freely mixed and matched further expand the opportunities for exploring new physics and applications [10]. Electronics applications are at the forefront of most researchers work with 2D materials such as graphene because of the exceptional electron mobility. 2D materials have great potential as Field Effect Transistors (FET) channels because of their high carrier mobilities but also their large on/off ratios at low voltages they also enable the miniaturisation of FETs. Other 2D materials applications draw on the charge of the electron to encode information and spin-electronics, which leverages the spin in electrons. Valleytronics is also emerging as a way to exploit the valley degree of freedom which specifies the energy extrema, or valleys that an electron occupies to store and process information in 2D layers, the valley pseudospin can be addressed both optically and electronically to realise devices. However there is more to 2D materials than electronic devices. Graphene and more generally carbon based materials are being actively pursued as low cost efficient catalysis for clean energy production and storage. Their performance rivals that of their metal based counterparts which are costly and have relatively poor stability[11].

A new material phosphorene has recently gain a lot of interest, monolayers of black phosphorous which have anisotropic lattice that differentiates this material from other 2D materials were first synthesised in 2014 are attracting considerable interest because of its excellent carrier motilities and high optical and UV absorption [12]. Some of the properties predicated for phosphorene such as super conductivity still await experimental verification, however high performance devices such as FETs and photodetectors have already being demonstrated. Some other new 2D materials which have been reported even more recently such as borophene which has recently been isolated, which is bendable and stretchable and may be applicable in flexible electronics [13].

2D materials continues to be studied due to the wealth of unusual physical phenomena that occur when charge and heat transfer is confined to a plane.

Recently new methods for synthesising, transferring, detecting, characterising and manipulating the properties of layered van der Waals materials have been demonstrated [14]. Furthermore novel synthetic methods including topotactic solution based, solvothermal and UHV surface epitaxial approaches have unleashed the potential to create new van der Waals solids and single layer thick materials. Many materials that had been initially considered to exist only in the realm of theory have been synthesised. These groups IV and II- VI semiconductors analogues of graphene/ graphene (the sp^2/ H terminated sp^3 derivatives) such as silicence [15] and germanane [16] have been reported. These materials similar to graphene show distinct differences between the material in its bulk form and in a single layer. These newly synthesized materials are useful building blocks that can be restacked and integrated into composites for a wide range of applications.

1.2 Structure and Synthesis of two-dimensional materials

The ability to synthesise single layer and few layer 2D materials is an essential first stop to enable the characterization of layer dependent changes, their physical properties, as well as providing information to enable these materials to be integrated into multiple applications. In general there are three main classes of materials that can be prepared as a single atom or single polyhedral thick layer.

1.2.1 Layered van der Waals solids

These are the most common class of crystalline structures that can be exfoliated as stable single layers. The crystal structure of these materials feature neutral single atom thick or polyhedral thick layers of atoms that are covalently or ironically connected with their neighbouring atoms within each layer, layers are held together via van der Waals bonding along the third axis. The weak van der Waals energies (~40 -70 meV) enable the facile exfoliation of these layers. The most common approaches for obtaining single and few layer thick 2D materials from these solids is by mechanical exfoliation using "scotch tape", chemical exfoliation by dispersion in a solvent with the appropriate surface tension and molecule/ atom intercalation in order to exfoliate these layers and enable their dispersions in polar solvents. These mechanical exfoliation processes have been used to prepare and study the properties of few layer van der Waals materials, such as MoS_2 and $NbSe_2$, since the 1960 [17] . The isolation of individual and few layers using mechanical exfoliation remains the most powerful approach for studying the materials properties due to the fact it is less destructive than other methods and can create large single layer flakes (10µm) on a variety of substrates.

1.2.2 Layered ionic solids

The second class of material that can be prepared as single or a few layers are solids that feature bulk crystal structures with charged 2D polyhedral layers that are typically held together with strong electro positive cations or strongly electronegative anions such as halides or OH^-. To enable their dispersion as single layers in solution, these cations \ anions are typically exchanged with bulky organic cations \ anions, such as tetrabutylammonium\dodecyl sulfate. These materials can then be easily dispersed onto substrates, with the majority of materials depositing as single to a few layers. Typical examples of these materials are layered double hydroxides such as Al−NO3, Zn2Al−NO3, Ca2Al−Cl, LiAl2−NO3, Zn2Cr−NO3, and Ni2Al−NO3.

1.2.3 Surface Growth of Non-layer material

The deposition of material on substrates offers the potential to grow and study the properties of a single to a few atoms thick materials beyond those existing as layered bulk crystals.

1.2.3.1 Solution – Phase growth

Solution – phase metal such as solvothermal or colloidal growth reactions offer a facile production method to synthesis gram scale quantities of 2D materials with precise thicknesses and basal–plane sizes[18] . In monoclinic, rhombohedral, tetragonal, and trigonal/hexagonal systems there is one unique axis (sometimes called the principal axis) which has higher rotational symmetry than the other two axes. The basal plane is the plane perpendicular to the principal axis in these crystal systems. The crystal structure and symmetry play a critical role in determining many physical properties, such as cleavage, electronic band structure, and optical transparency.

A solvothermal process can be defined as a process in a closed reaction vessel inducing a decomposition or a chemical reaction(s) between precursor(s) in the presence of a solvent at a temperature higher than the boiling temperature of this solvent.

Current synthetic strategies for nano-sheets primarily focus on solution-based processes, such as solvothermal reactions. However, the solution-produced nano-sheet may have solvent residues adsorbed at the surface that are difficult to remove and can substantially modify the nano-sheet's intrinsic properties.

1.2.3.2 Vapour Deposition

Vapour Deposition stand as an appealing versatile synthetic strategy. However the development of a controlled synthetic method of producing 2D material such as 2D chalcogenides by vapour deposition requires a better understanding of the fundamentals involved. While vapour deposition has been extensively used for the growth of thin films and nanomaterials [19], nanotubes[20] and graphene[21], knowledge obtained from these materials may not simply be apply to 2D materials. Unlike typical nanomaterial whose growth is primary governed a catalyst, the vapour deposition of 2D chalcogenides is often non-catalytic[22] . Without the dominance of catalysts the growth of 2D nano-sheets is subject to strong influences of many experimental parameters that may play only a negligible role in catalytic growths. For example, the diffusion of source material vapour through the gas flow boundary layer strongly controls the vapour deposition growth of GeS nano-sheets. This boundary layer diffusion is found to be the rate-determining step of the growth under typical experimental conditions, evidenced by a substantial dependence of the nano-sheet's size on diffusion fluxes. It has also been shown that high quality GeS nano-sheets can grow only in the diffusion-limited regime, as the crystalline quality substantially deteriorates when the rate-determining step is changed away from the boundary layer diffusion[23]. The growth of single layer substrate wide 2D materials is essential for commercialisation [24].

1.3 Characterisation of two dimensional materials

Probing the molecular and vibrational structure of 2D material is inherently challenging due to the small sample size. However, numerous methods have been developed to enable their identification and characterisation. The first challenge in single–layer characterisation is single layer preparation and detection. Optical microscopy is initially the most powerful high throughput method for identifying single and multiple-layer flakes[25]. Fluorescence Quenching Microscopy (FQM) uses an organic fluorophore whose fluorescence is quenched in the presence of single or few layer sheets. Many 2D materials feature either low enough band gaps or the appropriate band alignment to quench nearby fluorophores via FRET mechanism or charge mechanism. One can locate a single layer of 2D materials on a substrate by monitoring the reduction in fluorescence intensity of a thin fluorophore layer that was spun coat on top[26]. Atomic Force Microscopy (AFM) is a powerful technique to determine layer thickness with a precision of 5%[27]. However discrepancies can arise from differences in the interaction of the tip with the sample substrate[28]. Raman Spectroscopy is a method for finger printing a material and detecting layer dependent changes of the vibrational structure. It is necessary to use low power when obtaining Raman spectra of single layers to prevent sample decomposition[29].

Transmission Electron Microscopy (TEM) can provide detailed information on the nature of crystallinity layer sizes, interlayer and elemental composition. Many techniques such as Selected Area Diffraction (SAD) can be used to distinguish between monolayer and multi-layer materials. The deviation in diffraction intensity can distinguish between single and multilayers when there is a change in interlayer registration[14]. Recently advances have shown that weak field dark field electron microscopy can quantitatively determine the layer number and stacking order of multilayer graphene [30]. Scanning Transmission Electron Microscopy (STEM), using high angle annular dark field detector coupled with Electron Energy Loss Spectroscopy (EELS) can be used to visualise individual atoms in an isolated layer [31]. The ability to used low accelerating voltages (< 60KeV) minimises damage [32]. A detail description of TEM is given in chapter 2.

Scanning Tunneling Microscopy (STM) is a probe based technique that can measure the electronic and topographic structure of single atom–thick materials and can manipulate single atoms at specific points in order to build and characterise nanostructures that are well resolved from the substrate. X- Ray Diffraction (XRD) both small angle X-Ray scattering (SAXS) and wide angle XRD can supply information about the unit cell structure and constituents, the sheet thickness and lateral dimensions, and the arrangement of restacked nano-sheets[33][34][35].

1.4 Characterisation Opportunities

The development and implementation of new characterisation techniques that can rapidly and non-destructively probe atomic structures, defects and properties of single layer material is necessary to advance the field. Since the electronic properties of materials are often dominated by minority defects, the discovery, availability and implementation of techniques that can identify minority species, defects and edge states, such as aberration–corrected STEM as well as STM, will prove incredibility valuable.

New opportunities now exist due to a shift from post mortem characterization to live or *in-situ* measurements of structures, chemistry and properties of nanomaterials. This shift is mainly due to the adoption of aberration correction and Micro-Electro-Mechanical Systems (MEMS) device integration.

The drive toward *in-situ* TEM is to meet the scientific challenges to understand synthesis routes, chemical activity of nanoparticles, nanoscale property measurement and observation of nanoscale failure mechanisms which in turn will lead to more productive synthesis, fabrication and structural properties relationships.

Figure 1-1(a) (b) below shows the current areas of in-situ TEM. This is a field of research that is growing year on year with new developments constantly appearing in the MEMS fabrication, *in-situ* TEM holder designs. This is also reflected in the exponential growth in the number of publications in recent years as shown in figure 1-2 and the fact that each major materials related conference has at least one session related to *in-situ* TEM[36].

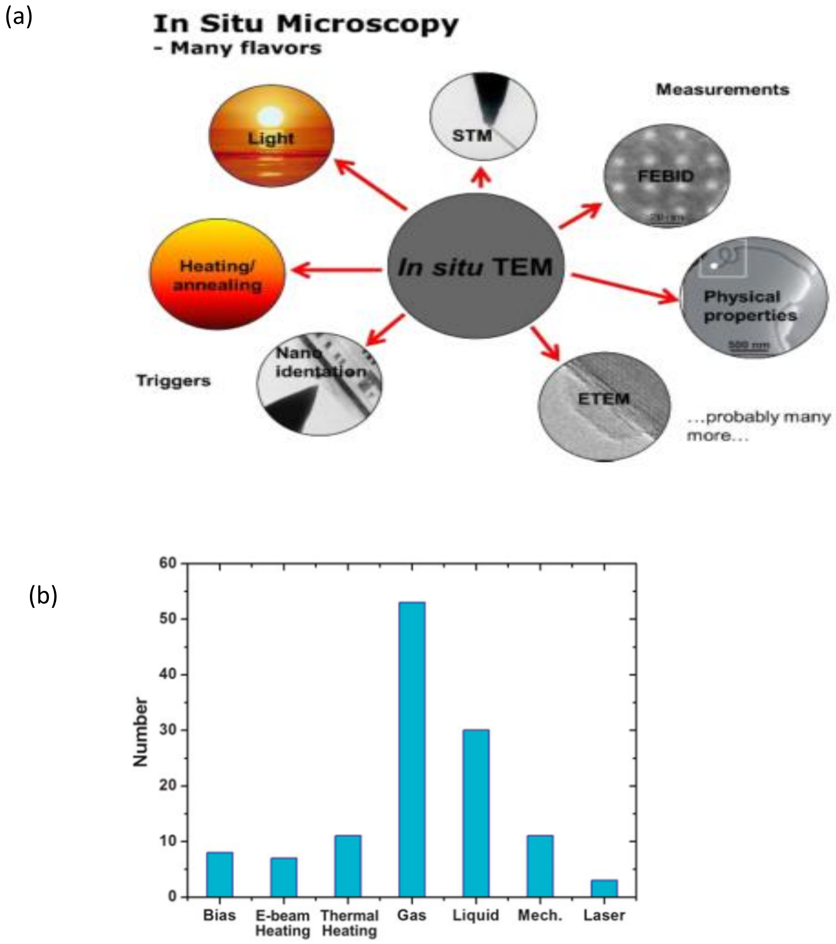

Figure 0-1(a) External stimuli currently used for in-situ observations on a TEM platform[37] *(b) breakdown of the various sub categories of in-situ papers presented at the Microscopy and Micro analysis conference USA 2012 and the European Microscopy and Microanalysis conference (UK)*[37]*. These subcategories are in-situ electrical biasing, electron beam heating, Thermal heating, gaseous environmental, liquid environment, mechanical loading and laser stimulation.*

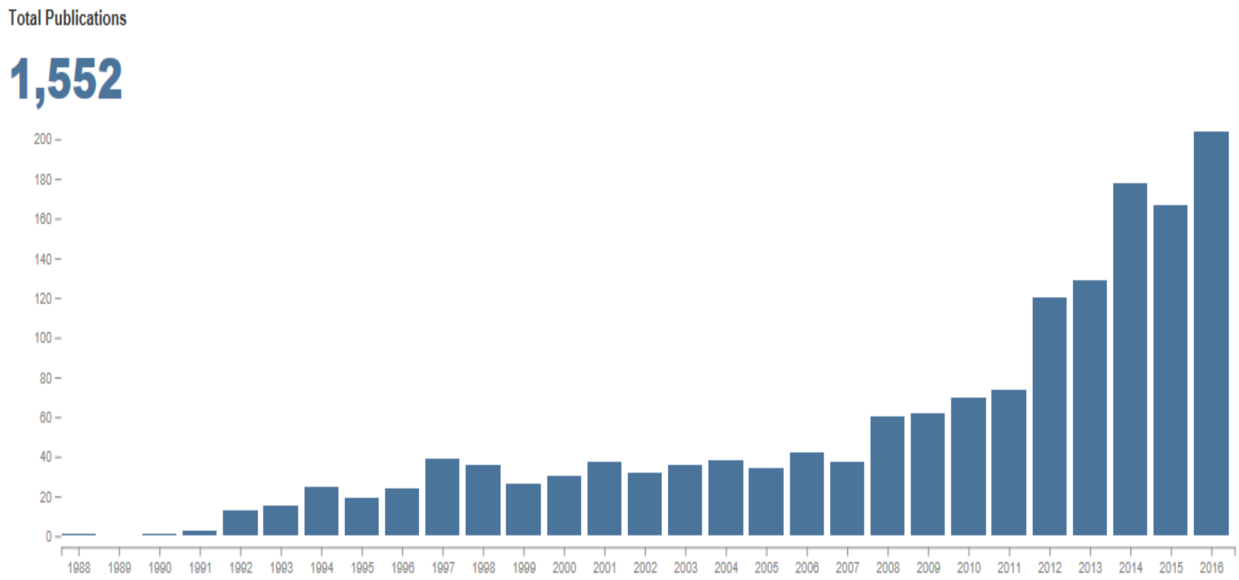

Figure 0-2 The growth in numbers of publications during 1988 and 2016 identified using keyword ''in-situ TEM''[38]

For successful in-situ measurements the key requirement is the base unit TEM / STEM as discussed in chapter 2 which combines high spatial and spectral resolution and has the capability to be interfaced with peripheral equipment. This equipment is available from a number of vendors such as Dens Solution , Proto-chips, and Humming bird which all enable *in-situ* experiments similar to those outlined in the sub categories in figure 1-1(a). In addition, there is a need for a data acquisition and processing system that can improve temporal resolution and is capable of handling large data set obtained during experiments.

1.5 *In-situ* heating in TEM

Temperature is one of the most important factors affecting the state and behavior of materials. *In-situ* heating in TEM is a powerful tool for understanding such effects and recently *in-situ* heating in TEM has made significant progress in terms of the temperature and resolution capabilities. *In-situ* heating in TEM of specimens has enabled observations of solid to solid reactions, solid to liquid reactions, (including high resolution observation of a solid–liquid interface, size dependence of the melting temperatures of one-, two- and three-dimensionally reduced systems, size dependence of the contact angle of metal liquid, and wetting of Si with liquid Au or Al) [39]. *In-situ* heating provides fundamental information on temperature effect on materials. TEM enables material observation with spatial and chemical resolution at atomic level. During *in-situ* heating TEM experiments, the samples are heated or cooled, so that these dynamic phase transformations and reactions at high temperature can be directly observed *in-situ*. One of the main limitations of *in-situ* heating TEM is the high vacuum in which the specimens are contained. Thus, traditional observations of reactions containing liquid and or gas have been difficult to carry out or have been made at the sacrifice of spatial and chemical resolution. Recently, however advancements in *in-situ* experimental holders for TEM have made significant progress and these difficulties have been overcome.

1.6 Specimen heating holders for successful *in-situ* TEM

The most important features required for *in-situ* TEM heating is the ability to reach high temperature, and good mechanical and thermal stability of the system at high temperatures. Any instability of the holder causes a drift of the specimen. In addition if the maximum heating temperature achievable by the heater is low, the application range will be limited. Therefore the design of the specimen heating holder is the most critical issue for performing *in-situ* heating for TEM experiments [39]. Chapter 3 describes in detail the Dens Solutions TEM heating holder that utilises MEMS technology use for experiments in this thesis.

2 Instrumentation and Theory

2.1 Electron Microscopy

The fundamental operation of electron microscopy relates directly back to the physics of the electron interactions with the sample. Energetic electrons are described as "ionizing radiation". This means the radiation that is able to ionize or remove the tightly bound inner shell electrons from a material. The advantage of this type of microscopy is the range of interactions which occur and the different signals which these generate: secondary, backscattered, Auger, X-ray as shown in figure 2.1. The early stages of research in electron microscopy in the 30's and 40's led to the development of two distinct groups of electron microscopy: transmission electron microscopy (TEM), which also includes scanning transmission electron microscopy (STEM) and scanning electron microscopy (SEM) [40].

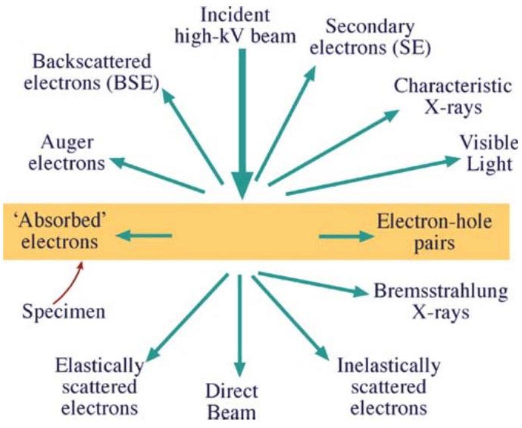

Figure 2-1 Schematic of the different signals generated when a high intensity electron beam interacts with a sample. [41]

2.2 Transmission Electron Microscopy

Electron microscopy was developed in order to create better resolving power than visible-light microscopes (VLMs). Initially TEMs were used as their resolution is much better than visible-light microscopes (VLM). It was later discovered that the TEM can be beneficial in other ways than just better resolution. From the interactions with the incoming electrons, chemical and structural information can be obtained by utilizing the different interactions happening within the sample when the high intensity electron beam passes through it as shown in figure 2-2 [41] [42].

TEM is a technique used to acquire high spatial resolution images as well as structural and spectroscopic information from electron transparent samples[41].The microscope directs a parallel beam of high energy, typically 80 – 300KeV, electrons at the sample. In order for the simplifications associated with single scattering of electrons within the sample to be valid the sample must be typically less than 100nm in thickness, but this can vary depending on the analysis required, the mass of the atoms in the material and the energy of the illuminating electron beam.

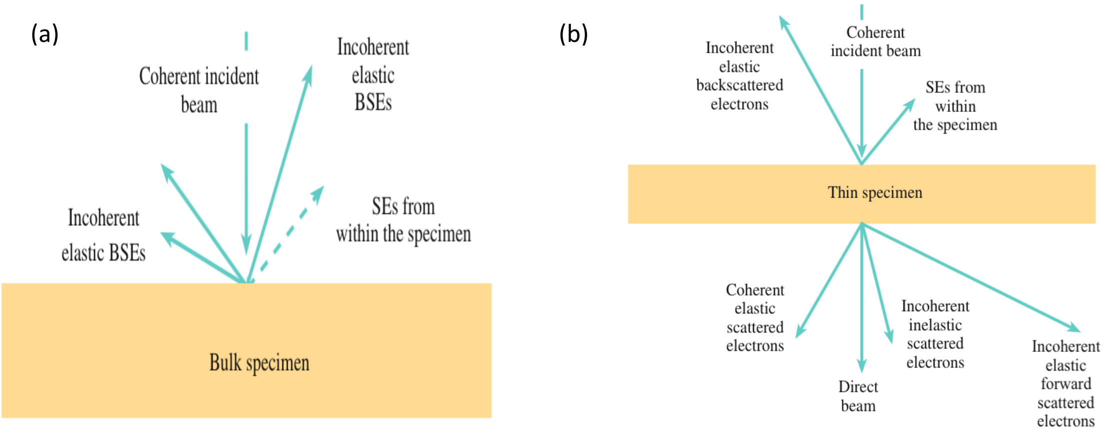

Figure 2-2 (a) Different scattering mechanisms from a bulk specimen, typically used in SEM, (b) Different scattering mechanisms for a thin, electron transparent, sample typically used in TEM. [41]

2.3 Imaging

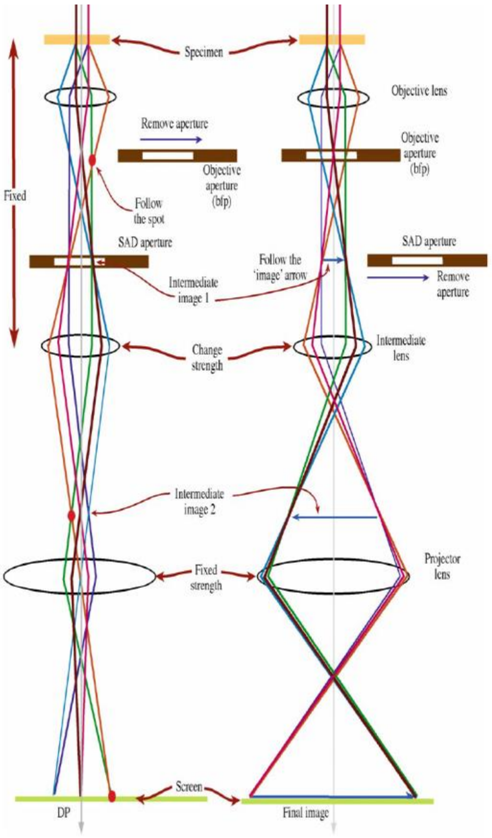

Figure 2-3 *Schematic showing diffraction and imaging mode of TEM* [41]

The TEM instrument contains 3 main sections: the illumination system, the objective lens/stage and the imaging system.

The illumination system consists of the gun and the condenser lenses. This system can be operated in two different modes: parallel beam or convergent beam. Parallel beam refers to traditional TEM mode and convergent refers to Scanning Transmission Electron Microscopy (STEM). In parallel mode, the most commonly used mode of TEM, uses its array of electromagnetic lenses to create a parallel beam of electrons, which pass through the sample (transmit). This electron beam collides with the electron transparent sample (<100 nm) and numerous interactions occur. There are both elastic, inelastic collisions, coherent, incoherent, elastic and inelastic scattering. The different types of scattering can help produce images and data containing different but often complimentary information. We can distinguish between imaging mode or diffraction mode as shown in the schematic *Figure 2-3* [41] [42].

2.4 Amplitude Contrast

As the electron wave passes through the sample its amplitude changes, this gives rise to image contrast, which is the difference in intensity between two adjacent areas. There are two types of amplitude contrast: mass-thickness contrast and diffraction contrast. The apertures in the TEM can be used to select certain transmitted beams and omit others in order to form different types of contrast. After the incident beam interacts with the sample it is transformed into a non-uniform intensity. This change in intensity translates into contrast in the image. The diffraction pattern shows this variation in intensity as it separates the direct beam from the diffract beams, which have been scattered throughout the sample. The diffraction pattern is only showing the electrons which have undergone Bragg diffraction. By using the objective aperture different beams (direct or diffracted) can be selected to create contrast within the image and highlight certain regions of the sample. This is what leads to bright and dark field imaging. In bright field (BF) imaging the high order diffracted beams are removed, meaning the more diffracted thicker material or defects appear darker. Conversely, in dark field (DF) imaging the beam is tilted so that the diffracted beam is allowed pass through the aperture. This makes the image predominantly dark with regions of diffraction appearing bright. [41]

Mass-thickness contrast is due to a difference in the thickness in regions of the sample. It arises from the incoherent elastic scattering (Rutherford scattering) of electrons. As Rutherford scattering is a strong function of the atomic number Z, it is strongly dependent on the mass of the sample and also the thickness of the specimen. In a BF image, thicker regions will appear darker and thinner brighter and vice versa for DF images. [42]

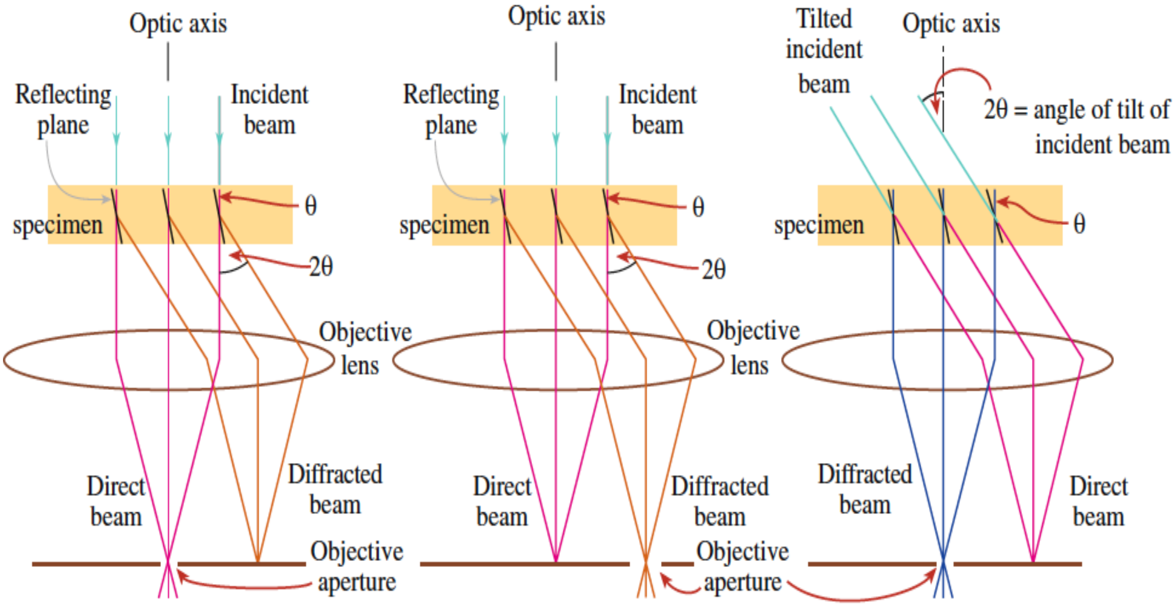

Figure 2-4 Set-up of bright and dark field imaging [41]

2.5 Phase Contrast

After passing through the sample, waves of the diffracted beam interfere with each other, creating constructive and destructive interference patterns. This leads to fringes being created, most commonly Moiré patterns. These are formed by two sets of interfering lattice fringes with nearly common periodicities. Lattice fringes are especially important to High Resolution Transmission Electron Microscopy (HRTEM) analysis as the lattice periodicity correlates to the periodicity of the crystal structure. Inserting apertures creates image contrast but at high magnification it limits the resolution significantly. Therefore to get HRTEM images, phase contrast must be used while imaging. This consists of not using an aperture or using a very large aperture and interpreting the phase of the electron waves after they have been transmitted through the sample. The sensitivity of this contrast is the reason why lattice structure can be imaged in this setting [42].

2.6 Scanning Transmission Electron Microscopy

By combining the TEM and the SEM technology, a STEM is created. STEM mode uses a convergent probe to scan across the sample point by point. The main advantage of using STEM is the Z-contrast mechanism. STEM uses annular detectors beneath the sample which can detect electrons scattered at high angles. There are 3 different types of detectors used in STEM: bright field (BF), annular dark field (ADF) and high angle annular dark field (HAADF). Z-contrast is obtained by detecting the electrons scattered at high angles, therefore the HAADF detector is used to collect these electrons and created a dark field z-contrast image. The ADF collects electrons that are both Bragg and Rutherford scattered creating a mixture of diffraction and z-contrast. The bright field detector detects the directly transmitted beam and the very low-angle (inelastic incoherently) scattered electrons. These inelastic incoherently scattered electrons are what is used in Electron Energy Loss Spectroscopy (EELS) analysis [41][42][43].

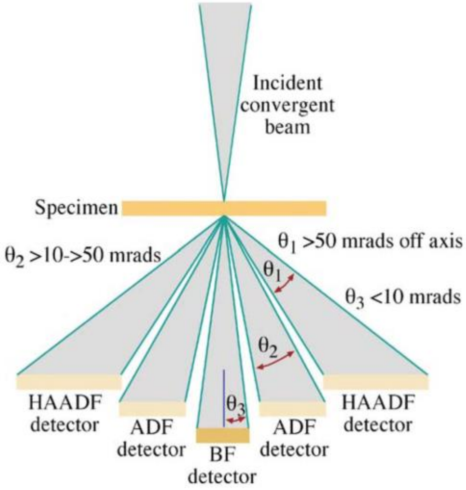

Figure 2-5 Diagram of the imaging system and detectors in STEM [42]

2.7 Electron Energy Loss Spectroscopy (EELS)

EELS requires a high energy beam of electrons with a narrow range the electrons of known kinetic energies. An electron spectrometer is then used to measure the energy loss of the electrons which undergo inelastic scattering in the sample. An electron spectrometer uses electric or magnetic fields to bend the path of incoming electrons. Electrons with higher kinetic energy pass through the spectrometer faster and are therefore deflected less. This allows us to spatially resolve electrons with different energies.

A typical EELS spectrum tell us that most of the electrons experience effectively no energy loss in a thin sample. The probability of a Plasmon excitation is relatively high, this interactions leads to a small loss of energy from the incident particle. The acquired spectrum also contains finer detail about the sample at higher energy loss ranges[44]. The incident beam can cause an inner shell ionization in the sample. The energy loss from the incident electron during this process is characteristic of the atom encountered. EELS can therefore be used to quantitatively identify sample composition, and unlike Energy Dispersive X ray analysis (EDX) it is best suited to elements with a low atomic number such as carbon. In fact EELS can even be used to distinguish the different allotropes of carbon [45][43].

2.8 Review of the applications of TEM and the influence of charged particle radiation on modifying nanostructures

TEM has been developed to a level that it can investigate the structure of material down to an atomic scale. Conventional techniques such as bright field, dark field imaging, diffraction and high resolution imaging coupled with analytical techniques such as Electron Dispersive X-ray (EDX), Electron Energy Loss Spectroscopy (EELS) and electron filtering imaging further extend the application of microscopy techniques from microstructure, crystallography, composition, to techniques that provide information about the materials electronic structure and even optical and magnetic properties from regions of the sample in the micrometer to sub nanometer range[46]. The radiation effect of the electron beam must be considered at all times when validating these results, however the radiation effect can also be applied to tailor the microstructures and hence modify the material under examination[44]. The radiation effect in charged particle microscopes is generally considered to have a damaging and negative impact on the material under observation as it is capable of introducing undesirable disorder and thus deteriorate the material, however if we control and limit the electron beam dose, beam energy we can use this effect to modify the nano-structure of materials and observe self-organization, self-assembly of materials thus locally engineering the phase transformation of materials by the simultaneous application of thermal stimuli and localized electron beam as outlined in chapter 5.

The radiation effect has also been reported to be used to tailor the mechanical [47], electronic [48] and even magnetic properties [49] of materials at atomic precision which cannot be achieved with conventional macroscopic tools.

Electron beams on field emission guns can be focused on a spot as small as 1Å which is less than the distances between atoms in materials. However it should be also noted that modifications can also be achieved by the defocusing of the beam. The limited size of the nanomaterial in one or two dimensions needs to be considered, as defect generation by charge particle irradiation differs in nano-materials compared to bulk materials due to the interactions of the electrons that can pass through low dimensional materials without inelastic scattering which in turn leads to very little energy loss opposed to bulk systems where all the energy is eventually absorbed. This means that the probability for energy loss of the incident beam is small in low dimensional materials and decreases with increasing energy resulting in low damage to the material when the particle energy is high, provided that displacement cascades do not play a considerable role [50]. This reduced dimensionality may give rise to a different temperature profile after the impact so that the local temperature may exceed the melting temperature of the material [51].

Even though TEM is considered the most powerful tool for investigating nanostructures of light element materials, it has been shown that these materials can be quite sensitive to electron beam irradiation which has resulted in misinterpretation of the structure of the material. The main primary radiation effects are:-

- Electronic excitation or ionization of individual atoms
- Collective electronic excitation such as Plasmon
- Breakage of bonds or cross linking
- Generation of phonons, leading to heating of the target
- Displacement of atoms in the bulk of the target
- Sputtering of atoms from the target

These radiation effects can be divided into those that lead to a displacement of atoms known as “knock-on effects” and alternatively radiation effects caused by “excitation”. Generally as the electron beam energy decreases the excitations increase whereas knock-on effects decreases. This gives us a strategy to minimize the knock-on damage during TEM experiments by lowering the acceleration voltage. Moreover this increases the possibilities of excitations which is the major origins of EELS spectrum, it also improves signal to noises ratios for chemical analysis. When the elastic scattering cross section increases, we note an increase in contrast of light elements in high resolution, zero-loss images. However when low-energy electron microscopy is applied to achieve the atomic resolution there is a need to use either direct or indirect aberration correction to achieve the required spatial resolution. Krivanek et al. [32] applied aberration correction STEM to reach probe sizes close to 1Å at 60KeV an operating energy that avoids direct knock on damage in materials consisting of light atoms. The results presented by Bell et al. [52] indicate that decreasing the acceleration voltage from 200KV to 80KV in a mono-chromated aberration-correction microscope enhanced the contrast while retaining sub-angstrom resolution.

Egerton et al. states that TEM can cause temporary or permanent change in the surface or bulk structure of a specimen and one way of categorizing this damage is in terms of electron scattering that gives rise to it[53] as outline in figure 2-6 .

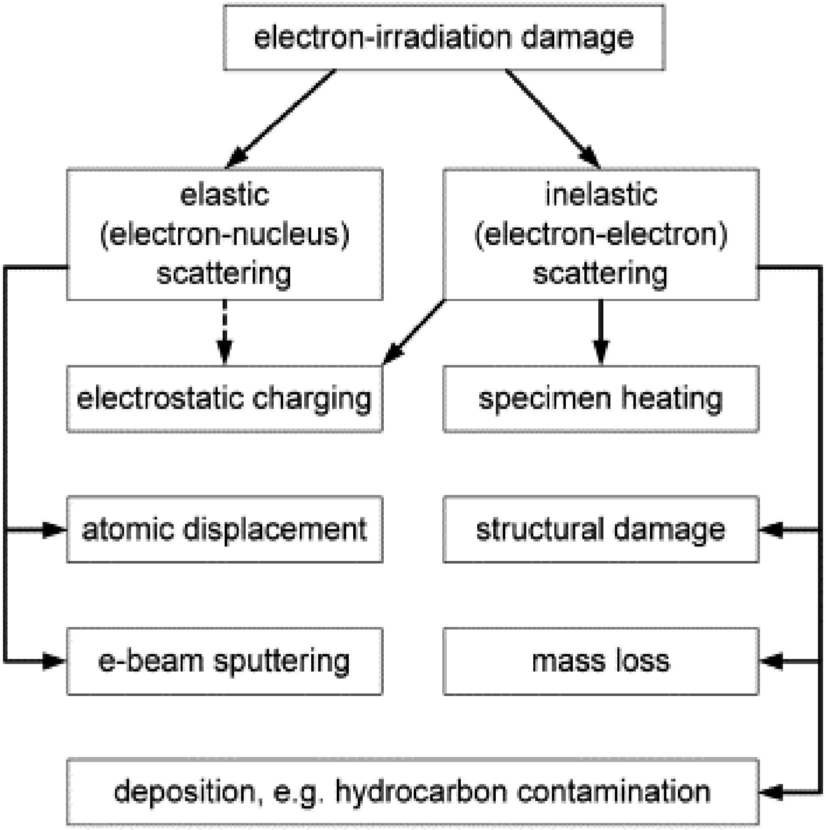

Figure 2-6 Classification of radiation damage according to the type of electron scattering and according to the effects produced in a specimen [53]

Electron scattering represents electrostatic deflection of incoming electrons by the coulomb field of each atom nucleus. This is what gives rise to electron diffraction patterns and to diffraction and phase contrast in TEM. In some circumstances elastic scattering results in atomic displacement within a crystalline specimen or electron-beam sputtering from its surface.

Inelastic scattering represents coulomb interaction of incoming electrons with atomic electrons that surround each nucleus which results in X-rays and EELS in TEM [53]. However inelastic scattering can also produce radiolysis effects, which change the structure of a specimen or remove material. Radiolysis is somewhat temperature dependent and can be reduced by cooling the sample[54].

3 *In-situ* Heating Holder

In this chapter we give an overview of the major components and performance specification of the *in-situ* heating holder under various conditions. We present our experimental data on the observed flexural distortion of the MEMS chip during heating, and detail a novel method to enable electrical testing of materials in SEM using a circuit edited modified standard heating MEMS chip.

The *in-situ* heating holder is a modified TEM sample holder that interfaces and connects between EM heater chips and a control unit to enable temperature control of the EM heater chip micro hot plate from the outside world, this holder ''Wildfire *in-situ* heating holder '' is commercial available from Den Solutions. The materials used in the manufacture of the holder have been specially selected for optimal mechanical strength, low thermal expansion and durability. The TEM holder is specifically designed to provide *in-situ* heating capabilities up to 1350 °C. It utilizes small MEMS semiconductor device (consumable) as a heater. The system is optimized to have a direct read-out of the temperature value during the experiment (independent of the heater environment) with a known reproducible distribution over the heated area for heating experiments on nanoparticles and FIB lamella.

The system can heat the specimen in S/TEM and control the temperature environment of the specimen in an accurate, fast, and reliable manner such that the full characterization power of S/TEM can be used for directly observing the structure evolutions at various temperatures.

Heating plays a significant role on the structure, properties and performance of materials. However the dynamic states of materials during heat treatments cannot always be inferred from S/TEM examination at room temperatures or from postmortem studies. Therefore direct observation of the structure evolution during the heat treatment are of the utmost importance.

The heating systems contains three major components as outlined in figure 3.1a.

(1) EM heater chips
(2) In-situ heating holder
(3) Control unit

3.1 EM-heater chips

EM heater chips are functional consumable sample carriers to replace traditional TEM copper grids. They offer additional functionality of a micro-scale hot plate which enable heating of samples. The heating principle of the micro-heater is based on Joule heating of a metal spiral. Figure 3-1(a) shows a diagram of the heating holder, figure 3-1(b) shows a SEM image of the MEMs chip. The EM heater chips are fabricated by using Micro Electro Mechanical Systems (MEMS) technology. All relevant functionality is integrated on the scale of 300µm x 300µm x 600nm, close to the scale of TEM samples.

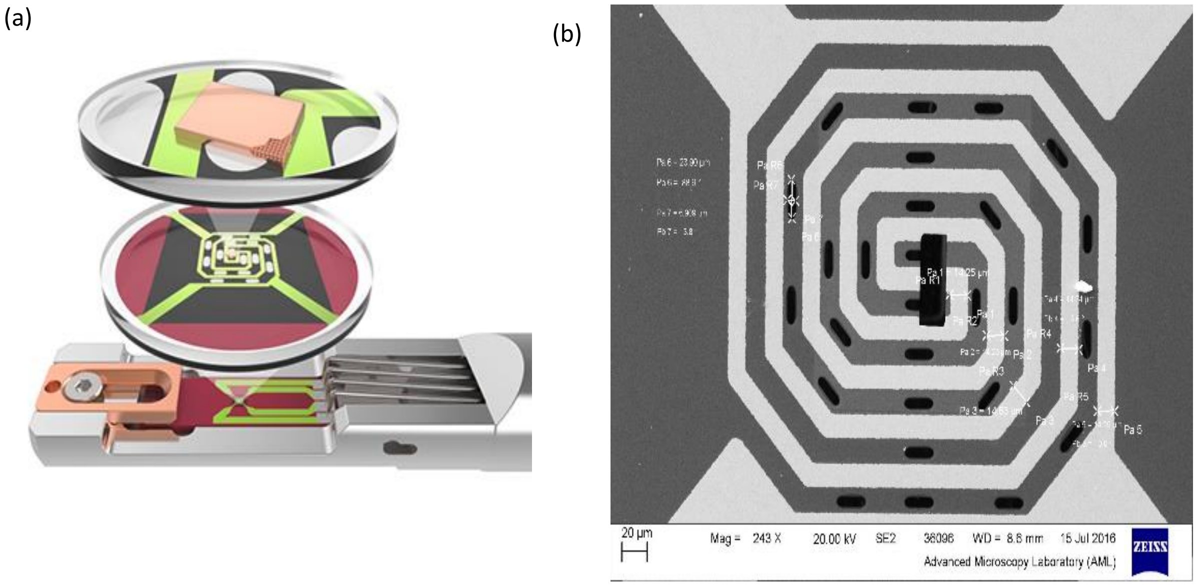

Figure 3-1(a) Diagram of the heating holder (b) SEM image of MEMs chip taken at 20KV using the secondary electron detector.

3.2 Control Unit

The plug and play control unit consist of a compact electronic regulator and graphics user interface software installed on a laptop. The regulator inputs power to heat the EM heater chip and supervises the real time temperature change. A feedback loop is constructed in the regulator to quickly within 2 seconds stabilize the fluctuations of temperature less than 10mK.The graphics software allows users to input setting temperatures digitally. The software also allows the user to program temperature versus time profile to enable auto-heating experiments. The digi-heater software provides a graphical user interface for accessing the heater control box. The control box regulates with the EM-heater via the contact between the four electrical contact pads of the heater and a resistive thermometer. Figure 3-2(a) shows a plot of the temperature of four point resistance measurement versus temperature.

(a)

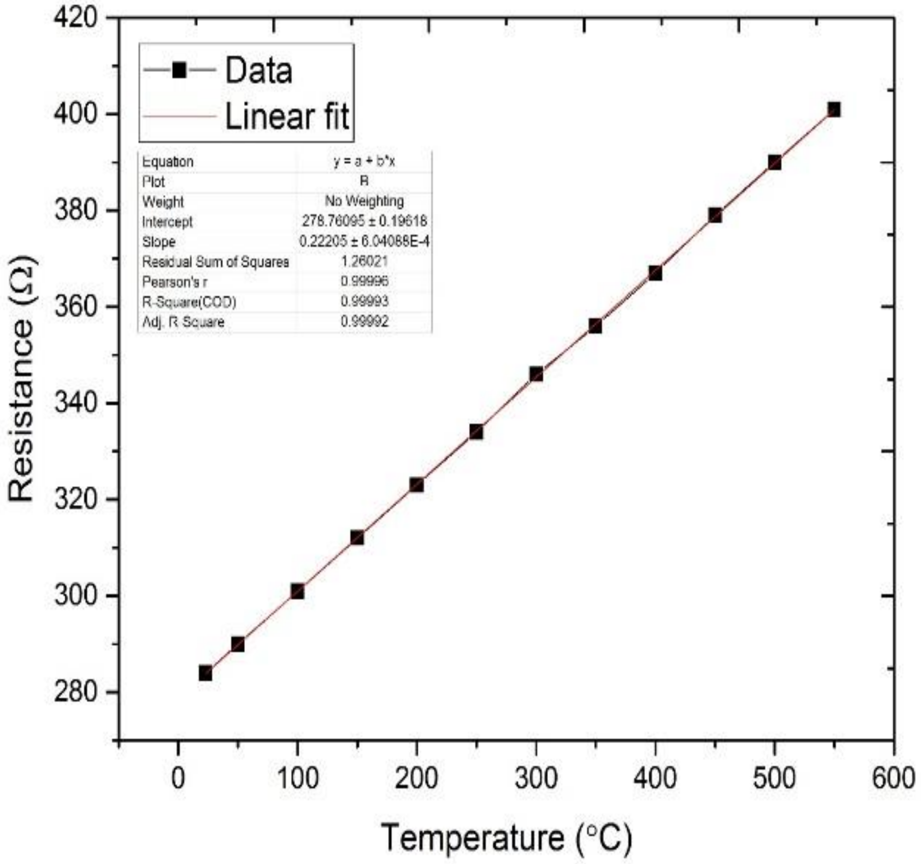

Equation	y = a + b*x
Plot	R
Weight	No Weighting
Intercept	278.76095 ± 0.19618
Slope	0.22205 ± 6.04088E-4
Residual Sum of Squares	1.26021
Pearson's r	0.99996
R-Square(COD)	0.99993
Adj. R Square	0.99992

Figure 3-2 (a) Plot of four point resistance measurement versus temperature.

The observed advantages of Dens solutions MEMS are as follows:-

- State of the art 4 point probing with continuous feedback for reliable temperature.
- Extremely fast response, reliable and reversible behavior resulting in no contamination or interference.
- 5 X 20µm electron transparent windows for experimental freedom.
- Windows are available with silicon nitride membranes less than 20nm, Carbon membranes less than 5 nm and through hole.
- Large specimen compatibility such as nanoparticles, FIB lamella, thin film.

3.3 Temperature setting and Temperature control

Once a request to set a certain temperature is sent by the software, the control box will apply a current through two of the four contacts of the spiral heater, inducing Joules heating. The voltage between the other contacts is measured in real-time and the resistance is calculated to provide the measured temperature T of the heating element according to the Callendar-Van Dusen see equation 1 below [55][56][57][58].

$$(T) = AT^2+BT+C \tag{1}$$

This equation shows a direct and well-defined relationship between resistance and temperature for a metal-based heating element above 0^oC. Based on the feedback of the measured temperature (calculated from the measured resistance), the control box adjusts its input current accordingly, to make the measured temperature match the set one. The feedback loop is running to compensate for possible temperature disturbance, such as change of gas pressure or a change to the sample.

A,B,C parameters in Callendar-Van Dusen equation of the EM-heater chip are parameters characterised by inherent property of the heater material. They are obtained from temperature-resistance calibration. A typical calibration can be firstly setting a temperature of the heater, e.g. by putting the heater chip in a furnace , then measuring the corresponding resistance of the heater, after a series of measurements A,B,C parameters are obtained based on the regression of the measured temperature resistance plot as shown in figure 3-2(a). The other way of calibration can be that applying current to enable the Joules heating of the heating chip, reading the resistance of the heater by four-point resistance measurements, and measuring the corresponding temperature using noncontact thermometry method, e.g. Raman or infrared thermometry to cross-correlate and built up the temperature–resistance relationship. The relationship between resistance (R) and temperature (T) is generated from the Callendar-van Dusen equations [56][59].

For the temperature range between -200°C to 0°C is describe by equation 2, for the temperature range 0°C to 661°C is described by equation 3.

$$R_T = R_0\{1 + AT + BT^2 - (t - 100)CT^3\} \tag{2}$$

$$R_T = R_0\{1 + AT + BT^2\} \tag{3}$$

Where R_T = Resistance at Temperature (T),

R_0 = Resistance at 0°C,

T =Temperature in °C

The constants A, B, and C are determined by the properties of the heater material in our case Molybdenum (Mo) used in the construction of the heater. The heater material is specially selected to give nominal values of the constants α, β, and δ. **The constants A, B, and C can be written as:**

- $A = \alpha \times \{1 + (\delta/100)\}$ °C^{-1}
- $B = -\alpha \times \delta \times 10^{-4}$ °C^{-2}
- $C = -\alpha \times \beta \times 10^{-8}$ °C^{-4}
- (β is equal to 0 when T is greater than zero)

$$\alpha = \frac{(R100 - R_0)}{(100\ x\ R_0)} \qquad \textbf{(4)}$$

Where (α) is the temperature coefficient of resistance obtained by measuring the heater resistance at both 0°C & 100°C as shown in equation 4, (δ) is obtained by calibration at a high temperature, for example, the freezing point of indium, tin, zinc, or aluminium (156.5985°C, 231.928°C, 419.527°C, and 660.323°C respectively), (β) is obtained by calibration at a negative temperature, for example, triple point of mercury and argon (-38.8344°C and -189.3442°C respectively) or liquid nitrogen (approximately -196°C).Choosing the high and low temperature point which best suites your application range improves the R vs. T correlation when applying the formulas. Using α, δ, and β, the Callendar-van Dusen equation can alternately be written as shown in equation 5:

$$R_T = R_0\left\{1 + \alpha\left[T - \delta\left(\frac{T}{100}\right)\left(\frac{T}{100} - 1\right) - \beta\left(\frac{T}{100}\right)^3\left(\frac{T}{100} - 1\right)\right]\right\} \qquad \textbf{(5)}$$

3.4 Metal or Ceramic heater

The heater material has crucial influence on heating system performance. Two types of heaters are commonly used metal and ceramic. Both have their own advantages and disadvantages.

Metal heaters have been widely used in our daily life e.g. kitchen, industry furnaces, in the temperature range RT-2000 °C. Metal is a very good conductor with quick heating response. The fast response is important for achieving effective feedback control loop. In the feedback control, the temperature of the heater is measured and corrected in real time by supervising the resistance of the heater.

It requires both the voltage and the corresponding stable current to be measured accurately and simultaneously. The shorter response time is, the faster the feedback loop can be. Long response time slows down the feedback loop, in the worst cases it may cause the failure of the feedback mechanics as its speed cannot follow the environments change. Metal heater has almost uniform performance throughout the whole temperature. However, it becomes unstable physically and chemically when the heating approaches the metal's melting point. Ceramic is usually used as high temperature materials above 1000°C, as it has different properties from metal. Ceramic is chemically stable at high temperatures. With increasing temperature, the electrical conductivity of the ceramics becomes better. However, at low or moderate temperatures around 500°C, the conductivity of ceramics is poor and more importantly the response time of ceramics is slow, making it is difficult to achieve effective feedback control. The heater system from (DENS solution) uses metals with high melting points as heater materials to harvest the benefits of using metals and at the same time overcome it challenges. EDX analysis of the MEMS heater material found the material to be Molybdenum, figure 3-3 shows the MEMS structural properties and physical properties.

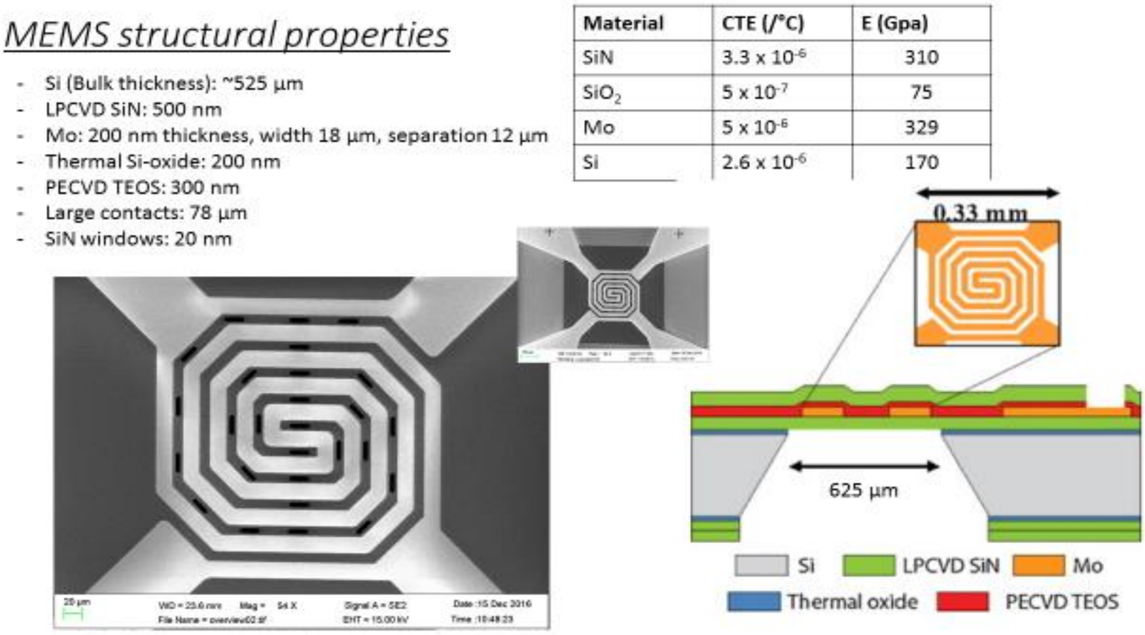

MEMS structural properties

- Si (Bulk thickness): ~525 μm
- LPCVD SiN: 500 nm
- Mo: 200 nm thickness, width 18 μm, separation 12 μm
- Thermal Si-oxide: 200 nm
- PECVD TEOS: 300 nm
- Large contacts: 78 μm
- SiN windows: 20 nm

Material	CTE (/°C)	E (Gpa)
SiN	3.3×10^{-6}	310
SiO_2	5×10^{-7}	75
Mo	5×10^{-6}	329
Si	2.6×10^{-6}	170

Figure 3-3 shows the MEMS structural properties and physical properties

3.5 Difference between Resistance or Power dissipation as temperature indicator

Using ΔR/R relative change of resistance and not absolute resistance as temperature indicator offers a big advantage over using power dissipation because the resistance is independent of the external environment and the type or the amount of sample loaded. For instance, setting a heater at 500 ^{0}C in 10^{-7} mbar vacuum, the power dissipation of the heater is typically 6 mWatts, the measured resistance of the heater is typically 350 Ω; whereas setting a heater at 500 ^{0}C in 10^{-2} mbar air gas environment, the measured power dissipation of the heater can be as high as 19mWatts, but the measured resistance of the heater remains the same. Figure 3-4(a) shows a plot of relative resistance change versus the dissipated power in vacuum and air for a Dens heating MEMs chip.

Furthermore the type and amount of sample loaded onto the heater will also have an influence on the dissipation power for reaching a certain temperature. Simply the greater the amount of material loaded on the MEMS, the more power required to thermally stimulate the material. The dissipation of power highly relies on the transport property of the environment around the sample and the thermal capacity of the samples. Figure 3-4(a) shows a plot of the relative resistance change in proportion to the dissipated power obtained by testing the MEMS chip *in-situ* in vacuum and on the bench in air. It should be noted we observed a requirement for a significant increase in dissipated power in air compared to vacuum to achieve the same relative resistance change, this increase in dissipated power in air significantly reduces the life cycle of the MEMS chip at higher temperatures.

(a)

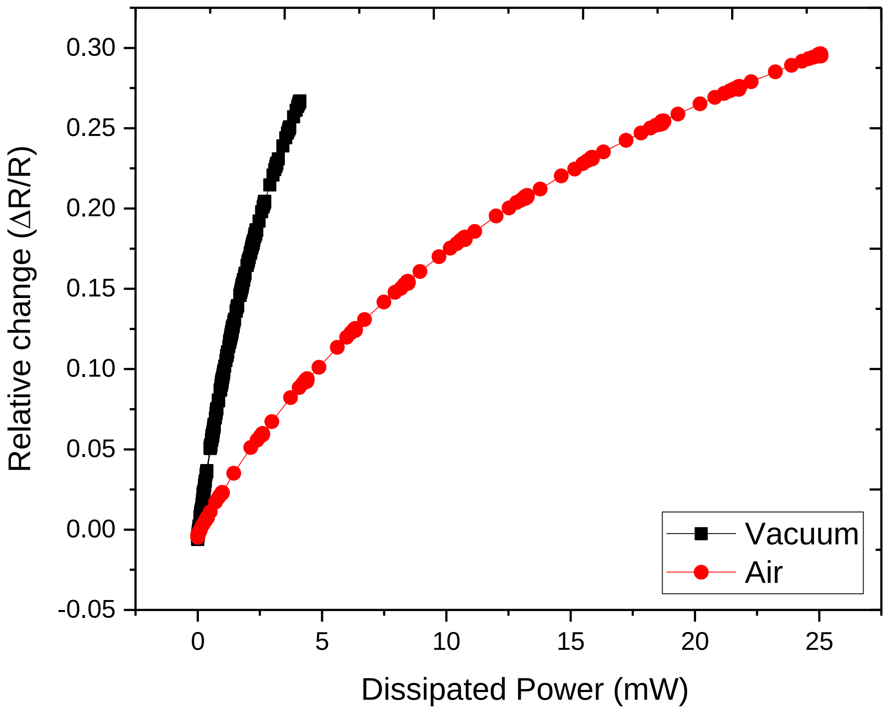

Figure 3-4 (a) Plot of relative resistance change versus dissipated power in Vacuum and Air for DENS heating MEMS Chip.

In contrast, the resistance temperature relationship, well defined by Callendar-Van Dusen as shown equation 1 (page 27) is independent to the external factors other than temperature.

This is why the DENS solution MEMS uses resistance as a temperature indicator, allowing the calibration parameter obtained in the calibration environment to be applied to the heater chip in various working environments.

3.6 2 Contacts or 4 contacts measurement

For measuring the resistance, 2 contact or 4 contact resistance measurement can be chosen. In the two contact resistance measurement figure 3-5(a), the total resistance of the system is actually measured, including the resistance of the micro-heater, the resistance of the cables that connect the heater to the outside regulator, the resistance of contacts from mechanical connections of various cables and needles to the chip interface resistances. As the cables and the contacts may be in a temperature environment different from the micro-heater (note that some part of cables are even outside microscope) and the material of the cable and the heater may be different, the total resistance method cannot be directly used to link the temperature of the micro-heater. For these reason the DENS solutions heating holder uses four contact resistance measurement method as show in figure 3-5(b) for obtaining the resistance of the heater. This method excludes the influence of the cable resistance and the uncertain contact resistance, allowing the measurement resistance to be used to indicate the temperature of the microheater.

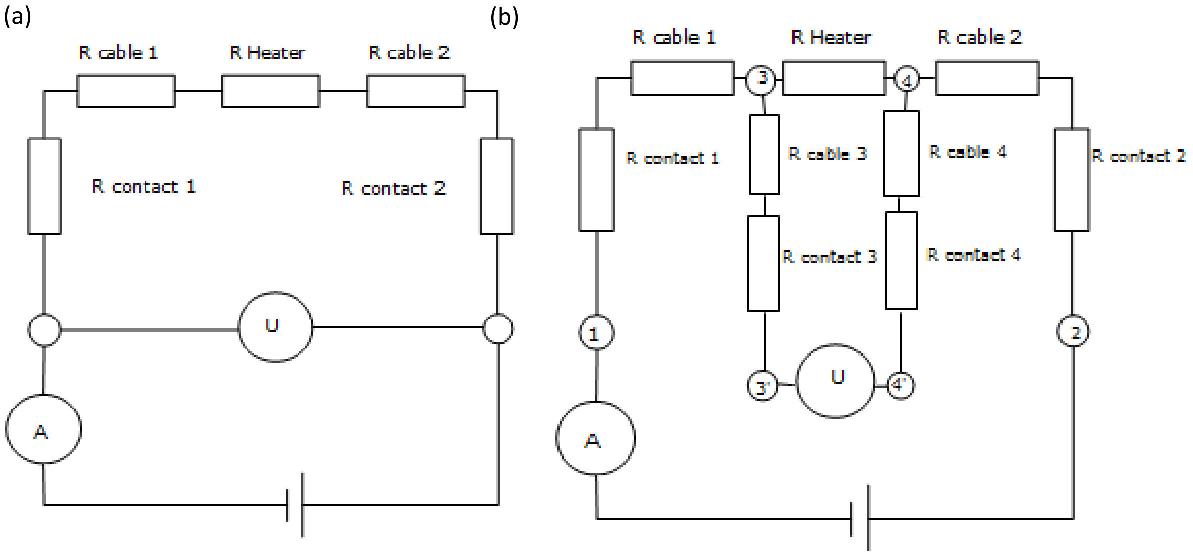

Figure 3-5 (a).Two point contact resistance schematic which does not take account of total resistance of complete electrical setup during analysis (b) Four point contact resistance schematic for heating holder which takes account of the total resistance of complete electrical setup during analysis.

3.7 Temperature gradient across the MEMS device

Heating is localized around the centre of the micro-hotplate. The temperature 300µm away from the edge of the micro-plate drops to room temperature as shown in figure 3-6. The micro scale heating results in a power consumption of only several mWatts for reaching high elevated temperature above 1000°C. This low power consumption and localized heating dramatically reduces the sample drift during heating experiments and avoids the using water to cool down the holder. Figure 3-7(a) shows the temperature localized around the micro hotplate of the MEMS chip, figure 3-7(b) shows the mems chip in air under an optical microscope at 950°C showing the localized heating.

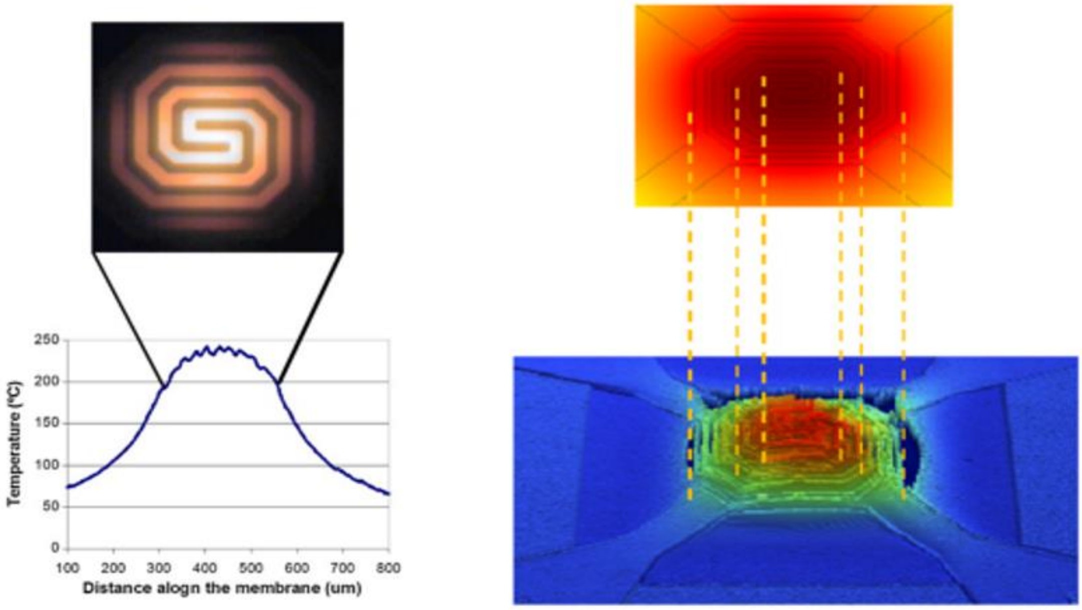

Figure 3-6 shows the temperature gradient profile across the MEMS device [60]

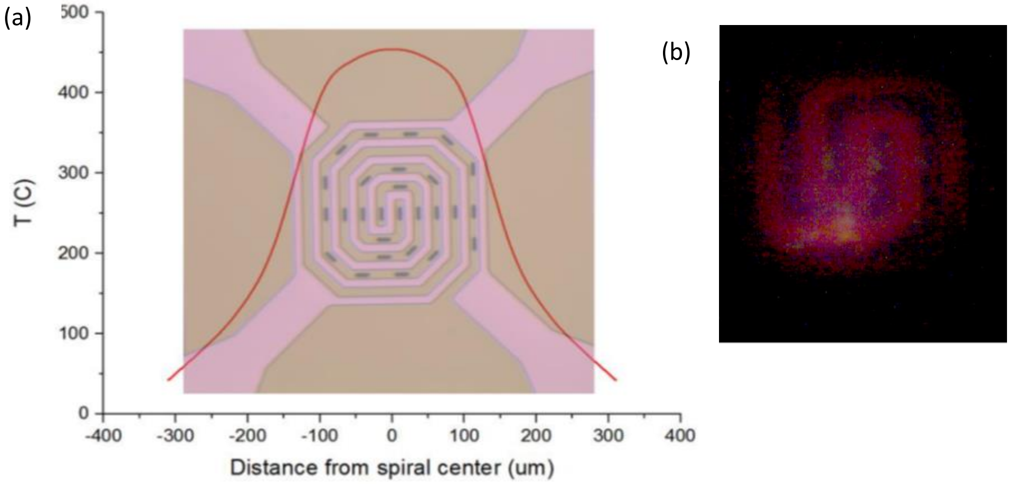

Figure 3-7 (a) showing temperature localized around micro- hotplate ,cross calibrated with resistive thermal sensor, infrared pyrometry, and Raman thermometry (b) image of mems chip at 950°C under optical microscope.

It is mainly the EM heater chip that determines the temperature working range and thermal drift rates, figure 3-8(a) shows data provide by DENS solutions of the amount of thermal drift over a 25 hour period. Thus, it provides the possibility to upgrade the heating system performance, by simply introducing a new MEMS. Standard MEMS chips can work up to and above 1000°C. The ultra-high temperature heating chips can work up to above 1400°C.

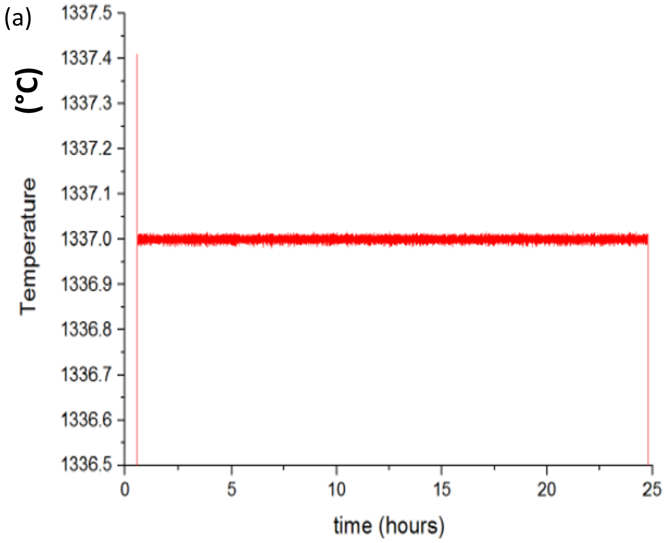

Advantages of MEMS based heating holder.

- The thermal stress is localised around a small inner coil.
- Local heating removes excessive thermally induced drift.
- 4-point geometry allows for very accurate and controlled temperature measurement.
- Rapid temperature elevation and relaxation.
- MEMS chip customisation

Figure 3-8 (a) Plot of temperature drift over a period of 25 hours, the temperature was set at 1337.0 °C on ultra-high temperature chip.

3.8 MEMS flexural distortion during heating in-situ in TEM

It was noted during experiments that there was a requirement to repeatedly de-focus the image each time we increased temperature. This was found to be due to the MEMs chip flexing during heating. To characterize the flexing of the MEMS chip due to heating 8 locations on the MEMS chip were selected to measure the defocus value versus the temperature at evenly distributed locations from the centre of spiral heater of the MEMS chip to the outer spiral of the MEMS chip. Figure 3-9(a) shows a plot of the resulting defocus values versus temperature at the 8 locations indicated in figure 3-9(b).

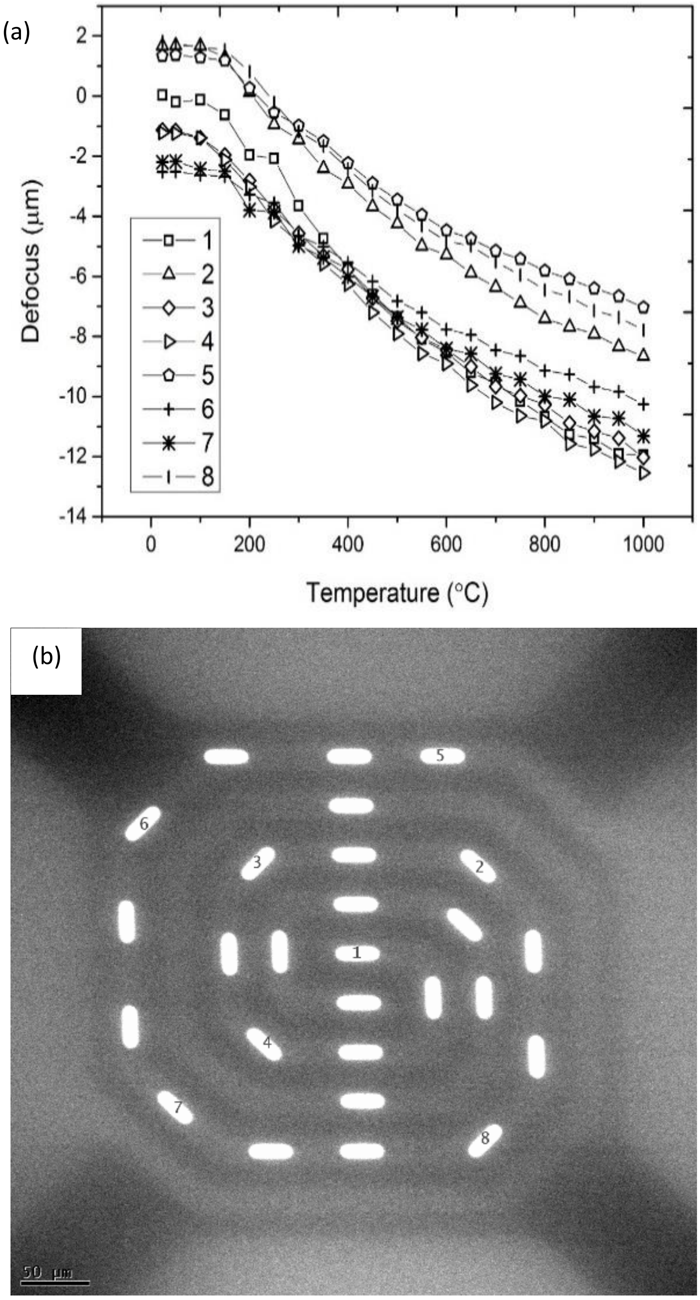

Figure 3-9 (a) Plot of defocus value at various locations on MEMS chip versus temperature (b) TEM overview of the MEM chip and the map of measurement locations.

The measured defocus values for all 8 locations were plotted against temperature to produce a visual map of the MEMS chip flexural distortion under thermal stress. The plots shown in figure 3-10 gives an indication of the flexural distortion at a range of temperatures.

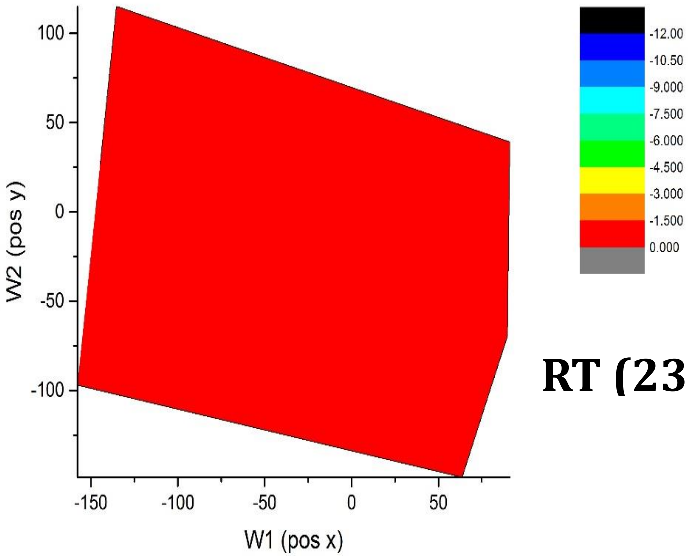

RT (23°C)

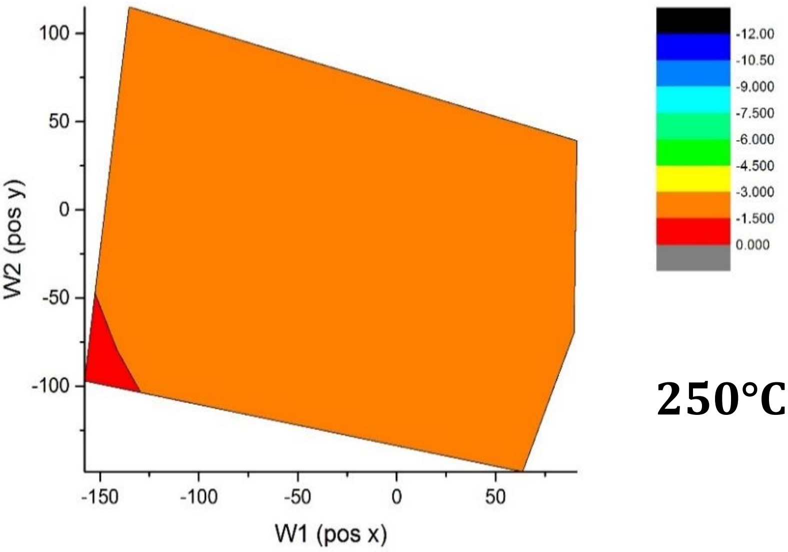

250°C

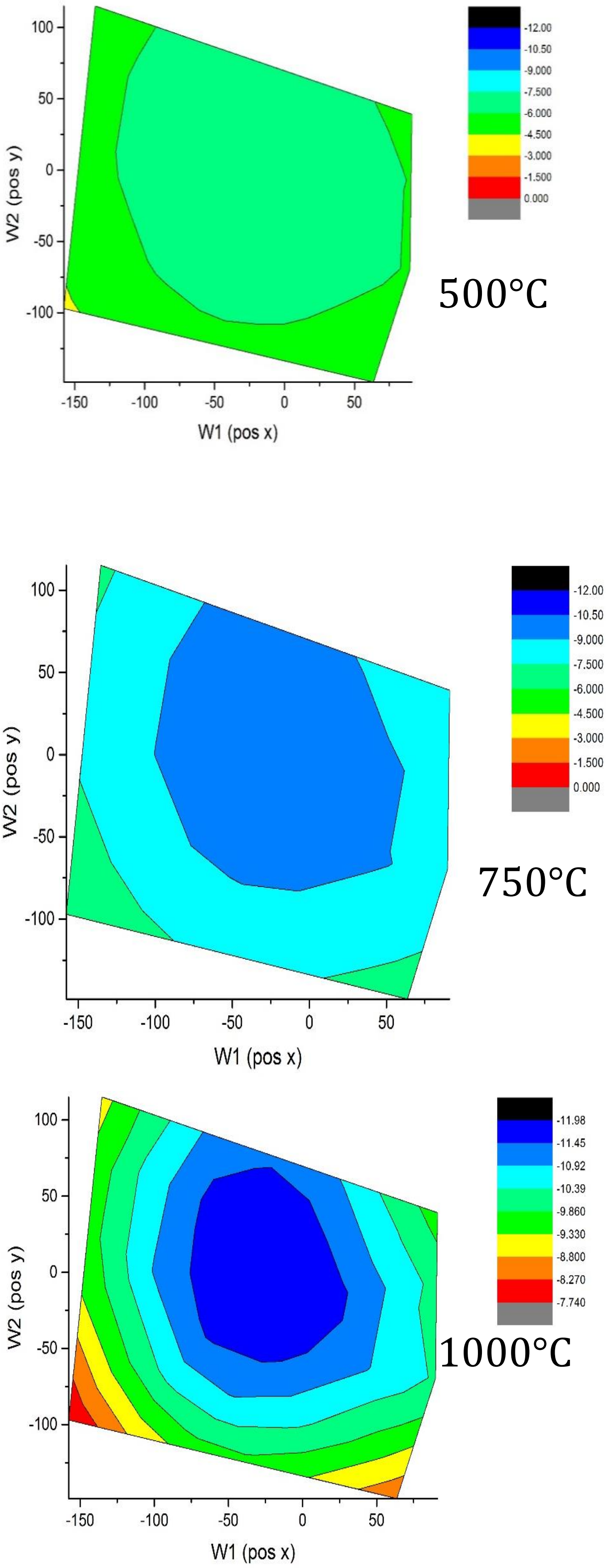

Figure 3-10 Plots of flexural distortion due to thermal stress across the area of the heater spiral of the MEMS chip.

The process was repeated for 26 locations on an through hole MEMS chip. Figure 3-11 gives an indication of the observed distortion at a range of temperatures on the through hole MEMS chip.

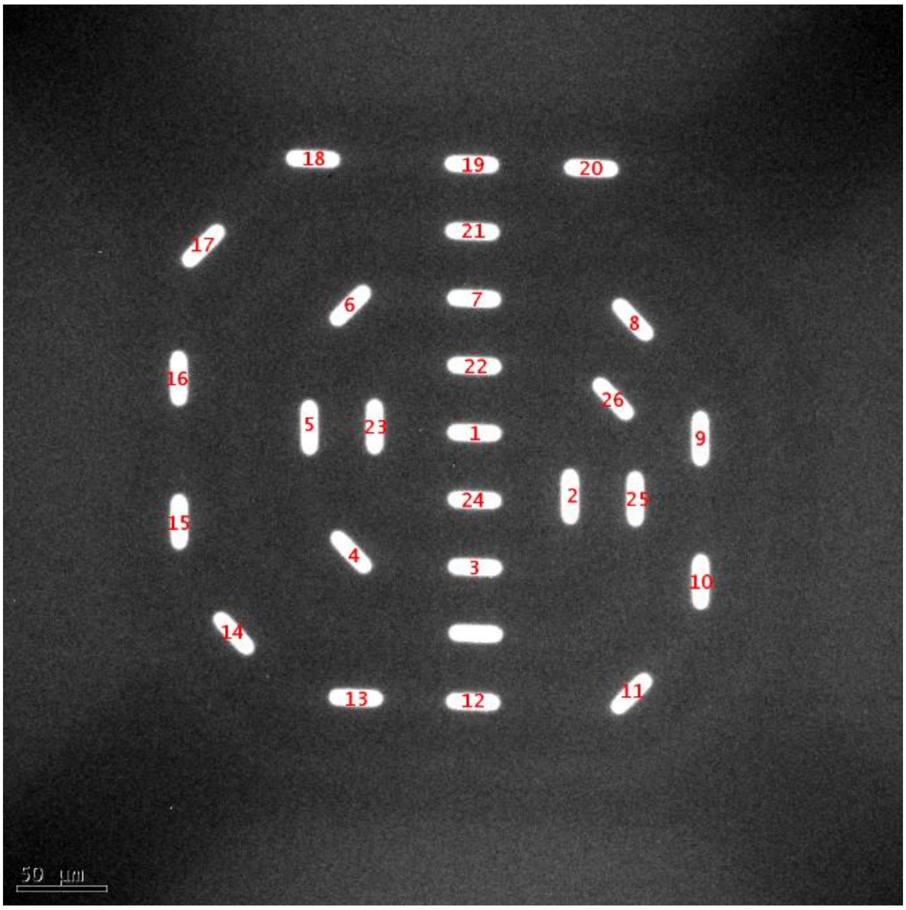

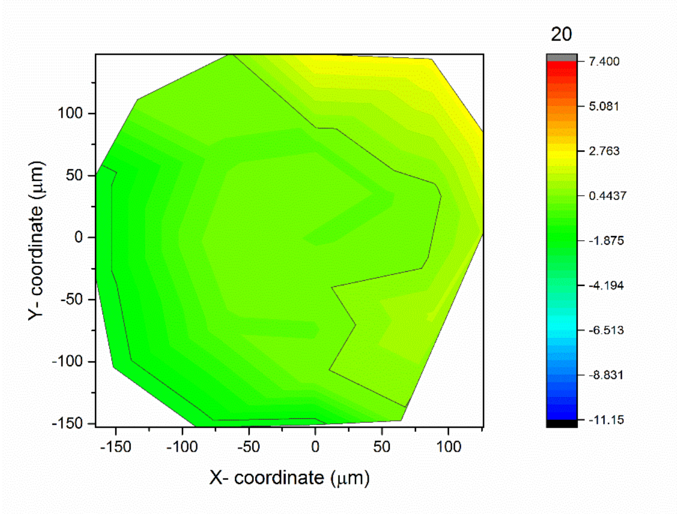

MEMS flexural distortion at 20°C

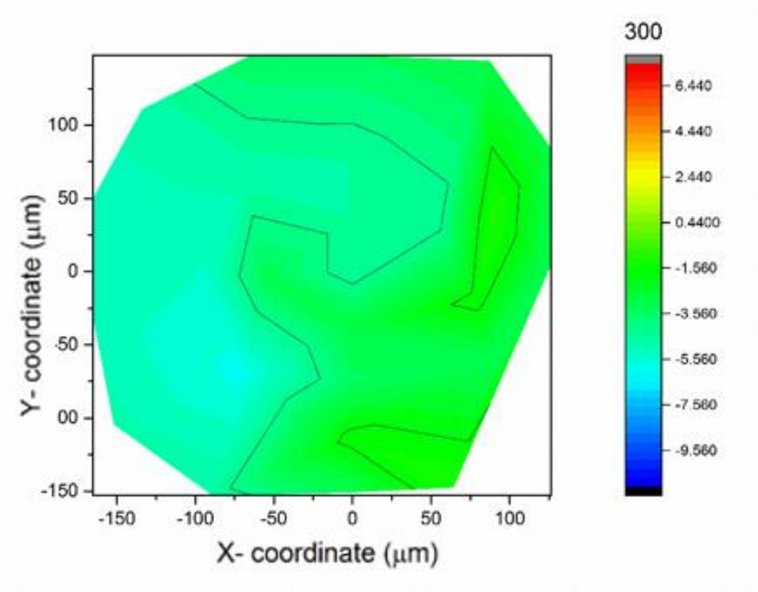

MEMS flexural distortion at 300°C

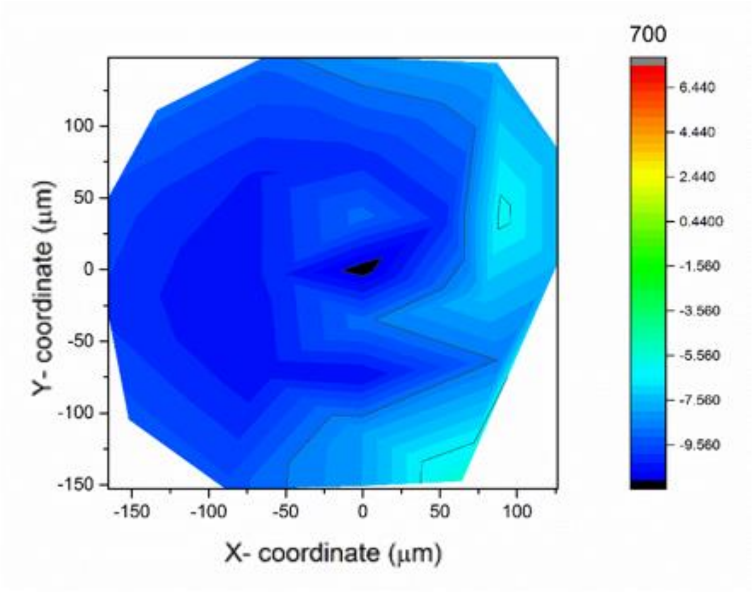

MEMS flexural distortion at 700°C

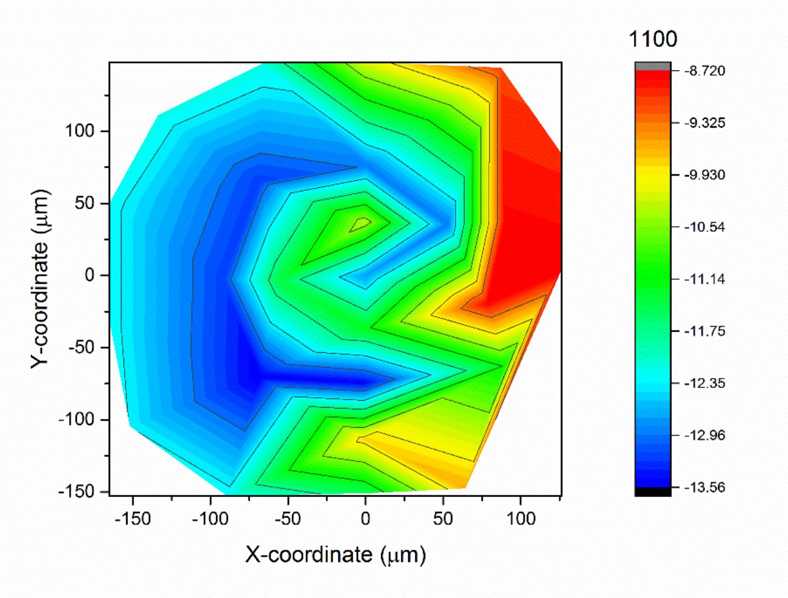

MEMS flexural distortion at 1100°C

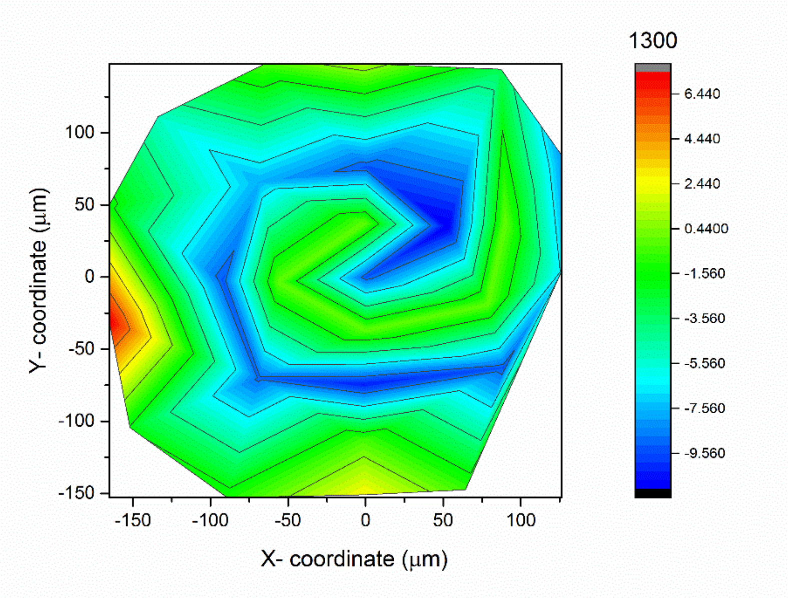

MEMS flexural distortion at 1300°C

Figure 3-11 Plot of flexural distortion due to thermal stress across the area of the heater spiral of the through hole MEMS chip.

3.9 *In-situ* SEM heating MEMS

MEMS setup in SEM to observe MEMS flexural distortion during heating

An experimental setup was developed to enable in-situ heating in SEM and also to investigate further the actual flexural distortion of the MEMS during heating. The DENS solution MEMS heating chip was attached to a SEM stub using a carbon tab. Two Kliendiek nano manipulators (MM3A) with probe tip ~100nm were mounted inside the SEM chamber and controlled through a SEM chamber feedthrough flange and standard feed through electrical connections to each manipulator and corresponding controller units. A Keithley dual source meter (2600 series) was connected in series to the controller units and use to ramp the current (I) and voltage (V) to the contact pads on the MEMS via the manipulator probe tips. The figure 3-12(a) shows the probe tips in contact with the MEMS contact pads. The voltage and current was ramped in a controlled manner however this experimental setup uses 2 point probing directly onto the MEMS chip which is not as controlled or as accurate as four point probing method used in the DENS solutions heating holder setup in TEM.

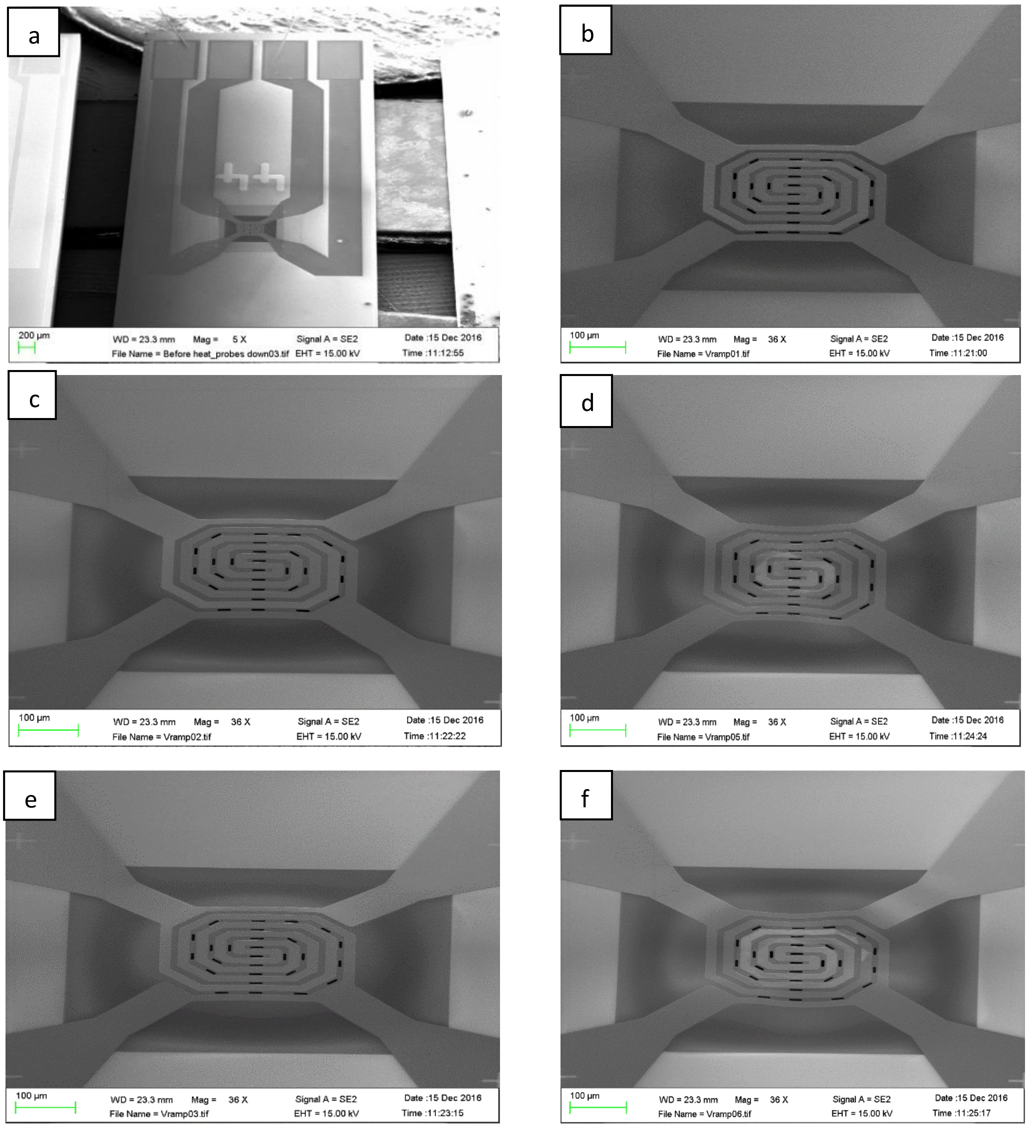

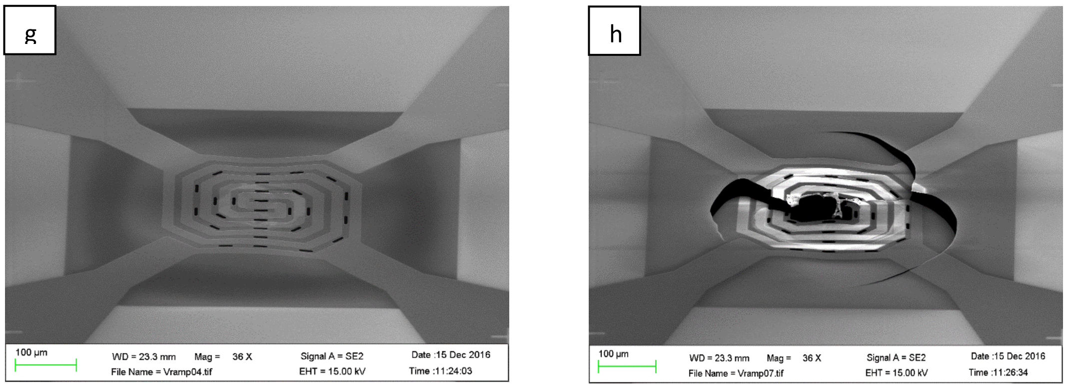

Figure 3-12 (a) shows the manipulator probe tips in contact with contact pads of MEMS chip (b-h) shows SEM images of the flexural distortion as heating increases in the range of 20°C to around 750°C.

Significant flexural distortion was observed as a function of temperature as the temperature was ramped from 20°C to failure temperature ~750°C figure 3-12(b-h). The flexural distortion observed in SEM followed the measured flexural distortion in TEM as shown in figures 3-10, 3-11. The higher the chip power consumption and power density are, the more pronounced effects and surface effects are .The mismatch of heat stress is more severe ,which can cause the MEMS devices to distortion. It should also be noted in the SEM experimental setup the MEMs chip failed at a temperature lower than its specification, this was most likely due to the experimental setup in SEM and the degree of control while ramping the voltage and current.

3.10 Electrical probing on circuit edited MEMS chip in SEM &TEM

A method was developed to electrically contact samples placed on the heating MEMs chip by modifying the MEMS heating spiral. FIB was used for this purpose. The procedure was demonstrated on a Black Phosphorous (BP) flake that was mechanical exfoliated and placed over a window on the heating MEMS chip as shown in figure 3-13. Black phosphorus is the thermodynamically stable form of phosphorous at room temperature and pressure.

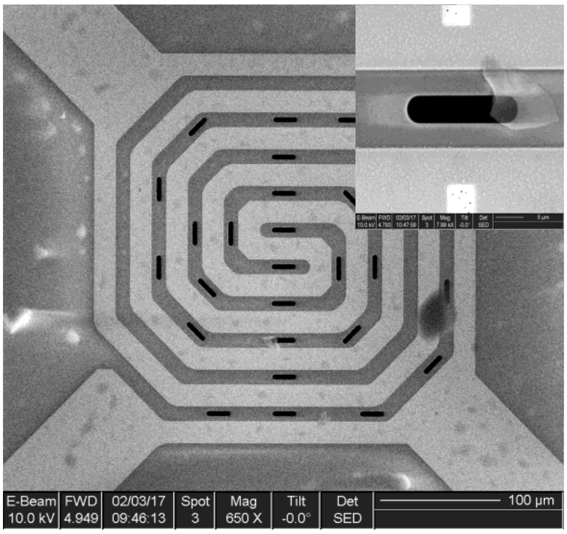

Figure 3-13 Black phosphorus flake mechanical exfoliated onto MEMS chip.

Once the position of sample on the MEMS chip was determined the MEMS electrical heating spiral was modified by a series of FIB cuts to isolated two sections of the spiral circuit as shown in figure 3-14. These isolated sections of the spiral maintained direct connection to the their respective contact pads on MEMS chip thus enable electrical connectivity to the DENS Solution heating holder when performing electrical measurements in TEM and to also allowing the micro manipulator probes to make electrical measurements when set up in SEM see figure 3-12(a).

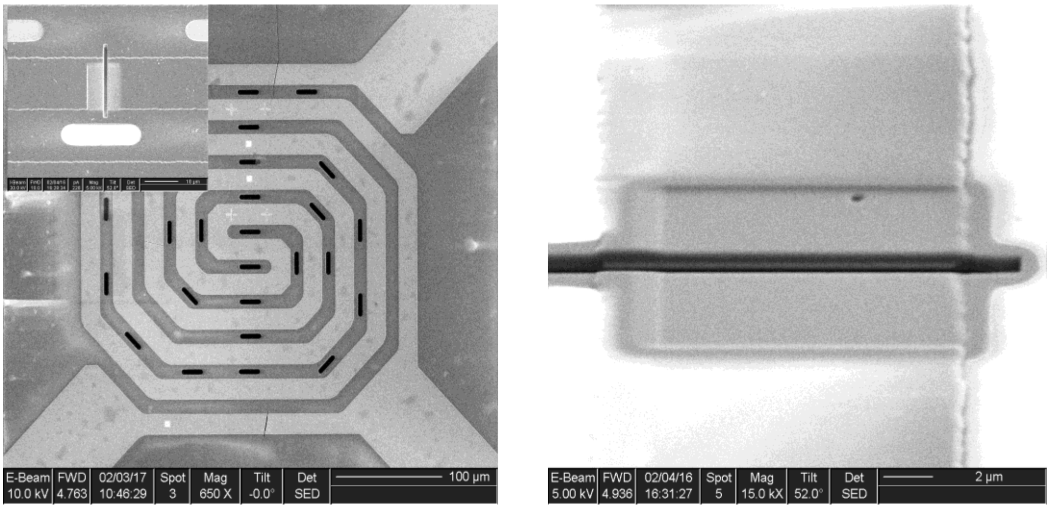

Figure 3-14 FIB cuts to isolate sections of the heating spiral to enable electrical measurements.

A 3µm x 3um window in the silicon nitride top layer of the MEMS chip was milled away using FIB to create an electrical contact to the molybdenum metal spiral below in the two isolated spiral section adjacent to the window where the sample was placed (see figure 3-15).

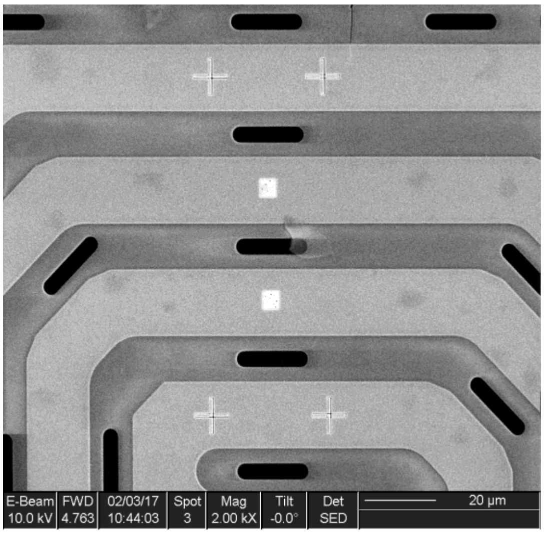

Figure 3-15 Windows exposed in silicon nitride layer to allow electrical contact

The gas injection system and FIB/SEM was used to make electrical connection between the sample and the exposed metal of the spiral in the window using e-beam platinum deposition figure 3-16(a). A resistance measurement between -10V and +10V was obtained for the BP sample flake tested in SEM using the micro manipulators and an Keithley source meter the corresponding IV curve was obtained and is shown below in figure 3-16(b).

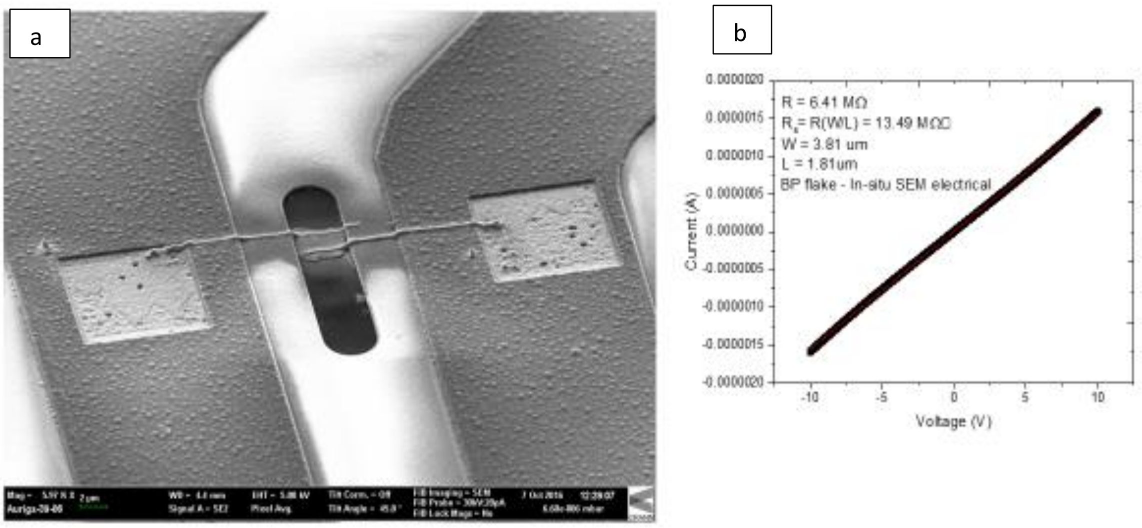

Figure 3-16 (a) SEM image of e-beam deposited electrical connection (b) IV curve

A second BP sample was prepared using the same procedure, however this MEMS chip was placed in the Dens Solutions heating holder and the electrical measurement were made in-situ in TEM using the heating holder and electrical feedthrough connector box connected in series to the Keithley dual source meter. Figure 3-17(a) shows TEM overview of a platinum e-beam deposited contacts to BP flake. The corresponding IV curve was obtained for the BP flake under test in the voltage range -15V to +15V and is shown below figure 3-17(b).

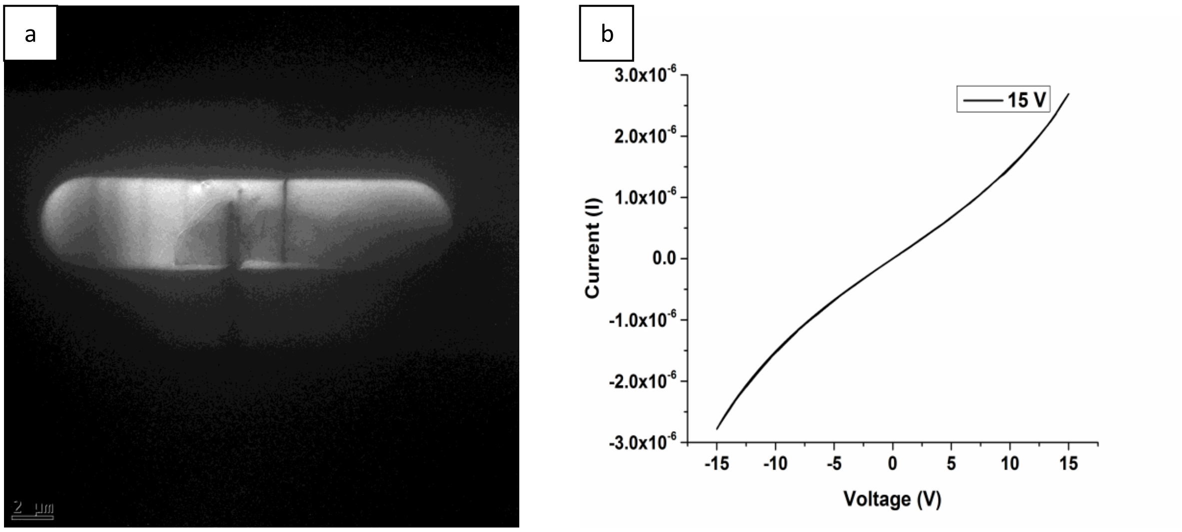

Figure 3-17 TEM image showing sample and platinum e-beam deposition to make electrical connection (b) IV curve

After electrical testing was completed the MEMS chip was heated up to 190°C on a hotplate to see the robustness of the platinum deposition making the electrical contact between the sample and the MEMS spiral. TEM images were taken before and after heating. It was noted that the heating causes ‘’opens’’ and the potential for ‘’shorts’’ in the connections. The TEM images below figure 3-18(a) show the electrical connections before heating figure 3-18(b) after heating to 190°C on a hotplate.

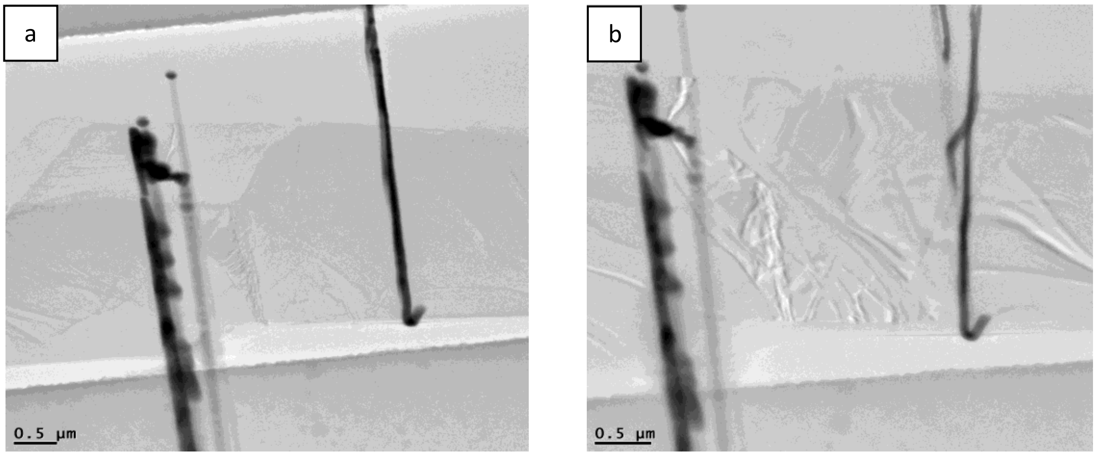

Figure 3-18 (a) TEM image of e-beam electrical connections prior to heating (b) TEM image of e-beam electrical connections after heating showing ''opens'' .

Further work is required in this area. My long term plan would be to make electrical contacts on the MEMS chip using e-beam lithography, allowing heating and electrical testing experiments to take place simultaneously on the same sample. Our initial results show that electrical contacts obtained using platinum e-beam deposition can only be used for electrical measurements. However such measurement would be limited by the high resistivity of the platinum interconnects. With additional experimental setup it may be possible to explore the possibility of annealing samples in the He-ion / FIB microscope while milling. This would help establishing whether heating regimes can help reducing the conventional gallium / helium diffusion/implantation occurring while milling. Heating while milling may reduce the inherent damage caused when ions impact the sample; it may also reduce the level of carbon contamination on the sample.

4 An *in-situ* heating TEM Study into the thermal decomposition of Black Phosphorous nano-sheets

4.1 Introduction

Ever since its discovery [61][25], graphene has been one of the most researched materials for its electronic and energy applications [62][63]. It has a very high carrier mobility (of the order of nearly 2.5×10^5 cm^2 V^{-1} s^{-1}), but due to its semi-metallic nature, it is impossible to completely turn the current off which hinders its application in microelectronic devices, such as field-effect transistors (FET) and computer chips. The successful isolation of graphene has motivated research in other inorganic layered 2D materials like h-BN [64] , transition metal oxides[65], graphitic oxides[66], transition metal dichalcogenides (TMDs) [17], black phosphorus (BP) [67] and post-transition metal oxides [68]. Some of these materials show properties that are rivalling or exceeding that of graphene. For example, monolayer MoS_2 has a band gap of 1.8 eV and a carrier mobility of 200 cm^2 V^{-1} s^{-1}. But the direct nature of the band gap is not lost in any number of layers. More recently, over one hundred years after it was successfully synthesis in the bulk form in 1914[69], monolayer black phosphorus (BP) namely phosphorene, has been attracting a lot of attention as a 2D layered material, which in turn has attracted interest from condensed matter physicists, chemists, semiconductor device engineers and material scientists. Similar to graphite and TMDs, BP has a layered structure but with a unique puckered single layer geometry as shown in figure 4-1.

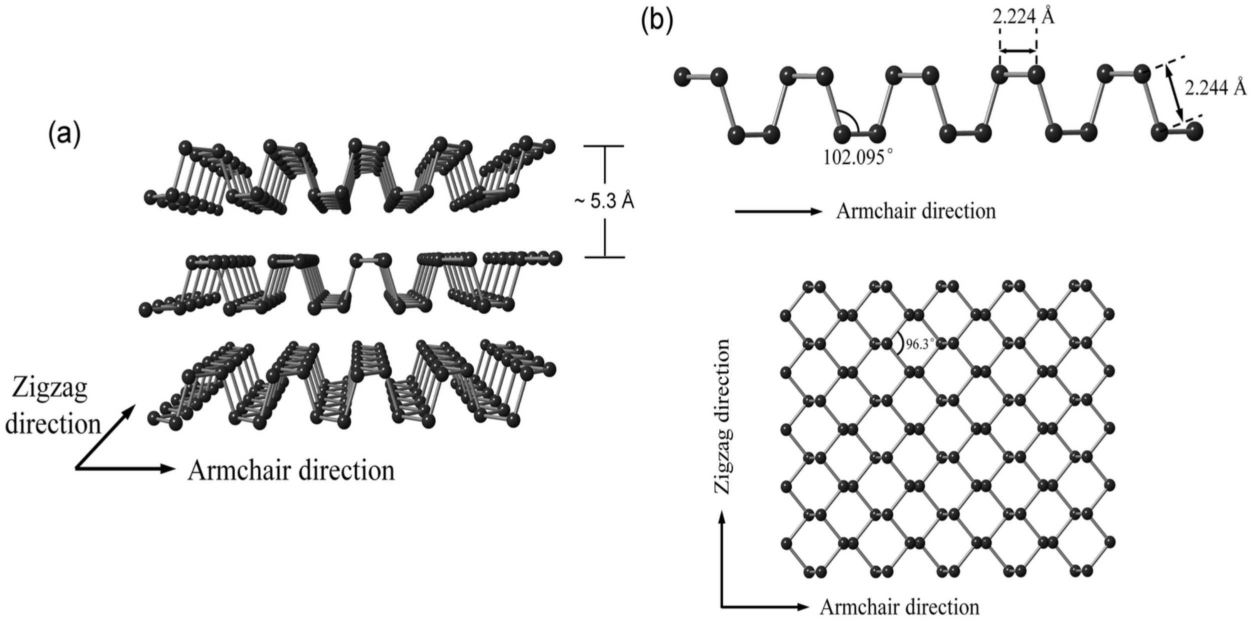

Figure 4-1 (a) Atomic structure of multi-layer black phosphorus and (b) monolayer phosphorene [70].

Due to its intriguing properties such as moderate direct band gap (0.3eV - 2 eV), which depends on it thin film thickness, very high carrier mobility of 10^3 cm^2 V^{-1} s^{-1} and anisotropic in-plane properties, BP looks a promising candidate for applications in nano-electronics and nano-photonics that differ from graphene and TMDs. Phosphorene's main drawback is that it degrades in ambient atmosphere and in contact with water[71]. However, it has been reported that special treatments involving the formation of chemical or physical passivation layers can be used to overcome stability issues in exfoliated BP [72]. D. Hanlon et al., for example, demonstrated that exfoliating black phosphorous in liquid-phase in the organic solvent CHP (N-cyclohexyl-2-pyrrolidone) can increase the lifetime of the system from hours to months. The reason for such an increase in its lifetime was mainly attributed to the formation of a CHP solvation shell around the BP sheets.

The use of protective chemical or physical passivation layers is however inconvenient for all those applications which require the use of pristine flakes. In order to get insights on the mechanism involved in the BP degradation I carried out a systematic *in-situ* thermal TEM analysis.

4.2 Experimental Methods

In order to rule out any contribution from solvents in most cases we carried out our experiments on mechanically cleaved BP nano-sheets, transferred onto a MEMS chip. *In-situ* TEM was carried out in a FEI Titan300 operated at 300kV and 80kV. Furthermore, I investigated the e-beam contribution to the nano-sheets degradation. In order to do so, I worked in two different regimes: "beam-off", meaning that the sample was heated while blanking the beam, and turning it on only for imaging post-heating; and "beam-on", meaning that imaging was carried our while the sample was heated.

4.3 Experimental Discussions: *in-situ* thermal decomposition of Black Phosphorus

The first task was to establish the thermal stability of the flake during heating. For this purpose the flake was initially heated up to 300°C over a period of 10mins in a beam-off condition (to avoid any e-beam contribution). Figure 4-2a and b show typical TEM images of a BP flake that was heated to 350 °C and 400°C respectively in the beam-off condition (i.e. sample not exposed to the electron beam while heated). Both images show little degradation occurring after heating to 350 °C and 400°C, respectively.

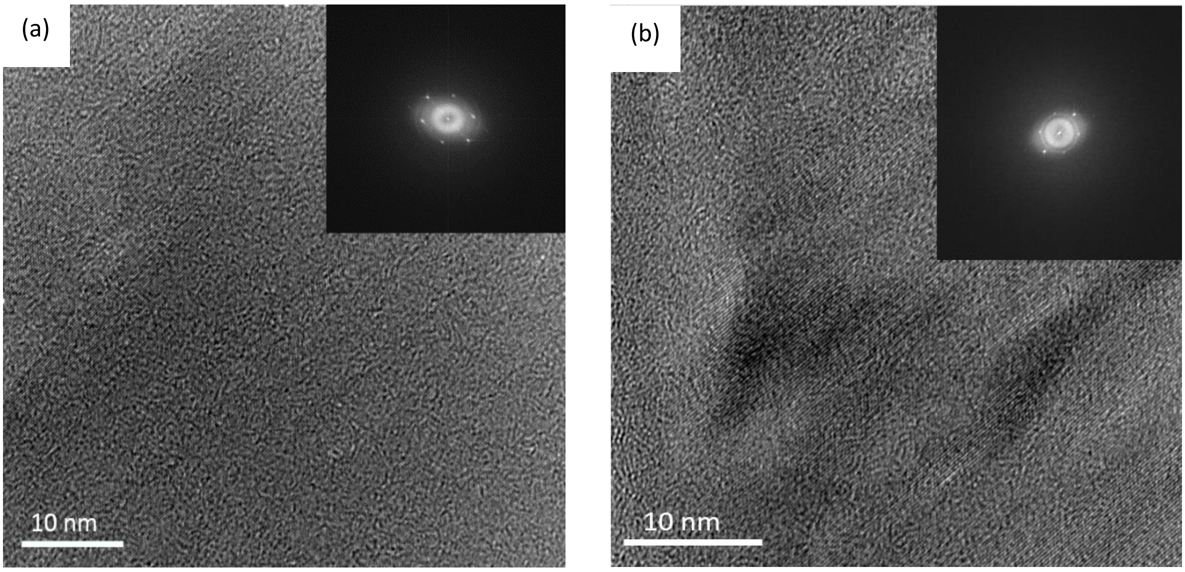

Figure 4-2 (a) Typical TEM image of a BP flake after heating to 350°C (heating occurring over the course of 10 mins) in an e-beam-off set-up (no imaging while heating). The inset shows the FFT of the same area; (b) Typical TEM image of a BP flake after heating to 400°C (heating occurring over the course of 10 mins) in an e-beam-off set-up (no imaging while heating). The inset shows the FFT of the same area. Both images show sign of very little degradation happening with heating, whilst the FFTs remark a very high degree of crystallinity being present.

In order to monitor the possible contribution of the electron beam, we carried out a second set of *in-situ* experiments, heating a BP sample this time while imaging (beam-on configuration). Figure 4-3a shows a typical TEM image of a BP flake that was heated to 450°C, while being exposed to the imaging electron beam for 2 minutes. This image (electron dose =4.8 x 10^5C/cm² at a magnification of 380Kx; beam current= 8.94nA) and its corresponding FFT in the inset) demonstrate that the flake has completely lost all its crystallinity.

In contrast, figure 4-3b shows a flake that was heated to the same temperature as shown in 4-3a but without any exposure to the electron beam (beam-off configuration). As can indeed be seen in the FFT in the inset, the flake has remained perfectly crystalline and displays the expected diffraction spots.

Finally, figure 4-3c shows the same BP flake as in figure 4-3b after it had been continuatively heated at 425°C and exposed to the electron beam for 1 minute (electron dose= 2.4 x 10^5C/cm² at a magnification of 380Kx; beam current=8.94nA for the area shown in figure 4-3c).

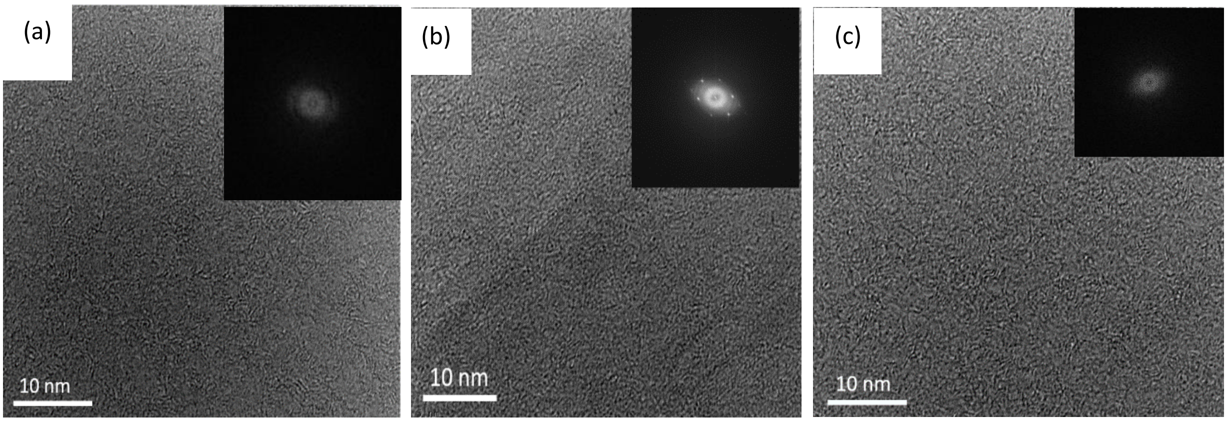

Figure 4-3 (a) Typical TEM image of a BP flake after heating to *425ºC while being exposed to the electron beam. The FFT in the inset show the sample becoming completely amorphous; (b)* Typical TEM image of a BP flake after heating to 425ºC *for the same duration as flake in (a) but with no beam irradiation (beam-off configuration); the FFT in the inset shows the flake being still perfectly crystalline; (C) typical TEM image of the same BP flake in (b) heated to 425º when exposed to the beam while heating for an additional 2 mins at* 425ºC*. The FFT in the inset shows the flake going completely amorphous.*

These simple initial results showed that the electron beam was indeed causing severe degradation of the BP flakes. To investigate this effect further a similar set of experiments was repeated at a TEM beam acceleration voltage of 80KV.

Figure 4-4(a) shows a typical TEM images of a BP flake acquired with an acceleration voltage of 80kV and in normal conditions (no heating). The FFT displayed as an inset shows the expected good crystallinity of the pristine as-exfoliated material.

Afterwards we started heating the sample at 2 minute interval steps up to 300ºC. An image of the system after such heating is displayed, together with the corresponding FFT, in figure 4-4(b). The system after this heating ramp still clearly displays a very good degree of crystallinity.

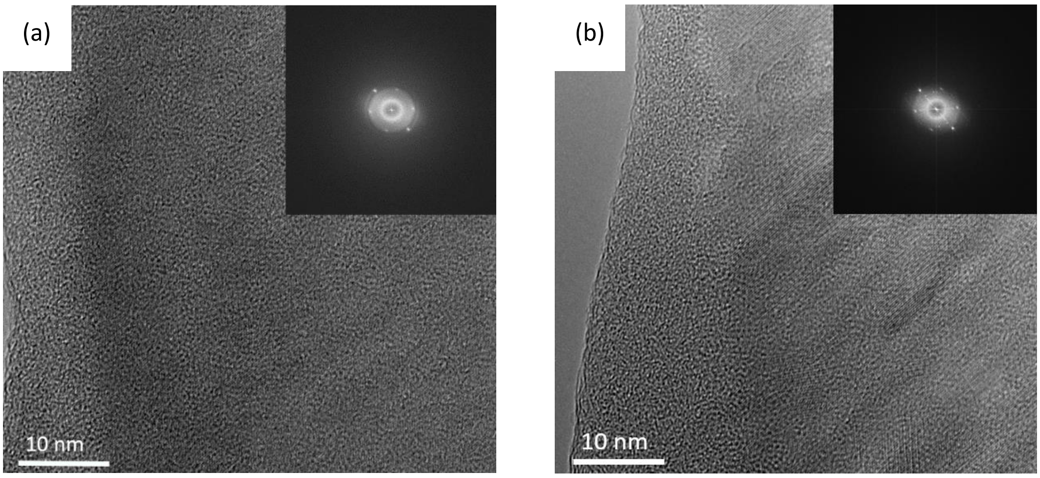

Figure 4-4 (a) Typical TEM image of a BP flake acquired with an acceleration voltage of 80kV and at normal conditions (no heating); the corresponding FFT is shown as an inset confirms the crystallinity of the as-exfoliated nano-sheet; (b) Typical TEM image of a BP flake acquired with an acceleration voltage of 80kV after the sample was heated at 300ºC, the FFT in the inset shows crystallinity.

In order to investigate the simultaneous contribution of beam and heating, the same system afterwards heated to 350°C with simultaneous exposure to the 80KV electron beam (electron dose=30.8 x 10^5C/cm² at a magnification of 380Kx; beam current 11.4nA). Figure 4-5 shows an image series acquired over the course of 10 minutes, demonstrating a clear, progressive degradation of the flake happening within the course of the experiment.

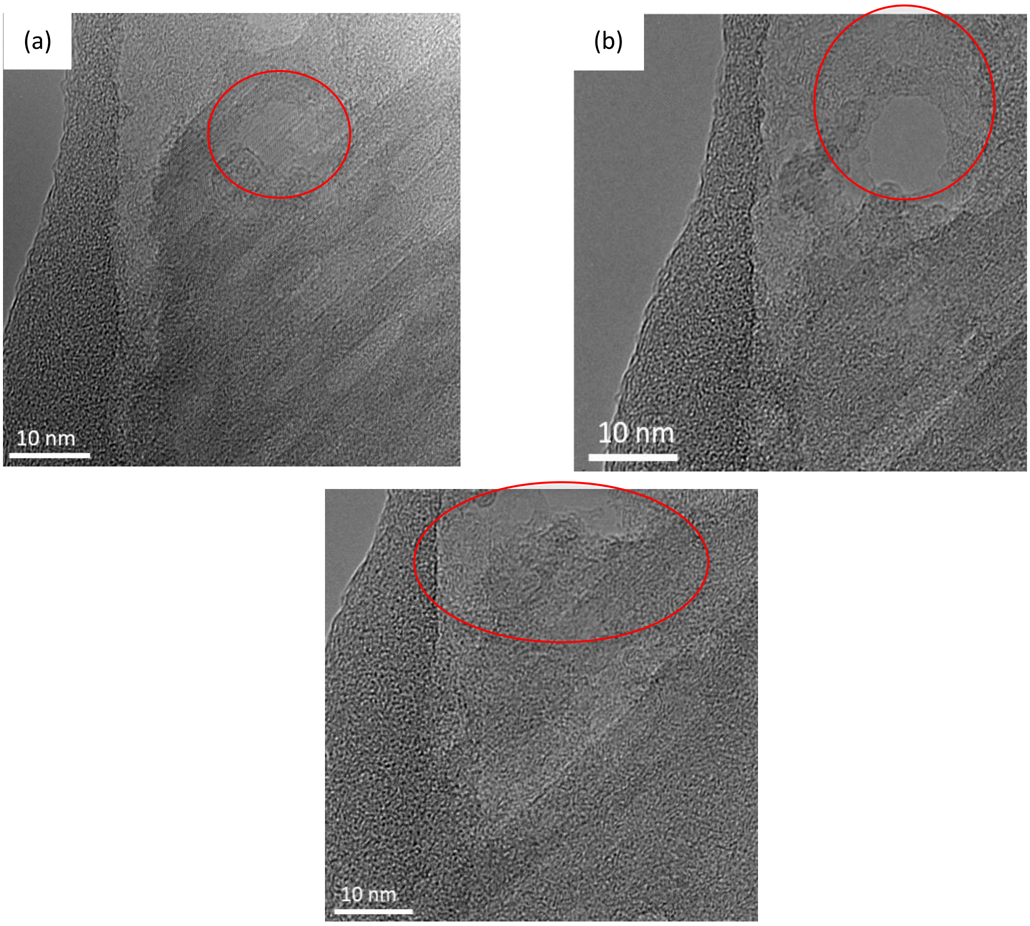

Figure 4-5 (a) (b) (c) TEM image series acquired at 80kV over the course of 10 minutes, showing a BP flake heated at 350^{0}C, while being exposed to the electron beam (electron dose=30.8 x 10^5C/cm² at a magnification of 380Kx; beam current=11.4nA for the area shown in figure c).Damage seems to be induced by heating and beam irradiation. *Areas of degradation are highlighted by red circle on each image in the series.*

As TEM imaging alone is a subjective measure of de-gradation, select area electron diffraction (SAED) patterns figure 4-6 and electron energy loss spectra (EELs) figure 4-7 analysis was undertaken to further confirm the degradation of the material when heated and exposed to the electron beam.

To minimise the effect of the electron beam degrading the BP flake, a series of SAED patterns were acquired at 100°C, 400°C and 500°C at a heating ramp rate of 10°C every 2 minutes in the *beam–off* configuration during heating (patterns shown in figure 4-6 (a), (b), (c) respectively). These demonstrate that BP remains crystalline when heated up to temperatures up to 400°C; it however turns amorphous at 500°C. In order to gather information on the chemical nature of the material undergoing heating we acquired core-loss EELS spectra of the sample after reaching 100°C, 400°C and 500°C at a heating ramp rate of 10 °C every 2 minutes with a 10 minute heating delay interval at 100°C, 400°C and 500°C respectively to acquire the EELS spectra.

These EELS spectra are shown in figure 4-7. Whilst the spectra of the sample heated at 100°C, 400°C show the fingerprint of BP in pristine, non-degraded state, the sample heated at 500°C shows a key change in its $L_{2,3}$ ELNES indicating a difference in the phosphorous bonding structure (Red Phosphorus) most likely due to the degradation of the material due to heating and exposure to the electron beam.

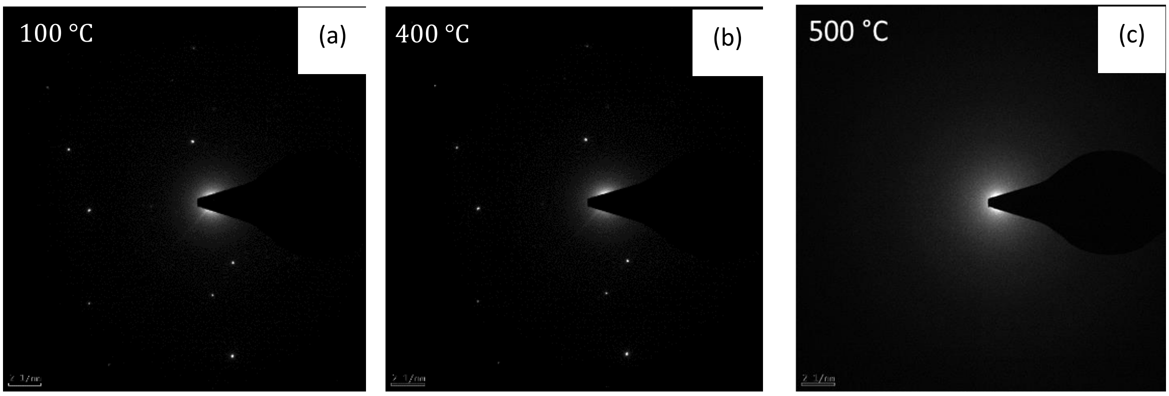

Figure 4-6 (a) 80kV SAED image of BP flake heated to 100°C, (b) 80kV SAD image of BP flake heated to 400°C (C) 80kV SAD image of BP flake heated to 500°C totally amorphous (Red Phosphorus).

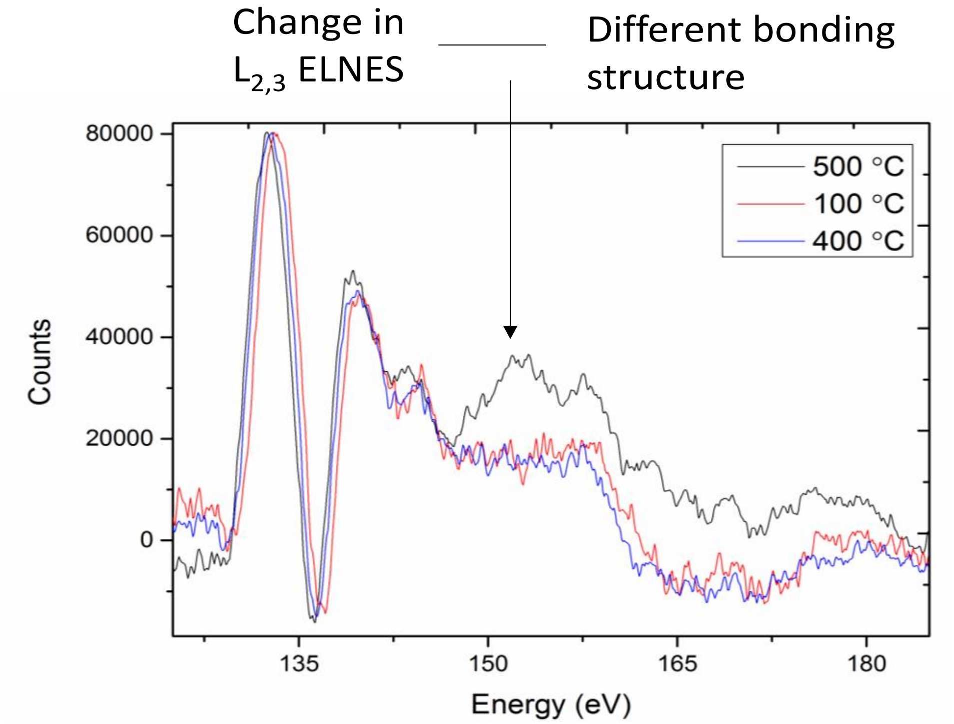

Figure 4-7 EELS spectra showing a change in $L_{2,3}$ ELNES at 500°C indicating a difference in bonding structure (Red Phosphorus).

A series of additional experiments were carried out using different conditions such as temperature, time and exposure to the beam these are shown in appendix 1 (S1), (S2), (S3).

4.4 Conclusions

In-situ heating experiments were carried out on mechanically exfoliated BP. Mechanical exfoliation was chosen over liquid-phase exfoliated material to avoid further effects due to the presence of solvent. The thermally-induced degradation of BP nano-sheets was monitored taking into account possible contributions coming from the electron beam.

To do so, we carried out all heating experiments in two different configurations: *beam-on* (when imaging happened while heating simultaneously) and *beam-off*, when the beam was blanked while heating the sample on the MEMS chip). These experiments show that in beam-on configuration as well as beam-off configurations as shown in figure 4.6, black phosphorus nano-sheets already degrade at temperatures in the range of 400°C-415°C. It should be also noted that findings show that the nano-sheets are very hydrophilic and that long term exposure to air moisture etches black phosphorus away[73].

However, the degradation of the material in TEM can be slowed down by limiting the BP flakes exposure to the electron beam and by imaging with 80KV. A series of additional experiments were carried out using different conditions such as temperature, time and exposure to the beam these are shown in appendix 1 (figure (S1) (S2) in supplementary information).

These additional experiments as well as the results above indicated that the electron beam indeed plays a significant role in the modification of the bonding structure of the BP material. Future work is required to fully understand the beam interaction and to fully investigate the interaction of BP with solvents to reduce the decomposition of this material when exposed to oxygen-rich environments.

5 *In-situ* TEM synthesis and phase engineering of PbO - a black phosphorous analogue

5.1 Introduction

Post-transition metal monoxides (PbO, SnO, etc.) and monochalcogenides (ie.e SnS, GeS, SnSe and GeSe, etc.) are a class of 2D layered materials which are isoelectronic to phosphorus, while displaying at the same time similar properties and polymorphism.

Due to the stability issues in BP discussed in Chapter 4, PbO was chosen as an alternative material for our studies.

Lead oxides have long been known and used as important conducting materials in photovoltaic devices, transparent conducting films, gas and optical sensors, and X-ray imaging detectors

owing to their interesting optical and electronic properties [74][75][76]. Among the numerous lead oxides, lead monoxide is the most significant one which exists in more than several polymorphs, and several other infrequent modifications.

Litharge, the red tetragonal α-PbO is the polymorph stable at room temperature; massicot, the yellow orthorhombic β-PbO is stable at 488 °C. Both of them adopt similar open-packed rocksalt-

like structures which arise from the stereo-chemically active lone pair of Pb2+, but with different orientations and distortions of PbO4 pyramid units (Figure 5-1). Thus, they show different band gaps (1.92 eV for a-PbO and 2.7 eV for b-PbO), making them distinct for various applications.

The diversity of PbO structures affords alternative advantages in specific usages. The interest for lead oxide and nano-lead oxide in the Nicolosi group raised from their very strong potential as anodes in lithium rechargeable batteries [77].

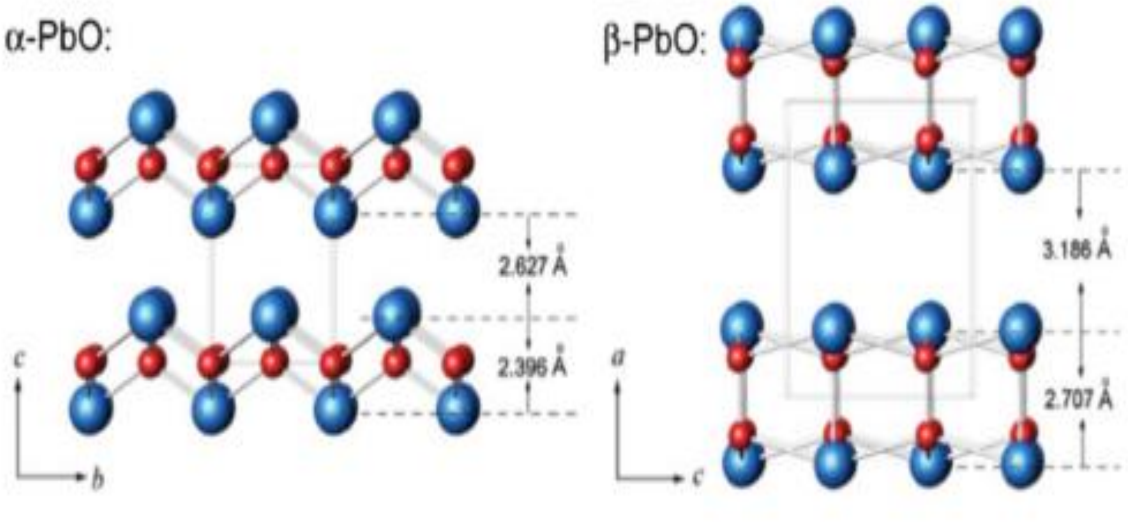

Figure 5-1 Crystal structures of α-PbO (P4/nmm, a = 3.9748 Å, c = 5.0227 Å, ICSD- 94333) and β-PbO (Pbcm, a = 5.8931(1) Å, b = 5.4904(4) Å, c = 4.7528(1) Å, ICSD-60135). Pb atoms are shown as blue spheres and O atoms in red. The distances of adjacent Pb layers are drawn with lines for contrast[78].

We decided to start studying PbO straight from its precursor of origin, $PbCO_3$ nano-sheets, a material that appears to be stable and safe to handle both in organic solvents and oxygen-rich environments. Synthesis and phase transformation of bulk PbO have already been discussed in literature and constitute the starting point of this study [78] [79] [80]. It has been reported in literature that when $PbCO_3$ is heated (ex-situ) at 315°C it converts to tetragonal α-PbO; further (ex-situ) heating of α-PbO induces a further transformation to orthorhombic β-PbO (Massicot or yellow lead oxide) occurring at 488°C [78].

Figure 5-1 shows the crystal structures of α-PbO and β-PbO and their respective interlayer, intra layer spacing. In this 5th chapter I discuss the *in-situ* TEM thermal decomposition of $PbCO_3$ leading to the formation of α-PbO and β-PbO, as well as the potential electron beam contribution in such phase transformations.

Whilst substantial amount of work has been performed in the phase engineering of transition metal dichalcogenides [81], this work is the first of this kind on novel IV-VI exfoliated compounds. We are hoping that this work will trigger new directions in the field of *in-situ* phase engineering of layered 2D materials.

5.2 Experimental Details

In-situ TEM was carried out on $PbCO_3$ hexagonal flakes (purity ≥99.99%, powder) purchased from Sigma-Aldrich, the DENS solutions Wildfire^{TM} heating holder in a FEI Titan300 operated at 300kV and 80kV was used for these experiments. The e-beam contribution to the induced phase transformations was also studied. In order to do so, I worked in two different regimes: “beam-off”, meaning that the sample was heated while blanking the beam, and turning it on only for imaging post-heating; and “beam-on”, meaning that imaging was carried out while the sample was heated. The *in-situ* evolution of the $PbCO_3$ nanoflakes at normal column temperature was studied both as a function of joule heating (*beam-off* condition) and a combination of joule heating and heating due to the electron beam (*beam-on* condition).

The *beam-off* condition was done by heating the sample to the desired temperature at a rate of 50 °C/min, staying at that temperature for 10 minutes and cooling down to column temperature at the same rate. Samples were then imaged only after having been cooled down to column temperature to ensured minimal beam induced effects.

In order not to miss any given transition, a very rigorous heating protocol was carefully designed and employed for the *beam-on* condition where samples were heated at extremely slow rate. A fast ramp rate was used (25 °C/min) at lower temperatures (< 250 °C) and a slower ramp rate was used (4 °C/min) at higher temperatures (> 250 °C). During the heating with *beam-on* condition, we always used a magnification of 620 kX and the beam was converged on to the specimen in order to ensure very high beam intensity.

5.3 Results and discussions

Figure 5-2 shows the phase transformations induced on a $PbCO_3$ flake in the *beam-off* condition after a heating regime as described in the experimental details paragraph. The original $PbCO_3$ hexagonal flakes figure 5-2(a) were characterized crystallographically using selected area electron diffraction (SAED in inset) and the lattice spacing are verified by using powder x-ray diffraction (PXRD) measurements figure 5.3(a) (b) (c). Additional XRD data on $PbCO_3$, α-PbO and β-PbO can be found in appendix 1(S4), (S5) and (S6).

Figure 5-2(b) shows a high-resolution image of the flake after this was heated *in-situ* in the *beam-off* condition up to 315 °C. The crystal appears to have transformed to α-PbO, as confirmed by the presence of the typical (001) 0.5nm spacing. This temperature-induced transition (no beam contribution) indeed happens at the same temperature reported for *ex-situ* experiments in bulk material [82].

Subsequent *in-situ* heating of the obtained α-PbO in figure 5-2(b) up to 488 °C (heating regime described in the experimental details paragraph) leads to a further phase transition to β-PbO. The material after this further heating step is shown in figure 5-2(c). The presence of crystal spacings of 0.59nm belonging to the (001) projection confirms that α-PbO has transformed to β-PbO. Once again, the temperature-induced transition from α-PbO to β-PbO indeed occurs at the same temperature reported for *ex-situ* experiments in bulk material[82].

In a further study, similar phase transformation were sought, this time in presence of a 300kV electron beam on during the whole duration of the experiment. At 300 kV, for all electron dose values used (1.5×10^5 Am^{-2}, 3.1×10^4 Am^{-2} and 7.7×10^3 Am^{-2}) the $PbCO_3$ material transformed directly into β-PbO at 300 °C. Figure 5-2(d) shows a typical high-resolution image of the material after such transformation. The α-PbO phase did not form under any circumstances under simultaneous heating and electron beam irradiation (beam-on set-up).

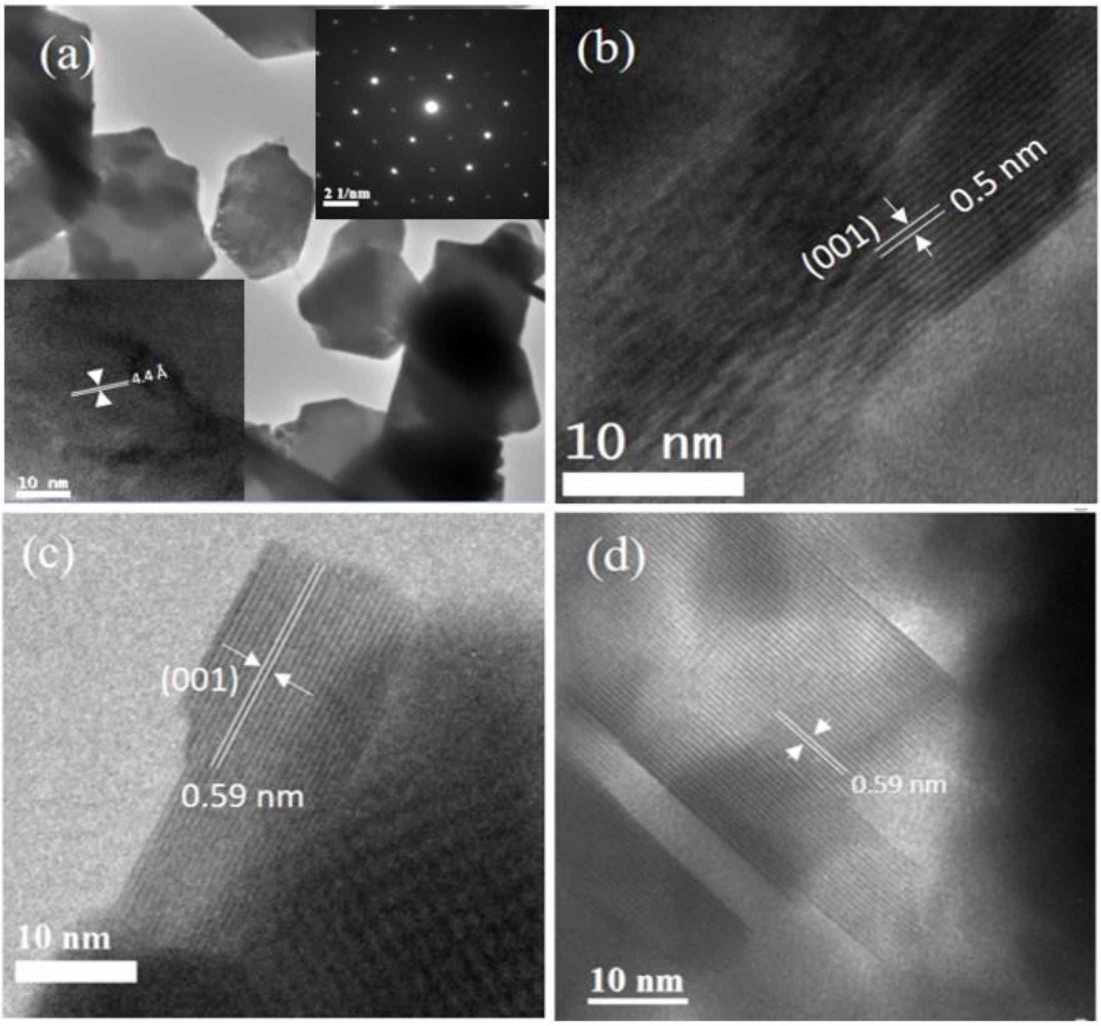

Figure 5-2: (a) Overview of the $PbCO_3$ flakes without any heating treatment. The insets show a high resolution image of a random $PbCO_3$ flake (bottom left inset) and its respective FFT (upper right inset); (b) The α-PbO formed after 315 °C in the beam-off condition and (c) the β-PbO formed in the beam-off condition after 488 °C; (d) The β-PbO form in the beam-on condition at 300 °C

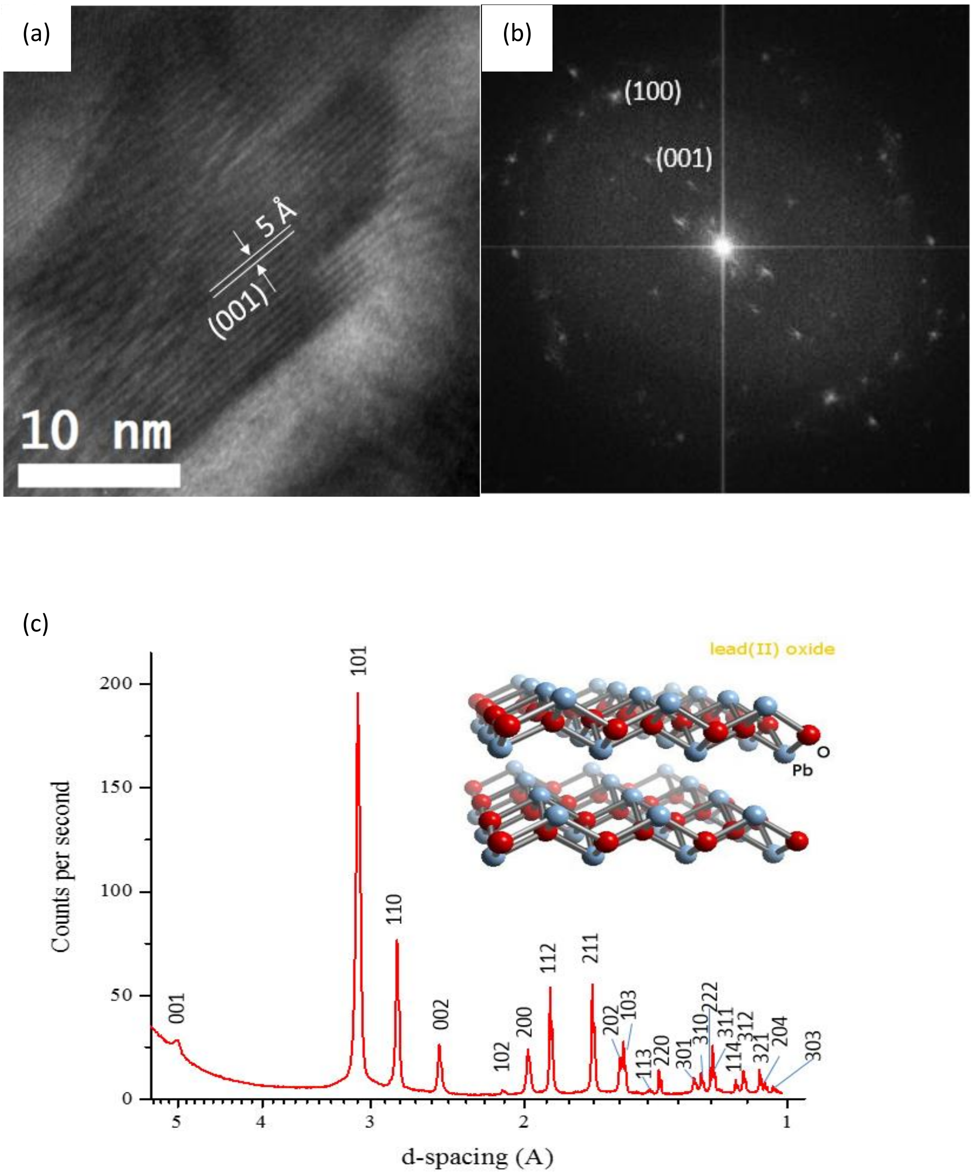

Figure 5-3(a) α-PbO high resolution TEM image, temperature ramped to 350^{o}C image taken at RT(b) (b) α-PbO diffractogram 350^{o}C (c) XRD spectra of α-PbO

A high-resolution high-angle annular dark field scanning transmission electron microscopy (HAADF STEM) image of the obtained orthorhombic β-PbO phase is shown in figure 5-4. This figure clearly shows the individual layers of the obtained orthorhombic β-PbO phase, imaged along the (010) zone axis.

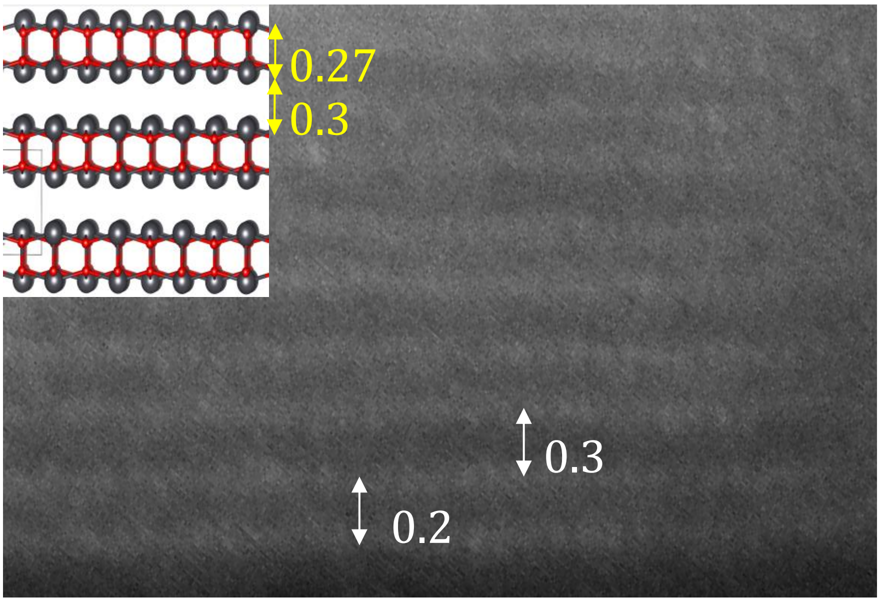

Figure 5-4 high-resolution high-angle annular dark field scanning transmission electron microscopy (HAADF STEM) image of β-PbO along the (010) zone axis. The intralayer spacing of 0.27 nm and interlayer spacing of 0.31 nm have been marked. The top left inset shows the schematic of β-PbO along the same zone-axis.

It is well known that at lower electron beam acceleration voltages, there is higher inelastic scattering cross section which results in higher sample heating leading to radiolysis of the specimen. In order to see the effect on the $PbCO_3$ and PbO phase transformations, the same set of experiments was repeated at 80kV.

At 80 kV, the phase transition to β-PbO occurred at 260 °C in the beam-on state compared to the observed β-PbO phase transition at 300°C at 300kV, which means that heating due to the presence of a lower 80kV electron beam only had a moderate effect on the decomposition temperature of $PbCO_3$. Phase transition from $PbCO_3$ to β-PbO also occurred at 488 °C in the beam-off state as outline in Table 1 below. In this context, it should be noted that the thickness of the starting $PbCO_3$ flakes used was very uniform. Therefore, the effects due to heating and presence of the electron beam were consistent in all experiments. All the described experiments led to a decrease in the thickness of the flakes, and as a consequence to better quality of phase contrast images as seen in figure 5-2(c) and (d).

Table 1 gives a summary of the executed experiments and the noted phase transition temperatures as a function of temperature, electron beam voltage and electron dose.

Table 1.*The decomposition temperature of $PbCO_3$ to orthorhombic β-PbO as a function of acceleration voltage and electron beam dose*

Acceleration voltage (kV)	Electron dose (Am^{-2})	Decomposition temp (°C)	Phase
300 kV	1.5×10^5	300	β-PbO
300 kV	3.1×10^4	300	β-PbO
300 kV	7.7×10^3	300	β-PbO
80 kV	5×10^4	260	β-PbO
Beam-off	-	315	α-PbO
Beam-off	-	488	β-PbO

Electron beam damage can be of 3 types; 1) radiolysis, 2) knock-on damage or 3) electron beam heating. For a field emission gun (FEG) source, and for insulators with moderate to good thermal conductivity, like PbO, the electron beam heating can be negligible. The primary way, semiconductors will be chemically modified is by radiolysis. The inelastic scattering of the electron beam with the $PbCO_3$ flakes initiates inter-band transitions. This inter-band transition from the valence band to the conduction band can change the valence chemistry of the specimen and can lead to different reaction pathways. Dynamic changes in chemistry due to radiolysis had been observed previously in transition metal dichalcogenides (WS_2) where formation of metal-metal bonds results in one-dimensional chains in the zigzag direction[83]. In order to corroborate our findings and better understand the role of the electron beam we performed further studies. Figure 5-5(a) shows the tetragonal α-PbO as formed and observed at 407 °C in a region of the MEMS chip that had not been exposed to any electron beam radiation whatsoever (same effect as the *beam-off* set-up).The flake was then subjected to e-beam irradiation (dose of 5×10^4 Am^{-2}) for an additional period of 33 sec, we subsequently observed a transformation to orthorhombic β-PbO phase. The flake after such e-beam exposure is shown in figure 5-5(b). Distinct lattices fringes can be seen in the HRTEM image 5-5 (b), the average lattice distance was measured to be 0.31nm. This crystal arrangement shows that the crystal size is 0.31 nm, which is in agreement with the domain peak of XRD (0.306 nm) in table 2 which is close to the inter-planar spacing between (101) crystal facets of β-PbO and confirms the formation of the nanostructure [84].

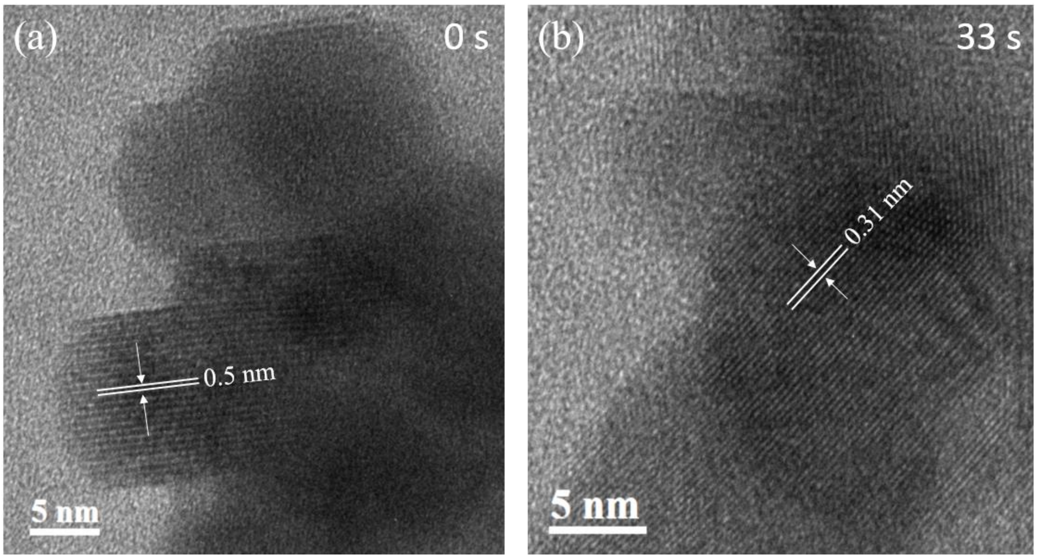

Figure 5-5 (a) α-PbO observed at 407 °C in a region not exposed to electron beam (b) The same area transforms into β-PbO after 33 s of electron beam exposure with a dose of 3.1×10^4 Am^{-2}.

Table 2. *XRD data and particle sizes of sol-gel synthesized PbO* [84]

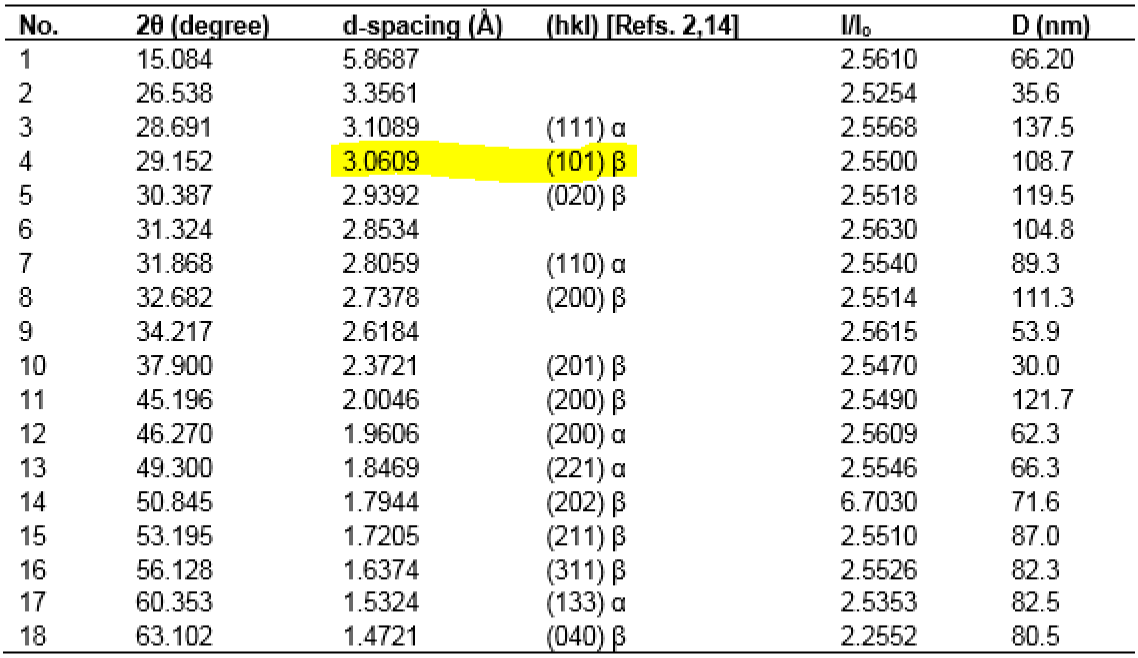

No.	2θ (degree)	d-spacing (Å)	(hkl) [Refs. 2,14]	I/I$_o$	D (nm)
1	15.084	5.8687		2.5610	66.20
2	26.538	3.3561		2.5254	35.6
3	28.691	3.1089	(111) α	2.5568	137.5
4	29.152	3.0609	(101) β	2.5500	108.7
5	30.387	2.9392	(020) β	2.5518	119.5
6	31.324	2.8534		2.5630	104.8
7	31.868	2.8059	(110) α	2.5540	89.3
8	32.682	2.7378	(200) β	2.5514	111.3
9	34.217	2.6184		2.5615	53.9
10	37.900	2.3721	(201) β	2.5470	30.0
11	45.196	2.0046	(200) β	2.5490	121.7
12	46.270	1.9606	(200) α	2.5609	62.3
13	49.300	1.8469	(221) α	2.5546	66.3
14	50.845	1.7944	(202) β	6.7030	71.6
15	53.195	1.7205	(211) β	2.5510	87.0
16	56.128	1.6374	(311) β	2.5526	82.3
17	60.353	1.5324	(133) α	2.5353	82.5
18	63.102	1.4721	(040) β	2.2552	80.5

Another interesting, electron beam induced effect in PbO is the amorphous to orthorhombic crystalline phase transformation which happens at room temperature solely by irradiating the area with the electron beam at 300 kV (at various doses).

When the specimen is heated to over 600 °C in the *beam-off* condition or when the specimen is heated to over 415 °C (at 300 kV) in the *beam-on* condition, an amorphous phase forms. Figure 5-6 (a) shows the amorphous PbO phase formed at 415 °C (at 300 kV) in the *beam-on* condition. This amorphous phase appeared perfectly stable under continuative exposure to the electron beam for a further 52 sec (while keeping the temperature at 415 °C). In a second-step of the experiment we switched off the heating element and allowed the system to cool down to room temperature; when we exposed this amorphous system again under the 300KV electron beam, the orthorhombic phase shown in figure 5-6(b) formed instantaneously.

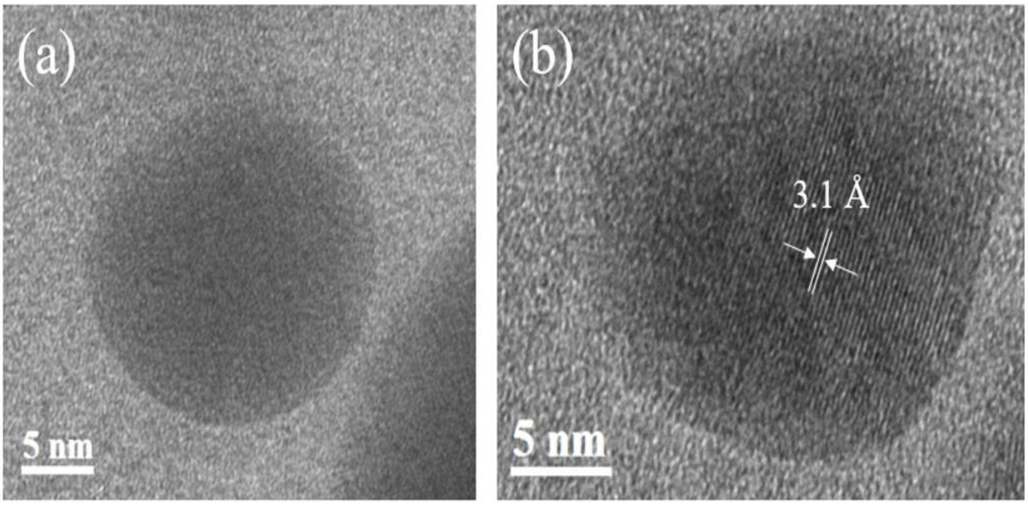

Figure 5-6 (a) Amorphous PbO at 415 °C imaged under an electron beam of dose 3.1×10^4 Am^{-2} at 300 kV. (b) The same amorphous sample after cooling to column temperature re-crystallises into α-PbO after exposure under a 300kV electron beam.

It is interesting to note that the same transformation from amorphous to crystalline α-PbO phase did not happen when the samples were irradiating with 80 kV electron beam.

Similar e-beam induced amorphous to crystalline phase transformation were reported at room temperature for $SrTiO_3$ [85]. Knock-on process had been found responsible in that case, based on molecular dynamics simulations. We also propose that knock-on is responsible for the amorphous to crystalline phase transformation in PbO. The very fact that an 80 kV electron beam could not instigate the amorphous to crystalline phase transformation makes us to believe that this is indeed a plausible explanation [46].

5.4 Conclusions

We have studied the thermal decomposition of $PbCO_3$ nano-flakes and the phase transformation into tetragonal PbO (α-PbO) and its further phase transformation into orthorhombic PbO (β-PbO) *in-situ* TEM. Performing a systematic study as a function of beam dose and beam acceleration voltages, we have found that a radiolysis process is responsible for the direct decomposition of $PbCO_3$ into orthorhombic β-PbO at 300 °C, whilst a knock-on process is involved in the amorphous to crystalline orthorhombic β-PbO phase transformation observed under the electron beam at room temperature.

We have shown how the thermal decomposition temperature of nano-flakes of $PbCO_3$ into tetragonal PbO (α-PbO) and its further phase transformation into orthorhombic PbO (β-PbO) happen around the temperatures reported in the literature for bulk (at 315 °C and 488 °C respectively) when an electron beam is not used.

However, when the phase transformations are accompanied by the presence of the electron beam, the same transition appear to occur at lower temperatures. In presence of an electron beam at 300 kV (with varying doses of 1.5×10^5 Am^{-2}, 3.1×10^4 Am^{-2} and 7.7×10^3 Am^{-2}), the orthorhombic β-PbO forms at temperatures as low as 300 °C; whilst in presence of an electron beam accelerated at 80 kV (dose= 5×10^4 Am^{-2}) the decomposition to orthorhombic β-PbO happens at around 260 °C. These findings show that the decomposition of $PbCO_3$ nano-sheets and the further induced phase transitions to tetragonal PbO (α-PbO) first, and orthorhombic PbO (β-PbO) afterwards, do not appear hugely dependent on electron dose and are only moderately affected by acceleration voltage.

Moreover, we demonstrated that amorphous PbO can be transformed into the orthorhombic crystalline form (β-PbO) in a controlled fashion solely by irradiating the sample with the electron beam (without any further thermal heating applied).

Our results proof that in-situ TEM can indeed be used to locally engineer the phase transformation of PbO and analogous materials.

6 Alternative methods under investigation to produce PbO

6.1 Method of producing PbO hexagonal nano-sheets by electrodeposition

One of the ongoing goals of my research is to investigate the electrical behavior of PbO *in-situ* using DENS MEMS chips. Whilst the material subject of my studies in Chapter 5 was perfectly suitable for monitoring phase transitions it demonstrated to be unsuitable for allowing efficient electrical testing. For that, the production of large, impurity-free material is crucially needed.

Dr João Coelho in the Nicolosi group is currently working on establishing new synthetic routes based on electrodeposition.

The electrodeposition technique was repeated several times using deposition potentials ranging from 1.0 V to 2.0V while varying the deposition times ranging from 15 min to 40 mins.

Hexagonal nano-sheets were more evident in the samples produced in the voltage potential range 1.3v to 1.5V and in the 20-30 mins time period. Figure 6-1 shows large hexagonal PbO nano-sheets with a typical lateral size in the range of 100nm-1µm and with a thickness in the range of 50-100nm.

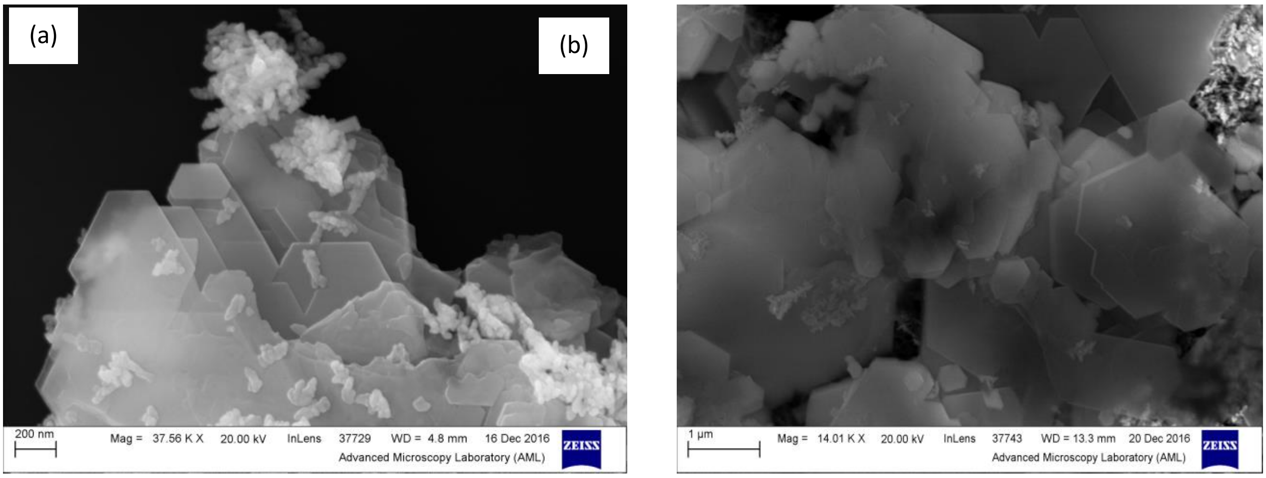

Figure 6-1 (a) (b) large crystalline hexagonal nano-sheets produced by electro deposition

A large variation was observed in the quality of the nano-sheets and their physical size and thickness by varying the process parameters as shown in figure 6-2. More experimental investigation is required to optimize this electrochemical process in order to being able to produce material in a controllable manner (i.e. control over the size and absence of undesired by-products and impurities).

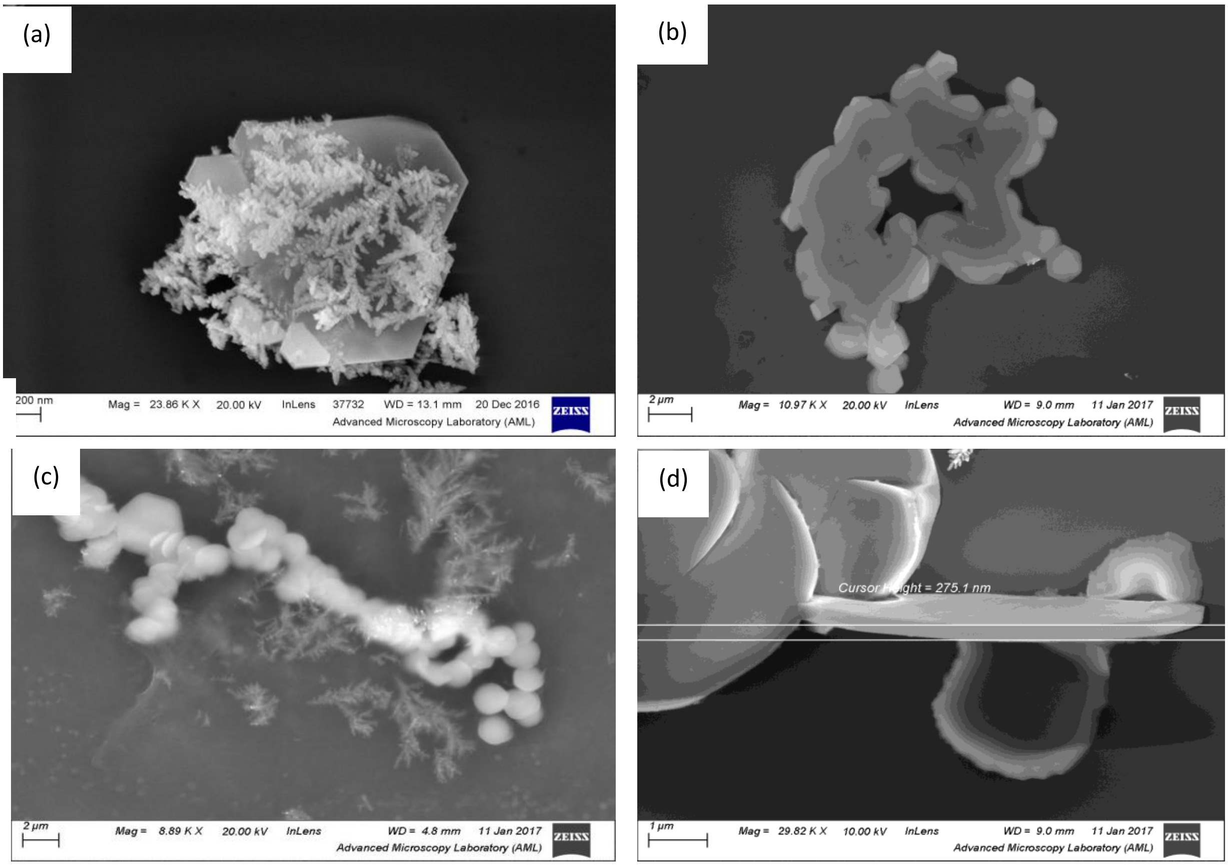

Figure 6-2 (a) (b) (c) (d) SEM images of the electrodeposited PbO material showing a very large lateral size and thickness variation.

High resolution TEM characterisation however confirmed the successful growth of crystalline hexagonal nano-sheets of PbO. A typical image and the corresponding diffraction patterns are shown in figure 6-3.

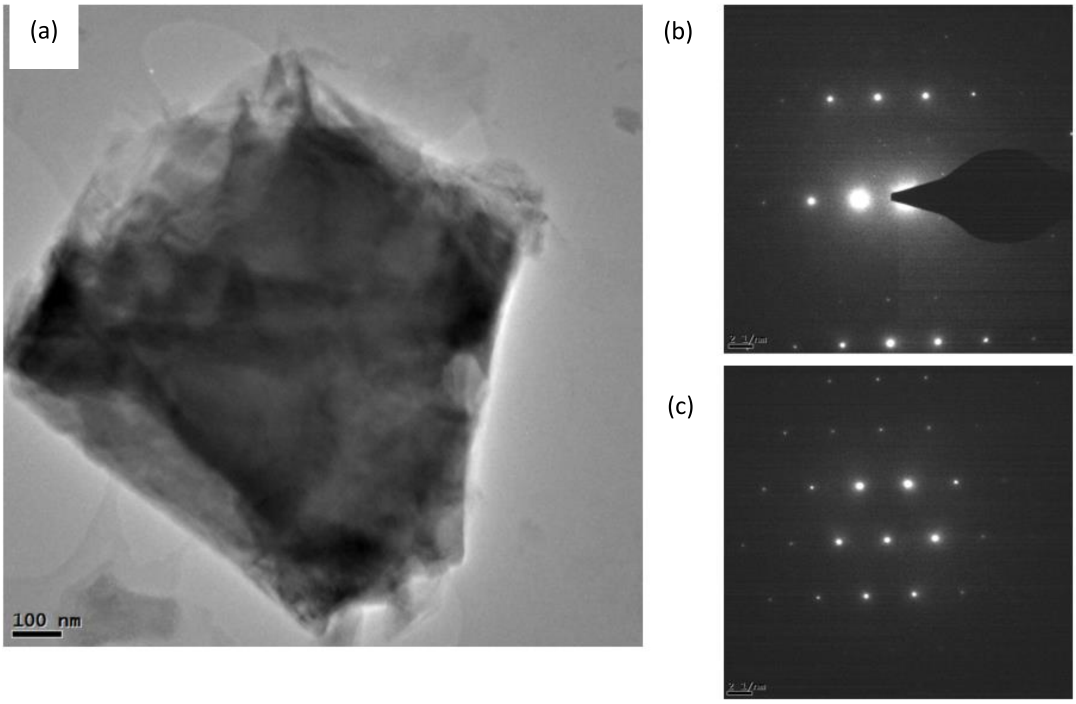

Figure 6-3 (a) TEM image of single PbO sheet and (b) (C) corresponding diffraction pattern.

However, optimization of growth is essentially still required to increase the yield of single large crystals which in turn will enable me to carry out the planned electrical and heating experiments.

In parallel to this on-going optimization of growth by electrodeposition, I have established a collaboration with Mr. Stephen Porter in the Stamenov group in TCD to attempt growth of PbO by Pulsed Laser Deposition.

7 Novel Lamella preparation technique for applications such as *in-situ* heating experiments and sample characterization

7.1 Introduction

In-situ experiments in relation to transmission electron microscopy are vitally important to the world of material science. Seen as *in-situ* preparation is becoming such a paramount aspect of research, sample preparation and the techniques in which samples are preparation is vital. Creating the correct technique and optimising these techniques for the various materials is crucial.

Here an novel *in-situ* lift-out procedure, using focused ion beam milling, is proposed for the preparation of lamella for *in-situ* heating experiments in the transmission electron microscope. This novel method involves the use of a rotating micro-grippers (tweezers) during the lift-out procedure as opposed to the traditional micromanipulator needle and Pt weld. Using rotating grippers and a unique adhesive substance, SEMGlu, lamellae are successfully mounted onto a MEMS chip for *in-situ* TEM heating experiments. Lamellae are prepared using a low kV voltage and wedge technique in order to reduce amorphisation within the sample. The technique is demonstrated using a PbO sample prepared by Pulsed Laser Deposition by Mr. Stephen Porter in the Stamenov group in TCD. The technique here described has an number of advantages over traditional FIB lamella sample preparation techniques [86][87][88]. Most alternative techniques produce samples that are larger in size and non-uniform thickness in the area of analysis and require further thinning by FIB when placed on the MEMS heating chip. This can potentially damage the MEMS chip and cross contaminate the sample. Final milling of the lamella on the MEMS chips usually requires the FIB to be fitted with a flip stage. This method has the advantage over other techniques where much larger sample sizes are required and need the addition of a copper grid to support the lamella which can potentially acts as a heat sink. This preparation technique uses a smaller specimen sample, which is mounted directly onto the MEMS, without the need for the copper support grid. This results in a more even and more accurate distribution of heat throughout the sample during analysis.

Focused Ion Beam preparation is a commonly used form of sample prep as it is an efficient and reliable method of preparing electron transparent samples to a very high quality, with minimal damage, and good sample protection through the use of reduced beam voltages during thinning and platinum layer protection.

An alternative method for lamella lift-out for MEMS chip mounting has been established previously [88], however, the novel aspect of our technique is in relation to the method of transfer and securing of the lamella to the MEMS chip which removes the need for use of platinum weld and lowers the risk of damaging the chip window during the thinning process. By eliminating of the copper grid as a support substrate is an advantage as all the specimen final thinning is carried in a micro-gripper prior to the transfers of the specimen directly to MEMS chip, no further sample processing is required.

This new method not only provides a new method of preparation for lamellae for *in-situ* heating it also provides a novel way of preparing cross-sectional lamellae across many different analysis applications[89].

7.2 Experimental Methods

The following PLD process parameters were used to deposit the PbO thin film: substrate strontium titanate (STO) temperature=495°C; chamber oxygen pressure=10 mTorr; fluence ~6 J/cm2. It should be noted that STO substrate was used as this was the only substrate available at this preliminary experimental stage. In order to determine the best method for growing epitaxial α-PbO, a thorough study of the parameter space for pulsed laser deposition thin film growth is required. If we are to achieve highly oriented films with a single crystalline α-PbO phase further experimental analysis on various substrates such as STO, dysprosium scandate (DSO), and potassium tantalate (KTO) substrates is required. All microscopy sample preparation was performed in a Zeiss Auriga dual beam system. We utilized SEMGlu (Kleindiek Nanotechnik Gmbh, Reutlingen) for securing lamella to MEMS chip. Proof-of-concept In-situ TEM was carried out using a DENS solutions WildfireTM heating holder in a FEI Titan300 operated at 300kV and 80kV.

7.3 Lamella mounting method onto MEMS

This technique involves the mounting of lamellae onto a MEMS chip *in-situ* within a FIB/SEM system. Instead of using traditional method of attaching the lamella to a copper grid by platinum ion beam deposition this method utilises SEMGlu (Kleindiek Nanotechnik Gmbh, Reutlingen) for securing lamella to MEMS chip. SEMGlu is a vacuum-compatible glue that is cured by e-beam irradiation. A low electron beam current allows working with the glue under SEM observation. Increasing the magnification or the electron beam current causes the glue to harden. The electron beam voltage determines the penetration depth into the glue and thus the curing volume of the glue. MEMS chips as described in chapter 3 supplied from DENS solutions were mounted on a SEM stub using carbon tabs.

The application of SEMGlu and removal of lamella was performed using a roof mounted Kleindiek RoTip micromanipulator fitted with a micro-grippers for lamella lift-out. The ROTIP-EM is a rotational axis plug-in for the MM3A-EM micromanipulator. It enhances the system by providing a fourth degree of freedom that is ideal for this particular technique and for numerous other SEM and FIB applications.

7.4 MEMS Chip Preparation

A through-hole MEMS chip is mounted on a SEM stub using carbon tabs. 1 ml of SEMGlu is placed on a separate stub. The Zeiss Auriga stage is tilted to 54°, the eucentric point is found and the sample is brought to the coincidence point of 5 mm. A Kleindiek micromanipulator needle is dipped into the SEMGlu until there is a tear-drop shape portion at the tip of the needle as shown in figure 7-1(a) (b). The needle is slowly brought to the MEMS chip and lowered until the SEMGlu is in contact with the chip. The stage is then slowly moved in the x and y direction to gently drag the needle around the surrounding windows of the chip to deposit some SEMGlu. The more windows available for mounting the lamella, the higher the success rate of the lift-out.

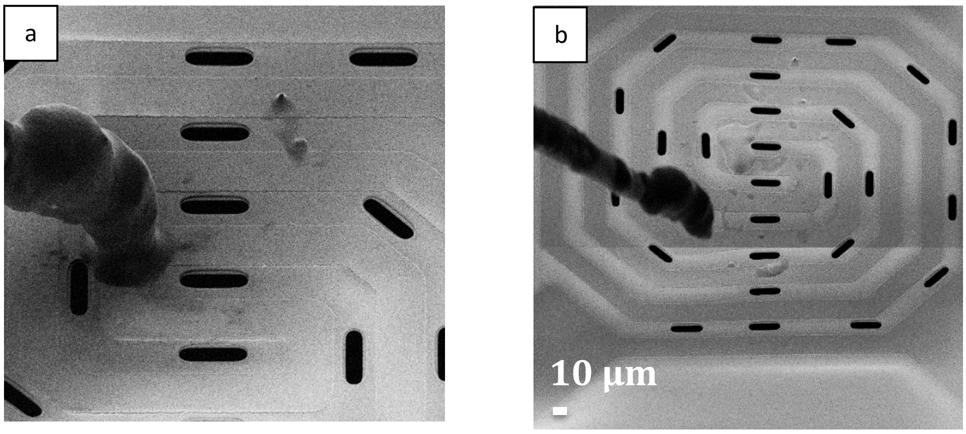

Figure 7-1 (a) (b) SEM images showing the application of SEMGlu around the surrounding windows of the MEMS chip using a Kleindiek micromanipulator needle.

7.5 Bulk Lamella Preparation

Once the SEMGLU has been deposited close to the windows on the MEMS chip in a number of locations, the needle with the SEMGlu is replaced with a micro-grippers with a RoTip attachment, which provides full 360° rotation. The bulk lamella preparation procedure is similar to that of Langford et al, Schaffer and outlined below. Both e-beam and I-beam platinum deposition is performed with an area of approx. 2 x 22 micron figure 7-2(a). Once the protective platinum layers have been deposited, the trenches are milled to a depth of approx. 10 microns figure 7-2(b). The undercut is performed at a tilt of 7 °C as shown in figure 7-2(c).

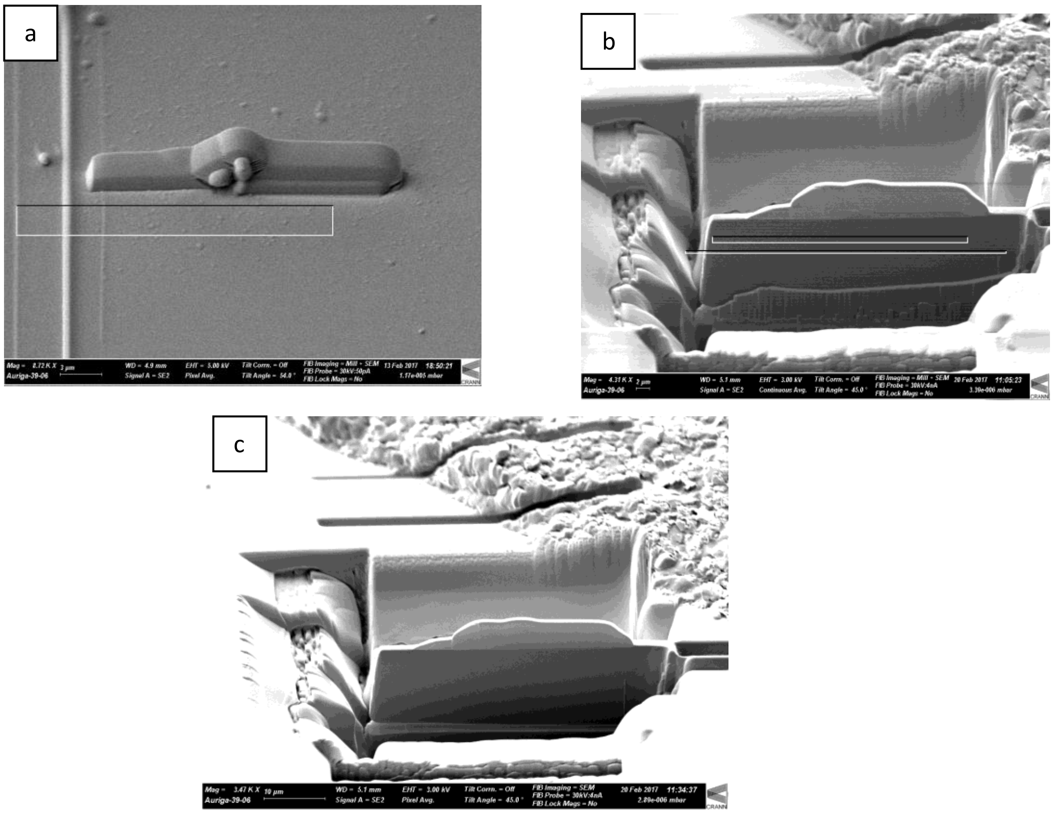

Figure 7-2 (a) e-beam Pt deposition, I-beam Pt deposition, (b) large trenches and side trench (c) undercut

Once the lamella is prepared in the bulk, the micro-gripper are then inserted. Fig 7-3(a) (b) shows both SEM and FIB images of the correct positioning of the grippers with respect to both the SEM and FIB beams. The grippers should be parallel with the FIB beam, for ease of use when it comes to the lift-out. The grippers should be at an approximate tilt of 54° to be parallel with the FIB beam. This correct positioning is roughly done by eye when positioning the micro-gripper in the chamber at air and then finely tuned using the Kleindiek RoTip.

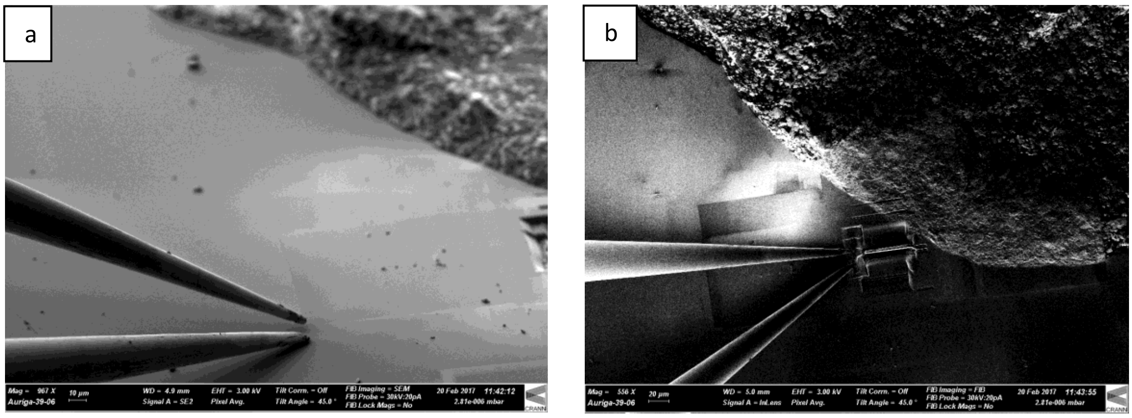

Figure 7-3 (a)(b) showing SEM & FIB images respectively of the correct positioning of the micro-gripper prior to lift-out

7.6 Gripping & Removing Lamella using Kleindiek Micro-gripper

The rotating tweezers is slowly inserted near the bulk lamella figure 7-4(a). Before finally reaching the lamella it is opened to allow room for the lamella to easily fit in between the two grippers figure 7-4(b).

By toggling between the SEM & FIB the lamella is placed between the two sides of the gripper. The grippers are slowly lowered & inserted. Once in the correct positioning, the grippers are slowly closed until they begin to slide along the lamella. Once the lamella is secure, the remaining sidewall connected to the bulk is removed using a 30 kV 2nA FIB beam. A slight shift in the lamella position may be noticed when it has been released from the bulk. At this point it is good to check that the lamella is secure within the grippers by tightening the grip after the mill. The grippers are slowly lifted up and out of the trench with a firm grip of the lamella figure 7-4(c). Once the bulk sample has been lowered, by lowering the z height, the lamella is imaged in the FIB to begin the thinning process.

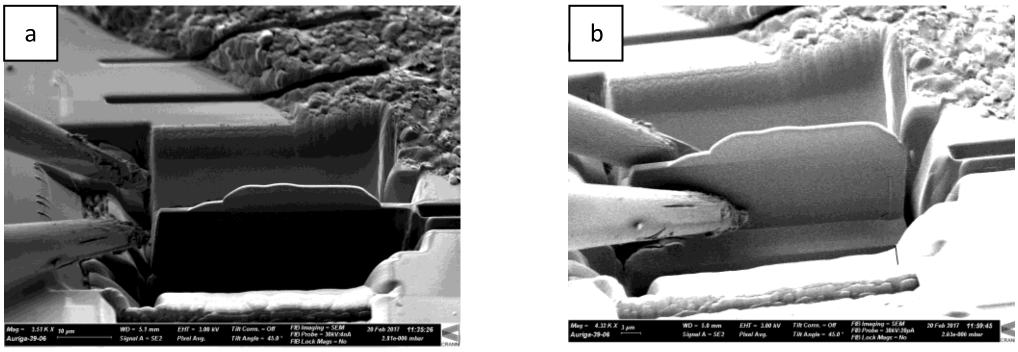

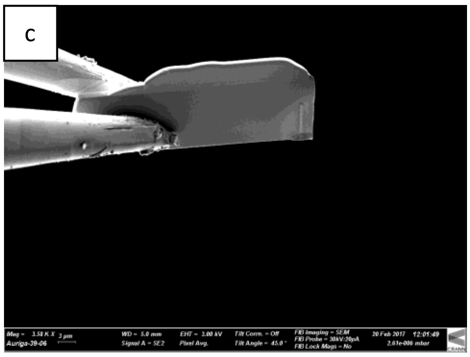

Figure 7-4(a) SEM images taken at 3 kV showing the micro-gripper approaching the lamella (b) gripping lamella (c) lifting out lamella from the bulk sample

7.7 Thinning & Transfer of the Lamella to MEMS Chip

Using the rotating grippers, the lamella is tilted between 3° – 5° with respect to the FIB. The lamella is then successively milled by adopting a staggered technique using a range of decreasing beam energies from 30 kV 240pA, 15 kV 200pA to 5 kV 20pA as shown in figure 7-5(a)(b)(c)(d)(e) [90] . The staggered approach allows parts of the lamella to remain untouched in the thinning process, which provides support to the thin regions but also creates a gap between the thinned area of interest of the lamella and the chip/chip window. It elevates the area of interest, while still maintaining a parallel geometry between the chip window and the lamella surface.

Once the area of interest has been thinned to approx. 70 – 100nm thickness, which appears white at 5kV in SEM mode, the SEM accelerating voltage is dropped to 3 kV and it is polished further until it appears white at this setting, which indicates it is approx. 50 – 70nm thick figure 7-5(f).

The use of the RoTip micro-grippers provides many advantages over the current conventions that perform final thinning of the lamella when the lamella is mounted on the MEMS. Final milling of the lamella on the MEMS chip at difficult tilt angles can result in ion beam damage of the MEMS chip [88]. The outline novel technique has the advantage that both sides of the lamella can be successfully milled without the obstruction of the MEMS chip itself or without causing potential damage such as to the area surrounding the MEMS chip window. The grippers also ensure there is no sputtering or re-sputtering of Pt due to welding, as no Pt weld is needed. It also eliminates the need for the lamella to be attached to a copper grid as the final thinning is done in the gripper and the lamella is transferred directly to the MEMS chip using the gripper.

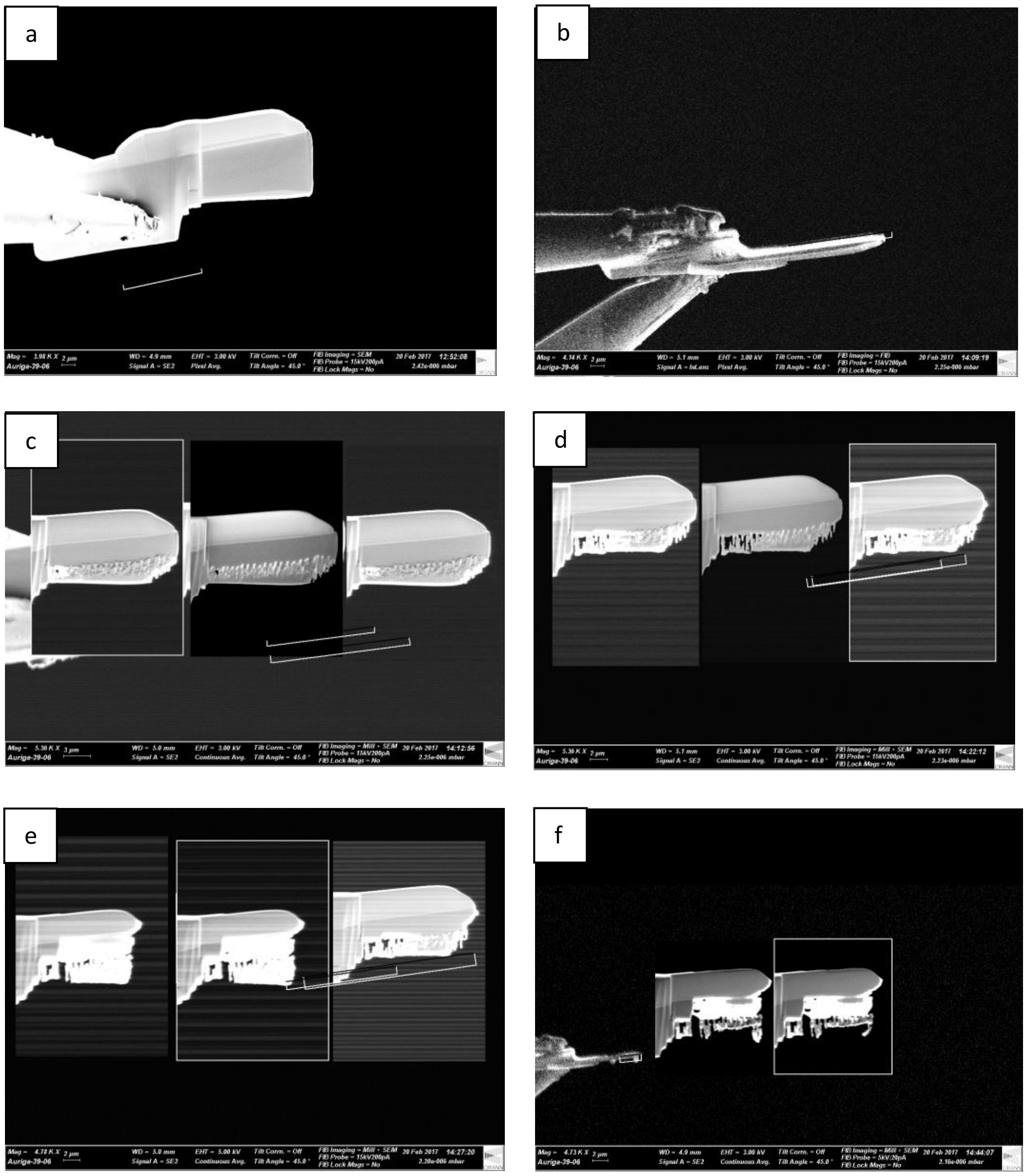

Figure 7-5 (a) (b) SEM images showing the final stages of the thinning & polishing process of the lamella (c) & (d) displaying the classic staggered approach to the thinning process, allowing the thicker segment to create a gap between the thin part of the lamella and the surface of the chip, (e) the lamella thinned at 15 kV 200pA and (f) at its final stages of polishing with a 5 kV 20pA beam. In figure 7.5 (c) (d) (e) (f) the highlighted rectangular frame indicates the live selected milling area of the lamella in each figure.

Once the lamella has been thinned & polished sufficiently, the stage is tilted back to 0° and moved to bring the MEMS chip to the 5 mm coincidence point. Having the stage at 0° tilt means the lamella will be in a better position to lie flat over the window of the MEMS chip, as the angle between the top of the lamella and the chip is being reduced below 90°. The lamella is transferred in the micro-gripper to the area of the MEMS chip were the SEMGlu has been placed, the lamella thinned region is placed directly above the window as show in figure 7-6(a) (b).

It is important to note during the transfer of the lamella to the MEMS the SEM accelerating voltage is kept at 3 kV, the aperture reduced from 120µm to 7.5µm and high current mode is switched off. This is to prevent /

reduce charging any possible between the sample, gripper and chip. It also prevents the SEMGlu curing/hardening before the lamella is placed over one of the chip windows.

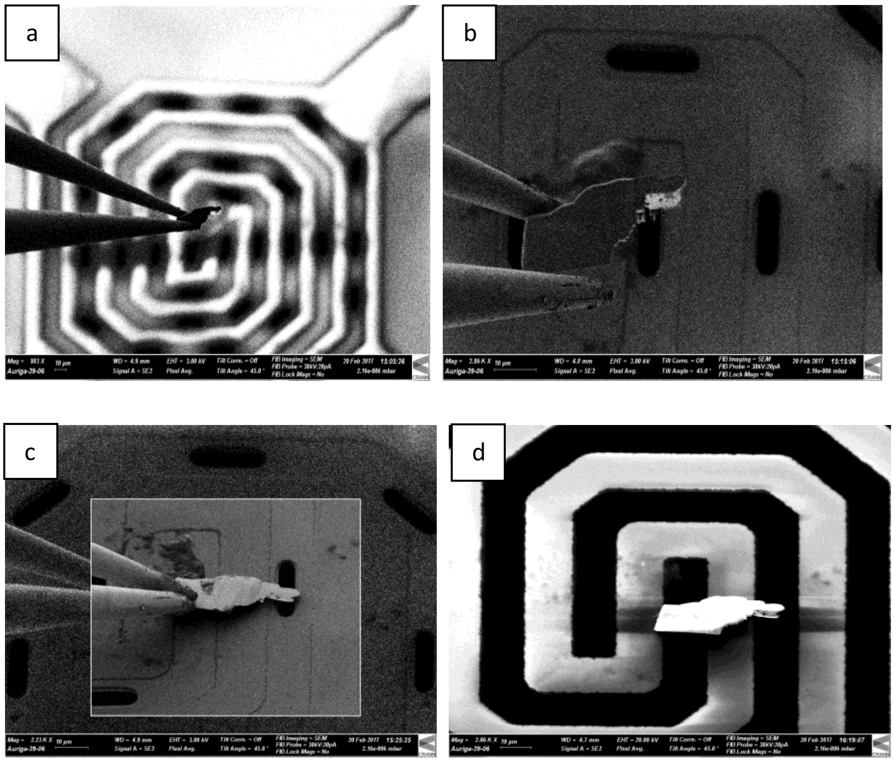

Figure 7-6 (a)(b) showing the transfer of the lamella from the grippers to the MEMS chip, (c)(d) images showing the high kV curing of the lamella and SEMGlu

7.8 Results & Discussion

The MEMS chip is mounted and secured in the DENS solutions heating holder. The lamella has remained over the desired window and has been successfully thinned to a very high standard, providing minimal damage and enabled us to obtaining high resolution images. A detailed publication of this novel in-situ lamella fabrication technique for *in-situ* TEM is available:- M. Canavan, D. Daly, A. Rummel, E. K. McCarthy, C. McAuley, and V. Nicolosi, "Novel in-situ lamella fabrication technique for in-situ TEM," *Ultramicroscopy*, vol. 190, pp. 21–29, 2018'' [89]. Table 3 below gives a complete set of parameter for lamella preparation using this technique.

Table 3. Complete set of parameters for lamella preparation

Preparation Step	Primary Mode	SEM Voltage	E-Beam Current	FIB Voltage	I-Beam Current	Depth	Tilt	Details
MEMS device preparation	Imaging: e-beam	5 kV	3 nA				54°	Using the manipulator needle, SEMGlu is applied carefully around the windows of the MEMS device
EBID-Pt	Deposition: e-beam	5 kV	3 nA			0.5–1 µm	54°	Thickness of 2 µm × 22 µm
IBID-Pt	Deposition: i-beam	5 kV	3 nA	30 kV	20 pA	1.5–2 µm	54°	Thickness of 2 µm × 22 µm
Trenches	Milling: i-beam	5 kV	3 nA	30 kV	4 nA	15 µm	54°	Dimensions of 40 µm × 50 µm × 15 µm
Side Trench	Milling: i-beam	5 kV	3 nA	30 kV	4 nA	15 µm	54°	Dimensions of 30 µm × 10 µm
Undercut	Milling: i-beam	5 kV	3 nA	30 kV	2 nA	3–4 µm	7°	Dimensions of 1 µm × 24 µm
Final sidewall removal	Milling: i-beam	5 kV	3 nA	30 kV	2 nA	15 µm	54°	Dimensions of 2 µm × 2 µm
Lamella lift-out	Imaging: e-beam	5 kV	3 nA	30 kV	20 pA		54°	Sample lifted out using microgrippers
Thinning in RoTip microgrippers – Stage 1	Milling: i-beam	5 kV	3 nA	30 kV	240 pA		58 - 59°	Milled to a thickness of approximately 700–800 nm (4 – 5° tilt with respect to FIB)
Thinning in RoTip microgrippers – Stage 2	Milling: i-beam	5 kV	3 nA	15 kV	200 pA		58 - 59°	Milled to a thickness of approximately 200–300 nm (4 – 5° tilt with respect to FIB)
Thinning in RoTip microgrippers – Stage 3	Milling: i-beam	3/5 kV	3 nA	5 kV	20 pA		57 - 58°	Milled to a thickness of approximately 50–70 nm (3 – 4° tilt with respect to FIB)
Transfer of lamella to device	Imaging: e-beam/i-beam	3 kV	10 pA	30 kV	20 pA		0°	Lamella and MEMS device both at coincidence point. SEM voltage and beam current lowered to reduce charging and prevent any unnecessary curing of the SEMGlu prior to the final stages of the transfer.
Securing lamella over MEMS device window	Curing: e-beam	30 kV	6 nA				0°	Lamella successfully placed over the window. Thicker end of lamella over SEMGlu exposed to a high beam voltage for approximately 30 minutes to ensure a secure placement.

7.9 HRTEM imaging of PbO lamella

HRTEM imaging was performed on the PbO lamella mounted on the MEMS chip. The lamella was imaged over a through hole of the MEMS chip at 300KV in TEM.

Figure 7-7(a) shows an overview TEM image of the PbO lamella. The red arrows indicate the various layers, STO substrate, PbO deposited layer and the platinum deposited protection layers (b) shows the high resolution TEM images of the PbO sample and STO substrate, demonstrating the high quality sample obtained from the FIB milling.

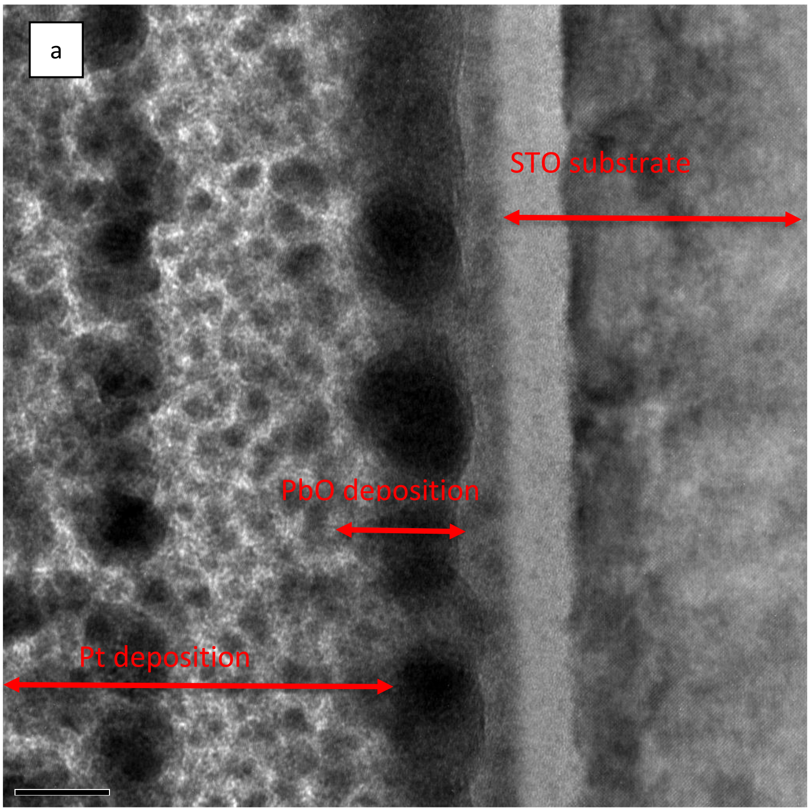

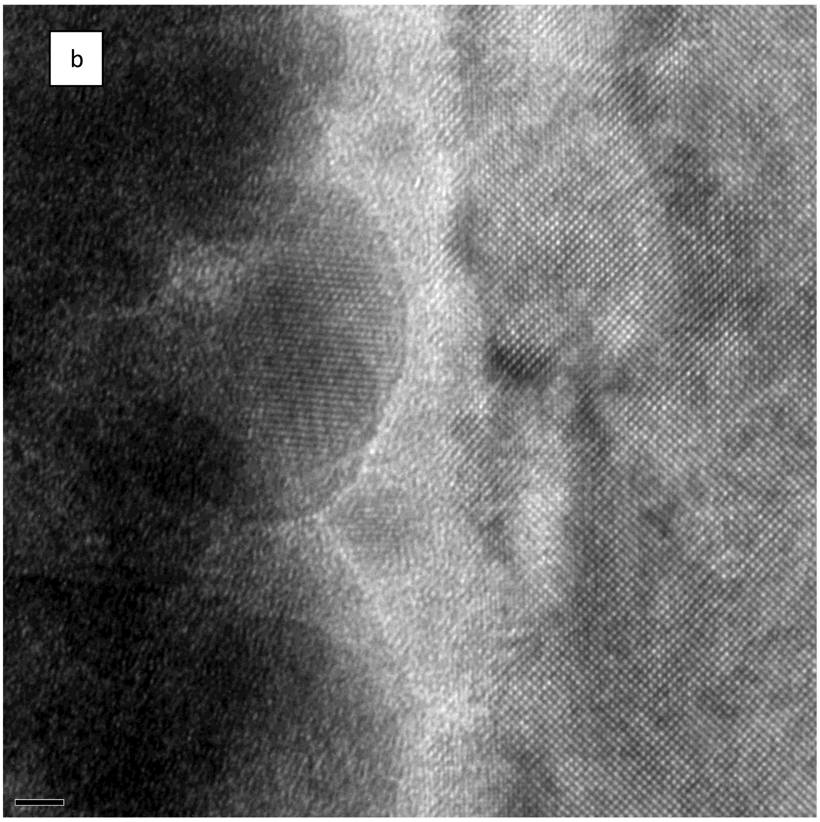

*Figure 7-7 (a) shows an overview TEM image of the PbO lamella (b) HR*TEM image of PbO lamella placed over the through-hole window

7.10 Heating experiment

The lamella was heated on the MEMS chip at a continuous slow ramp rate (120 mins) from 25°C to 436°C to allow TEM images to be taken a various intervals. The goal of the experiment was to observe a phase change in PbO in a single crystalline region of the lamella. Changes in the structure of the material was observed during the heating experiment as is evident from the figures 7-8, however an obvious phase change was not observed and future work is required to determine whether or not a phase change is taken place on the pulsed laser deposited PbO material as observed in the $PbCO_3$ nano-flakes used in the other experiments outlined in chapters 4, 5 and 6. It should be also noted that the experimental method using pulse laser deposition to deposit the PbO in this instance was not idea. To obtain α-phase PbO deposition by PLD the substrate selection and process parameter are critical.

Figure 7-8 shows TEM images of a large crystalline area of the lamella at a series of temperatures.

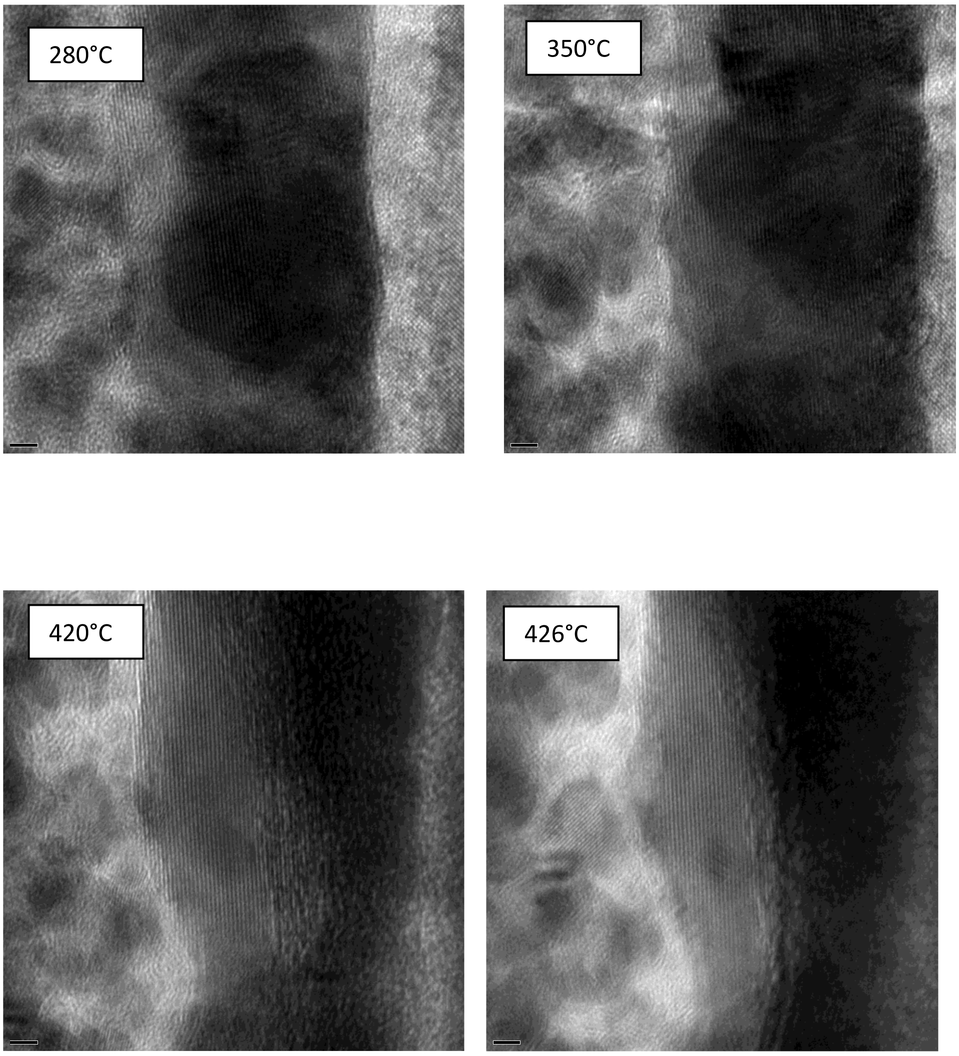

Figure 7-8 TEM images of PbO Lamella during heating experiment.

A thorough study of the parameter space for pulsed laser deposition thin film growth is required if we are to successfully observed phase changes during heating experiments on deposited PbO films on various substrates. It is most likely the film deposited was not highly oriented α-PbO as it was deposited on a strontium titanate substrate. The lattice mismatch STO substate and α-Pbo does not seem to favour growth of single crystalline α-PbO. If we are to achieve highly oriented films with a single crystalline α-PbO phase further experimental analysis on various substrates such as STO, dysprosium scandate (DSO), and potassium tantalate (KTO) substrates is required. Table 4 below indicates that potassium tantalate substrates have the closes lattice match to α-PbO [91].

Table 4 shows results of experiments that compared various substrate materials used for the growth of α-PbO. Included are their lattice mismatch and FWHM of the 2θ peaks and rocking curves for films grown on each substrate under identical conditions [91]

Substrate Material	Lattice Mismatch (%)	FWHM of 2θ 002 Film Peak	FWHM of Rocking Curve	Crystallite Size (nm)
MgO	6%	No single-phase α-PbO	No single-phase α-PbO	No single-phase α-PbO
STO	1.7%	0.50°	0.65°	16.5
DSO	0.8%	0.32°	0.59°	25.5
KTO	0.3%	0.25°	0.12°	32.6

7.11 Preliminary STEM EDX analysis of PLD deposited PbO film on STO

Preliminary STEM and EDX results for PbO growth on an STO substrate by PLD is presented. Figure 7-9(a) shows an STEM image of an FIB prepared lamella of the PLD deposited film on the STO substrate. The STEM image indicates the PbO deposited film has a thickness of ~10 nm reference area 1. EDX elemental analysis of the lamella at 6 locations was performed, figure 7-9(b) shows an integrated EDX spectra of all 6 analyzed locations. A line scan figure 7-9(C) through area 1 to 3 shows the transition between the substrate and the deposited film.

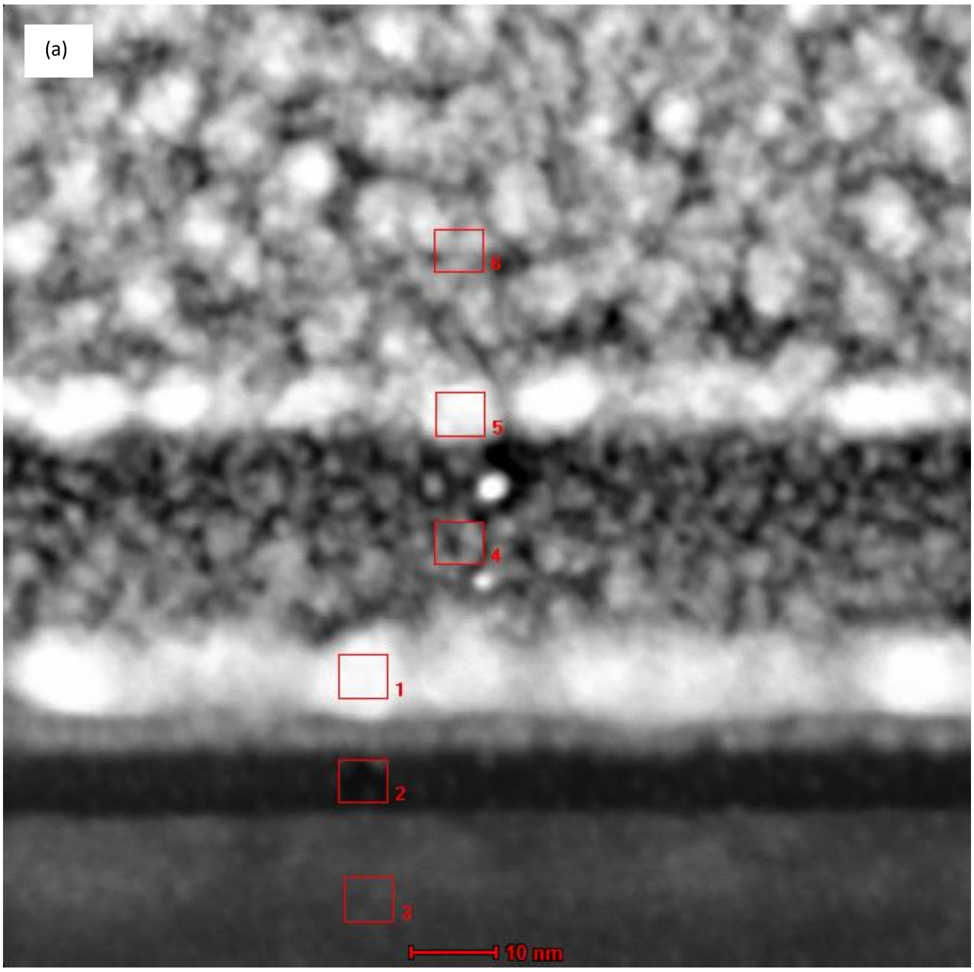

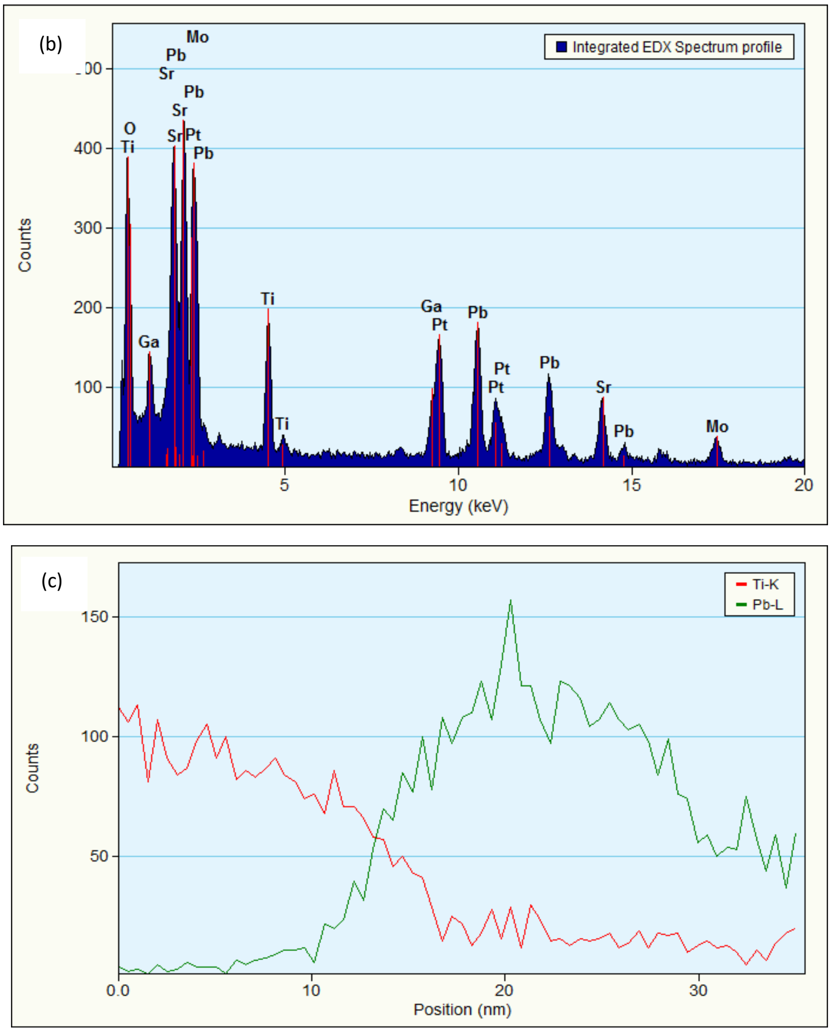

Figure 7-9 (a) STEM image PLD PbO lamella thin film, (b) integrated EDX spectrum profile of all 6 areas analyzed (c) line profile of inter face between analysed area 1 (PbO) and area 2 (substrate)

Figure 7-10(a) is an EDX spectra of area 1 which confirmed this area to be predominately the deposited PbO thin film, area 2,3 is the STO substrate and area 4,5,6 is the e-beam and ion beam platinum protection layer deposited to protect the PbO thin film during FIB sample preparation. The other identified trace elements found in the EDX spectra such as Ga is from the Gallium ion source used for FIB milling and the detected molybdenum is from the MEMS spiral heater the lamella was placed on during the analysis.

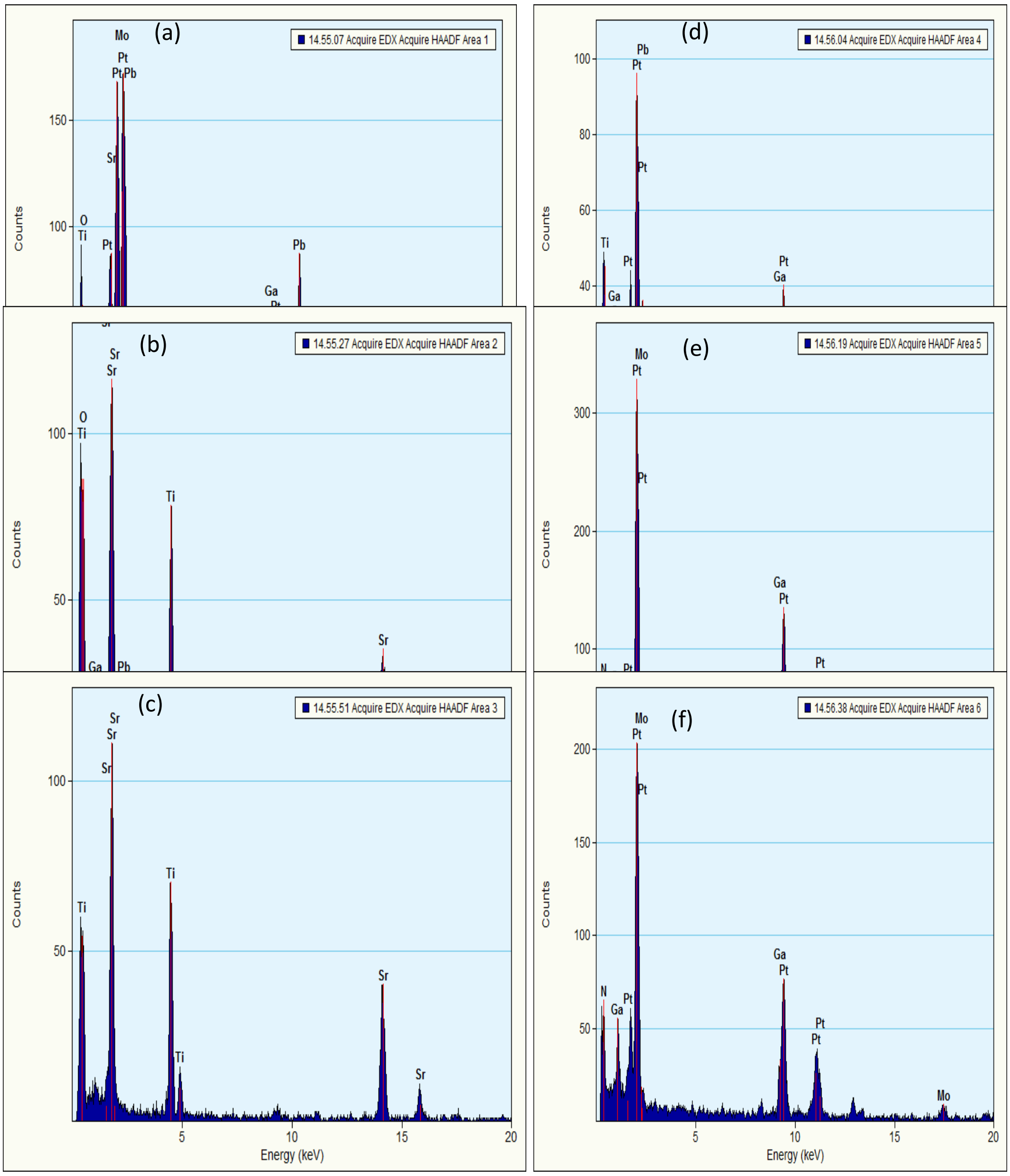

Figure 7-10 EDX spectra of the lamella areas 1-6 analyzed as outlined in figure 7-9(a)

7.12 Summary/Conclusions

The above results show that the technique is successful in number of ways:

- The transfer of a lamella from the bulk material using rotating micro-grippers and SEMGlu
- The low kV thinning of a lamella using a micro-grippers and Ro-Tip manipulator
- The capability to carry out heating experiments on lamella
- The ability to carry out EDX analysis

An alternative in-situ lift-out procedure using focused ion beam milling was developed and optimized for the preparation of lamellae for *in-situ* annealing in TEM and beyond. This technique combines for the first time the use of rotating micro-gripper for lift-out and thinning, and a unique adhesive substance, SEMGlu, during the lift-out procedure, instead of the traditional micromanipulator needle and platinum weld. Lamella were successfully mounted onto the MEMS chip for *in-situ* TEM annealing experiments without causing damage to the MEMS chip. It has been show that this novel method ensures the ability to employ wedge technique during the procedure due to the rotation of the micro-grippers. The use of the micro-grippers also ensured no platinum deposition onto the sample and reduced the risk of damaging the MEM chip during thinning HRTEM imaging of the polished lamella verifies that this method can produce high quality lamellae comparable with traditional *in-situ* lift-out procedures. The success of this technique will open a lot of avenues for many different applications of sample preparation due to its relatively low cost in comparison to other techniques and causes minimal damage. On this initial PbO lamella we were unable to observe α-PbO to β-PbO crystalline phase change after heating as observed in other experimental methods outline in chapter 5. The lamella in the region of interest (PbO) became amorphous at temperature above 430°C which was unexpected in comparison to observation in previous heating experiment using alternative sample preparation techniques. Further experimental analysis is required to fully understand the heating effect on materials such as PbO that are below 100nm in thickness.

8 Conclusion and Future Work

To incorporate nanomaterials into functional devices we need to fully understand the materials characteristics. This includes electrical, optical, mechanical and most important for us the thermal properties. The focus of my work is developing techniques to allow the *in-situ* electron microscopy characterisation of materials for the Prof Nicolosi group in CRANN. In this thesis I am presenting my work describing some new and novel techniques to characterise and synthesise 2D nanomaterials. Without the benefit of analytical tools such as TEM, FIB, SEM and advance in *in-situ* TEM holders and sample preparation techniques, the examination of these materials would prove difficult at the nanoscale.

The goal of this research was to assess the feasibility of *in-situ* TEM to examine 2D material under thermal stimuli. The emphasis has therefore been on experimental aspects and development of new and novel techniques to examine the 2D materials, namely BP and PbO. As part of this research journey we also had to discover the practicalities of how the experiments are performed, the factors that needed to be considered and the type of results that can be expected. This also included the development of many new techniques for sample preparation and the transfer of nanoscale samples to the MEMS device to enable thermal experiments *in-situ* TEM. Initially, we researched the 2D material BP and we had to overcome challenges such as material degradation and decomposition. This led us to look at analogues of BP such as PbO to enable us to examine the properties of the material in a more stable environment. Our initial goal was to prove these materials exhibited different physical, chemical properties characteristics in the bulk form as opposed to the nanoscale. Our research showed this was actually the case, however, our *in-situ* TEM also showed that the irradiation effect on the material such as knock on and radiolysis could also help us modify the material at a nanoscale. The addition of thermal stimuli using the *in-situ* TEM holder and MEMS technology further enhanced this capability.

Overall our research shows that BP has a good intrinsic thermal stability and the material is stable if isolated from water and oxygen. It may not be as stable as other 2D material, such as graphene and TMDs, in the presence of water and oxygen, however, there are already breakthroughs in developing effective passivation methods to overcome this degradation issue. It is likely that good passivation and packaging technology can already resolve this issues essential requirement for some semiconductors, such as silicon and III-V material to allow better device reliability and performance.

Although there is sporadic research activities since 2014 demonstrating BP based detectors, modulators, RF transistors and sensors research into fundamentals and applications are still in their infancy. During this research we observed further decomposition of BP when exposed to an electron beam in vacuum (Chapter 4). The degradation of 2D materials during analytical analysis in TEM must be considered prior to reporting results and parameters such as incident beam KV and beam dose should be stated on images and data obtained during analysis. By the use of MEMS technology we were successfully able to charateristise the thermal decomposition of BP in TEM. Our results show that the thermal decomposition of BP occurs at lower temperature in BP nanoflakes compared to the thermal decomposition of BP in the bulk form. The research into analogues of BP namely PbO showed that it may be easier to study the physical properties and potential phase transformation induced by thermal stimuli by selecting analogues to BP such as PbO that are more stable in air to further the research into these groups of 2D materials.

It should be also noted that new analytical methods and techniques are required to examine nanomaterials. Innovative sample preparation techniques as describe in chapter 6 and chapter 7 are require to expand the analytical capability and accuracy of results. Physical properties and characteristics of the equipment and materials used in their manufacture need to be understood and accounted for in the test environment to allow for drift during analysis from the *in-situ* holders and during thermal analysis the inherent flexural distortion on the MEMS chip characterised in this thesis chapter (3) must be accounted for during analysis. TEM is essential for the characterisation of these 2D material sets. However, without innovative thinking and consideration for factors such as the physical test environment, the effects of the inspection probe on the material, the challenges of preparing and manufacturing 2D materials, we will be unable to unlock the potential these materials offer to the scientific community. Until these physical barriers are overcome, there will remain a real barrier to investigating and commerialising these new material sets.

8.1 Future work

Scientific challenges need to be addressed in the future in the area of catalysis, electrochemistry, phase transformation and mechanical property measurement. To overcome this challenges the area I feel that needs to be addressed to continue this work are outlined below.

- **High spatial and temporal resolution combined on the same platform.**
  High spatial resolution combined with high temporal resolution is required to identify transient reaction products, understand catalytic reaction mechanisms. Currently available image acquisition systems allow us to routinely acquire high-resolution (<0.1 nm) images with low temporal resolution (0.033 s to 0.2 s range) or low resolution (a few nanometer in single shot mode) with high temporal resolution.
- **Automatic drift correction**
  Drift is major issue for all *in-situ* experiments, especially during heating. Although new MEMS based heating holders have minimal drift (<1 nm min^{-1}, at best), it is still enough to make continuous acquisition of high resolution images during heating difficult. Both hardware and software developments are needed. The correct selection of the raw material by vendors in the manufacturing of *in-situ* holder is critical to reduce drift during experiments over extended periods.
- **Temperature measurement at the microscale**
  Temperature measurement continues to be one of the challenging problems that has kept us from obtaining thermodynamic and kinetic information. The actual temperature of the sample under TEM observation. The ambiguity for furnace heaters with thermocouples arises from the nature of thermal contact between TEM grid and furnace, and the thermal conductivity of grid material and sample. For ETEM experiments the problem becomes more severe as temperature gradients are also dependent on gas composition and

pressure. However MEMS technology and accurate 4 point electrical probing with integrated temperature feedback loops migrate this issue to some extent.

- **Simultaneous acquisition of bright field , dark field and select area diffraction patterns**
  Combining diffraction and imaging information would be a valuable tool for many applications such as catalytic particles. At present, parallel detection of both signals is not possible and requires a different TEM design. Modification of current instrumentation will allow switching between diffraction and imaging mode with sufficient speed. This can be done with software but requires two detectors.
- **Combinational *in-situ* holders**
  To enable measurement the mechanical properties of crystals (double tilt) as a function of temperature (heating), biasing (electrical and magnetic).
- **Concurrent microscopy and spectroscopy (lab in the pole-piece gap)**
  In situ observations of the effects of external stimuli on the morphology, structure, chemistry have enabled us to elucidate a number of atomic scale reaction mechanisms. However, the information obtained is limited to the nanoscale, and in order to relate the local behavior (in the electron beam) to the average behavior of the sample, simultaneous acquisition of complementary integrated measurements is needed.
- **Development of robust fluid cell holders and gas holders compatible with high vacuum environment**
  A number of vendor such as DENS solutions , Proto-chips and Humming bird provide gas holders solutions however these are very much still under development.
- **High speed data acquisition and processing**
  The amount of data acquired simultaneously during *in-situ* experiments is increasing with the complexity of the experiments and the increasing available methods of data collection during experiments.

Bibliography

[1] R. Venkatraman, J. C. Bravman, W. D. Nix, P. W. D. Avies, P. A. Flinn, and D. B. Fraser, "Mechanical properties and microstructural characterization of Al-0.5%Cu thin films," *J. Electron. Mater.*, vol. 19, no. 11, pp. 1231–1237, Nov. 1990.

[2] Z. Liu, L. Ma, G. Shi, W. Zhou, Y. Gong, S. Lei, X. Yang, J. Zhang, J. Yu, K. P. Hackenberg, A. Babakhani, J.-C. Idrobo, R. Vajtai, J. Lou, and P. M. Ajayan, "In-plane heterostructures of graphene and hexagonal boron nitride with controlled domain sizes," *Nat. Nanotechnol.*, vol. 8, no. 2, pp. 119–124, 2013.

[3] H. P. Longworth and C. V. Thompson, "Abnormal grain growth in aluminum alloy thin films," *J. Appl. Phys.*, vol. 69, no. 7, pp. 3929–3940, Apr. 1991.

[4] F. Radulescu, J. M. Mccarthy, and E. A. Stach, "In-Situ Annealing Transmission Electron Microscopy Study of Pd/Ge/Pd/GaAs Interfacial Reactions," *MRS Proc.*, vol. 589, p. 179, Jan. 1999.

[5] M. Legros, G. Dehm, R. M. Keller-Flaig, E. Arzt, K. J. Hemker, and S. Suresh, "Dynamic observation of Al thin films plastically strained in a TEM," *Mater. Sci. Eng. A309–*, vol. 310, pp. 463–467, 2001.

[6] J. Yao, X. Shen, B. Wang, H. Liu, and G. Wang, "In situ chemical synthesis of SnO2–graphene nanocomposite as anode materials for lithium-ion batteries," *Electrochem. commun.*, vol. 11, no. 10, pp. 1849–1852, Oct. 2009.

[7] N. P. Young, M. A. van Huis, H. W. Zandbergen, H. Xu, and A. I. Kirkland, "Transformations of gold nanoparticles investigated using variable temperature high-resolution transmission electron microscopy," *Ultramicroscopy*, vol. 110, no. 5, pp. 506–516, 2010.

[8] J. Damiano, D. P. Nackashi, and S. E. Mick, "A MEMS-based Technology Platform for in-situ TEM Heating Studies," 2017.

[9] A. K. Geim and K. S. Novoselov, "The rise of graphene.," *Nat. Mater.*, vol. 6, no. 3, pp. 183–191, 2007.

[10] W. J. Yu, Q. A. Vu, H. Oh, H. G. Nam, H. Zhou, S. Cha, A. Carvalho, M. Jeong, H. Choi, A. H. C. Neto, Y. H. Lee, and X. Duan, "Unusually efficient photocurrent extraction by tunnelling through discretized barriers," *Nat. Publ. Gr.*, vol. 7, pp. 1–9, 2016.

[11] "Expanding our 2D vision," vol. 1, no. November, p. 2016, 2016.

[12] Y. Cai, G. Zhang, and Y. Zhang, "Layer-dependent Band Alignment and," pp. 1–6, 2014.

[13] Z. Zhang, A. J. Mannix, Z. Hu, B. Kiraly, N. P. Guisinger, M. C. Hersam, and B. I. Yakobson, "Substrate-Induced Nanoscale Undulations of Borophene on Silver," 2016.

[14] S. Z. Butler, S. M. Hollen, L. Cao, Y. Cui, J. A. Gupta, H. R. Gutie, T. F. Heinz, S. S. Hong, J. Huang, A. F. Ismach, E. Johnston-halperin, M. Kuno, V. V Plashnitsa, R. D. Robinson, R. S. Ruoff, S. Salahuddin, J. Shan, L. Shi, O. M. G. Spencer, M. Terrones, W. Windl, and J. E. Goldberger, "Opportunities in Two-Dimensional Materials Beyond Graphene," no. 4, pp. 2898–2926, 2013.

[15] P. De Padova, P. Perfetti, B. Olivieri, P. De Padova, J. Avila, A. Resta, and H. Enriquez, "Silicene structures on silver surfaces," no. 111.

[16] E. Bianco, S. Butler, S. Jiang, O. D. Restrepo, W. Windl, and J. E. Goldberger, "Stability and Exfoliation of Germanane : A Germanium Graphane Analogue," no. 5, pp. 4414–4421, 2013.

[17] H. S. S. Ramakrishna Matte, A. Gomathi, A. K. Manna, D. J. Late, R. Datta, S. K. Pati, and C. N. R. Rao, "MoS2 and WS2 analogues of graphene," *Angew. Chemie - Int. Ed.*, vol. 49, no. 24, pp. 4059–4062, 2010.

[18] M. Choucair, P. Thordarson, and J. A. Stride, “Gram-scale production of graphene based on solvothermal synthesis and sonication,” vol. 4, no. December 2008, pp. 7–10, 2009.

[19] Y. Cui, L. J. Lauhon, M. S. Gudiksen, J. Wang, C. M. Lieber, Y. Cui, L. J. Lauhon, M. S. Gudiksen, and J. Wang, “Diameter-controlled synthesis of single-crystal silicon nanowires Diameter-controlled synthesis of single-crystal silicon nanowires,” vol. 2214, no. 2001, pp. 1–4, 2016.

[20] C. Singh, M. S. P. Shaffer, and A. H. Windle, “Production of controlled architectures of aligned carbon nanotubes by an injection chemical vapour deposition method,” *Carbon N. Y.*, vol. 41, no. 2, pp. 359–368, 2003.

[21] X. Li, W. Cai, J. An, S. Kim, J. Nah, D. Yang, L. Colombo, and R. S. Ruoff, “Large-Area Synthesis of High-Quality and Uniform Graphene Films on Copper Foils,” vol. 3893, no. June, pp. 1312–1315, 2009.

[22] D. Kong, W. Dang, J. J. Cha, H. Li, S. Meister, H. Peng, Z. Liu, and Y. Cui, “with Highly Tunable Chemical Potential,” no. C, pp. 2245–2250, 2010.

[23] C. Li, L. Huang, G. P. Snigdha, Y. Yu, and L. Cao, “Role of Boundary Layer Di ff usion in Vapor Deposition Growth of Chalcogenide Nanosheets : The Case of GeS,” no. 10, pp. 8868–8877, 2012.

[24] X. Li, W. Cai, J. An, S. Kim, J. Nah, and D. Yang, “PUBLISHED ON-LINE BY SCIENCE ON MAY 7 , 2009 (Science Express article). This is the official publication date for this work . Large-Area Synthesis of High-Quality and Uniform Graphene Films on Copper Foils,” vol. 2009, pp. 1–12, 2009.

[25] K. S. Novoselov, J. M. Raimond, M. Brune, Q. Computation, F. De Martini, C. Monroe, D. L. Moehring, P. L. Knight, M. B. Plenio, V. Vedral, E. S. Polzik, C. Variables, S. L. Braunstein, A. K. Pati, M. D. Lukin, I. J. Cirac, P. Zoller, C. Han, P. Xue, G. C. Guo, S. V Polyakov, A. Kuzmich, H. J. Kimble, J. I. Cirac, T. A. B. Kennedy, P. Horodecki, R. Horodecki, D. P. Divincenzo, J. A. Smolin, A. Beige, L. C. Kwek, P. Kok, J. A. Sauer, L. You, A. Zangwill, M. S. Chapman, M. Nielsen, A. K. Geim, S. V. Morozov, D. Jiang, Y. Zhang, S. V. Dubonos, I. V. Grigorieva, and A. A. Firsov, “Electric field effect in atomically thin carbon films,” *Science (80-.).*, vol. 306, no. 5696, pp. 666–669, 2004.

[26] J. Kim, L. J. Cote, F. Kim, and J. Huang, “Visualizing Graphene Based Sheets by Fluorescence Quenching Microscopy,” no. 14, pp. 8499–8506, 2010.

[27] G. Binnig and C. F. Quate, “Atomic Force Microscope,” *Phys. Rev. Lett.*, vol. 56, no. 9, pp. 930–933, 1986.

[28] Z. E. Al I, Peter Nemes Osvath, “Anomalies in thickness measurements of graphene and FLG crystals by tapping mode AFM,” *Carbon N. Y.*, vol. 46, no. 11, pp. 1435–42, 2008.

[29] K. S. Joya and X. Sala, “In situ Raman and surface-enhanced Raman spectroscopy on working electrodes : spectroelectrochemical characterization of water oxidation electrocatalysts,” *Phys. Chem. Chem. Phys.*, vol. 17, no. 1, pp. 21094–21103, 2015.

[30] J. Ping and M. S. Fuhrer, “Layer Number and Stacking Sequence Imaging of Few-Layer Graphene by Transmission Electron Microscopy,” 2012.

[31] O. L. Krivanek, M. F. Chisholm, V. Nicolosi, T. J. Pennycook, G. J. Corbin, N. Dellby, M. F. Murfitt, C. S. Own, Z. S. Szilagyi, M. P. Oxley, S. T. Pantelides, and S. J. Pennycook, “Atom-by-atom structural and chemical analysis by annular dark-field electron microscopy,” *Nature*, vol. 464, no. 7288, pp. 571–574, 2010.

[32] O. L. Krivanek, N. Dellby, M. F. Murfitt, M. F. Chisholm, T. J. Pennycook, K. Suenaga, and V. Nicolosi, “Ultramicroscopy Gentle STEM : ADF imaging and EELS at low primary energies $,” *Ultramicroscopy*, vol. 110, no. 8, pp. 935–945, 2010.

[33] I. Khan, K. Saeed, and I. Khan, “Nanoparticles: Properties, applications and toxicities,” *Arab. J. Chem.*, 2017.

[34] R. Phatthanakun, P. Deekla, W. Pummara, C. Sriphung, C. Pantong, and N. Chomnawang, “Design and fabrication of thin-film aluminum microheater and nickel temperature sensor,” *2012 7th IEEE Int. Conf. Nano/Micro Eng. Mol. Syst. NEMS 2012*, no. 2, pp. 112–115, 2012.

[35] S. Pan and I. A. Aksay, “Factors Controlling the Size of Graphene Oxide Sheets Produced via the Graphite Oxide Route,” no. 5, pp. 4073–4083, 2011.

[36] R. Sinclair, “In situ high-resolution transmission electron microscopy of material reactions,” pp. 1065–1072, 2017.

[37] M. L. Taheri, E. A. Stach, I. Arslan, P. A. Crozier, and B. C. Kabius, “Current status and future directions for in situ transmission electron microscopy,” vol. 134, no. Bâtiment MXC, pp. 1–23.

[38] “insitu TEM citation web of science.” [Online]. Available: https://apps.webofknowledge.com/CitationReport.do?action=home&product=WOS&search_mode=CitationReport&cr_pqid=5&qid=5&SID=N1M8VXKhRMoeg7iwGAG. [Accessed: 06-Jul-2017].

[39] H. Saka, T. Kamino, and S. Arai, “I n Situ Heating Electron Microscopy,” vol. 33, no. February 2008, pp. 93–100, 2017.

[40] D. C. Bell and N. Erdman, *Low Voltage Electron Microscopy: Principles and Applications*. 2013.

[41] D. B. Williams and C. B. Carter, *Transmission Electron Microscopy*, vol. 13, no. 3. 1996.

[42] V. Nicolosi, “Introduction to Transmission Electron Microscopy Course Notes,” 2013.

[43] R. Brydson, “Electron Energy Loss Spectroscopy,” *Epic. Microsc. Soc. Microsc. HANDBOOKS Vol. 48, BIOS Sci. Publ. Ltd, Oxford, UK*, 2001.

[44] R. F. Egerton, “Control of radiation damage in the TEM,” *Ultramicroscopy*, vol. 127, pp. 100–108, 2013.

[45] M. Terauchi and M. Tanaka, “High-resolution EELS study of carbon and boron allotropes,” *J. Surf. Anal.*, 1997.

[46] D. B. Williams and C. B. Carter, *Transmission Electron Microscopy: A Textbook for Materials Science*, vol. 1–4. 2009.

[47] B. E. I. Peng, M. Locascio, P. Zapol, S. Li, S. L. Mielke, G. C. Schatz, and H. D. Espinosa, “Measurements of near-ultimate strength for multiwalled carbon nanotubes and irradiation-induced crosslinking improvements,” vol. 3, no. October, 2008.

[48] P. J. D. E. Pablo, B. Biel, A. Rubio, and F. Flores, “carbon nanotubes by ion irradiation in the,” vol. 4, no. July, 2005.

[49] O. V Yazyev and L. Helm, “Defect-induced magnetism in graphene,” no. January, pp. 1–5, 2007.

[50] F. J. Garc, “Optical excitations in electron microscopy,” *Spectroscopy*, 2007.

[51] A. V. Krasheninnikov and K. Nordlund, “Ion and electron irradiation-induced effects in nanostructured materials,” *J. Appl. Phys.*, vol. 107, no. 7, 2010.

[52] A. Manuscript and A. T. E. Microscope, “NIH Public Access,” vol. 16, no. 4, pp. 386–392, 2011.

[53] R. F. Egerton, P. Li, and M. Malac, “Radiation damage in the TEM and SEM.,” *Micron*, vol. 35, no. 6, pp. 399–409, Jan. 2004.

[54] L. Hobbs, “Radiation effects in analysis by TEM,” *Introd. to Anal. electron Microsc.*, 1987.

[55] S. P. Venkateshan, *Mechanical Measurements*, vol. 23. John Wiley & Sons, 2015.

[56] M. S. Van Dusen, “Platinum-Resistance Thermometry At Low Temperatures 1,” *J. Am. Chem. Soc.*, vol. 47, no. 2, pp. 326–332, 1925.

[57] H. Preston-Thomas, “The International Temperature Scale of 1990(ITS-90),” *Metrologia*, vol. 27, no. 1, pp. 3–10, 1990.

[58] “www.itsirl.com/admin/pdfmanual/1399021951CalVan.pdf - Google Search.” [Online]. Available: https://www.google.ie/#q=www.itsirl.com%2Fadmin%2Fpdfmanual%2F1399021951CalVan.pdf. [Accessed: 08-Jul-2016].

[59] ITS, “The Callendar – van Dusen coefficients,” pp. 3–5, 1999.

[60] L. Mele, T. Rossi, M. Riccio, E. Iervolino, F. Santagata, A. Irace, G. Breglio, J. F. Creemer, and P. M. Sarro, “Electro-thermal analysis of MEMS microhotplates for the optimization of temperature uniformity,” *Procedia Eng.*, vol. 25, pp. 387–390, 2011.

[61] G. W. Watson and S. C. Parker, “Origin of the Lone Pair of r -PbO from Density Functional Theory Calculations,” pp. 1258–1262, 1999.

[62] P. Canepa, P. Ugliengo, and M. Alfredsson, “Elastic and vibrational properties of alpha and beta-PbO,” *J. Phys. Chem. C*, no. 1, p. 8, 2012.

[63] K. S. Novoselov, V. I. Fal’ko, L. Colombo, P. R. Gellert, M. G. Schwab, and K. Kim, “A roadmap for graphene,” *Nature*, vol. 490, no. 7419, pp. 192–200, 2012.

[64] A. Nag, K. Raidongia, K. P. S. S. Hembram, R. Datta, U. V. Waghmare, and C. N. R. Rao, “Graphene analogues of BN: Novel synthesis and properties,” *ACS Nano*, vol. 4, no. 3, pp. 1539–1544, 2010.

[65] M. B. Sreedhara, H. S. S. R. Matte, A. Govindaraj, and C. N. R. Rao, “Synthesis, characterization, and properties of few-layer moO3,” *Chem. - An Asian J.*, vol. 8, no. 10, pp. 2430–2435, 2013.

[66] F. Wu, Y. Liu, G. Yu, D. Shen, Y. Wang, and E. Kan, “Visible-Light-Absorption in Graphitic C 3 N 4 Bilayer: Enhanced by Interlayer Coupling,” *J. Phys. Chem. Lett.*, vol. 3, pp. 3330–3334, 2012.

[67] C. R. Ryder, J. D. Wood, S. A. Wells, and M. C. Hersam, “Chemically Tailoring Semiconducting Two-Dimensional Transition Metal Dichalcogenides and Black Phosphorus,” *ACS Nano*, p. acsnano.6b01091, 2016.

[68] D. D. Vaughn, R. J. Patel, M. A. Hickner, and R. E. Schaak, “Single-crystal colloidal nanosheets of GeS and GeSe,” *J. Am. Chem. Soc.*, vol. 132, no. 43, pp. 15170–15172, 2010.

[69] X. Ling, H. Wang, S. Huang, F. Xia, and M. S. Dresselhaus, “The renaissance of black phosphorus,” vol. 112, no. 15, pp. 4523–4530, 2015.

[70] H. Du, X. Lin, Z. Xu, and D. Chu, “Recent developments in black phosphorus transistors,” *J. Mater. Chem. C*, vol. 3, pp. 8760–8775, 2015.

[71] E. Passaglia, F. Cicogna, G. Lorenzetti, S. Legnaioli, and M. Caporali, “Novel polystyrene-based nanocomposites by phosphorene dispersion,” pp. 2–6.

[72] D. Hanlon, C. Backes, E. Doherty, C. S. Cucinotta, N. C. Berner, C. Boland, K. Lee, A. Harvey, P. Lynch, Z. Gholamvand, S. Zhang, K. Wang, G. Moynihan, A. Pokle, Q. M. Ramasse, N. McEvoy, W. J. Blau, J. Wang, G. Abellan, F. Hauke, A. Hirsch, S. Sanvito, D. D. O’Regan, G. S. Duesberg, V. Nicolosi, and J. N. Coleman, “Liquid exfoliation of solvent-stabilized few-layer black phosphorus for applications beyond electronics,” *Nat.*

Commun., vol. 6, p. 8563, 2015.

[73] A. Castellanos-Gomez, L. Vicarelli, E. Prada, J. O. Island, K. L. Narasimha-Acharya, S. I. Blanter, D. J. Groenendijk, M. Buscema, G. A. Steele, J. V Alvarez, H. W. Zandbergen, J. J. Palacios, and H. S. J. van der Zant, “Isolation and characterization of few-layer black phosphorus,” *2D Mater.*, vol. 1, no. 2, p. 025001, Jun. 2014.

[74] A. Facchetti and T. J. Marks, “Transparent Electronics,” no. March 2006, p. 2008, 2010.

[75] L. Shi, Y. Xu, and Q. Li, “Controlled growth of lead oxide nanosheets, scrolled nanotubes, and nanorods,” *Cryst. Growth Des.*, vol. 8, no. 10, pp. 3521–3525, 2008.

[76] H. Zhang and J. Ouyang, “High-performance inverted polymer solar cells with lead monoxide-modified indium tin oxides as the cathode,” *Org. Electron. physics, Mater. Appl.*, vol. 12, no. 11, pp. 1864–1871, 2011.

[77] M. Martos, J. Morales, L. Sa, R. Ayouchi, D. Leinen, F. Martin, and J. R. R. Barrado, “Electrochemical properties of lead oxide films obtained by spray pyrolysis as negative electrodes for lithium secondary batteries,” vol. 46, pp. 2939–2948, 2001.

[78] C. Article, “CrystEngComm,” vol. 15, no. 18, 2013.

[79] Y. Wang, X. Lin, H. Zhang, T. Wen, F. Huang, G. Li, Y. Wang, F. Liao, and J. Lin, “Selected-control hydrothermal growths of alpha- and beta-PbO crystals and orientated pressure-induced phase transition,” *Crystengcomm*, vol. 15, no. 18, pp. 3513–3516, 2013.

[80] C. Shan, Z. Sofer, O. Jankovský, H. Wang, and M. Pumera, “Electrochemical Properties of Layered SnO and PbO for Energy Applications,” no. January 2012, pp. 2012–2013, 2015.

[81] D. Voiry, A. Mohite, and M. Chhowalla, “Phase engineering of transition metal dichalcogenides.,” *Chem. Soc. Rev.*, vol. 44, no. 9, pp. 2702–12, 2015.

[82] R. Gusmão, Z. Sofer, and M. Pumera, “Black Phosphorus Rediscovered: From Bulk Material to Monolayers,” *Angew. Chemie - Int. Ed.*, vol. 56, no. 28, pp. 8052–8072, 2017.

[83] K. K. Amara, Y. Chen, Y. C. Lin, R. Kumar, E. Okunishi, K. Suenaga, S. Y. Quek, and G. Eda, “Dynamic Structural Evolution of Metal-Metal Bonding Network in Monolayer WS2,” *Chem. Mater.*, vol. 28, no. 7, pp. 2308–2314, 2016.

[84] S. A. Elawam, W. M. Morsi, H. M. Abou-shady, and O. W. Guirguis, “Characterizations of Beta-lead Oxide ‘ Massicot ,’” vol. 17, no. 1, pp. 1–10, 2016.

[85] S. Jesse, Q. He, A. R. Lupini, D. N. Leonard, M. P. Oxley, O. Ovchinnikov, R. R. Unocic, A. Tselev, M. Fuentes-cabrera, B. G. Sumpter, S. J. Pennycook, S. V Kalinin, and A. Y. Borisevich, “Atomic-Level Sculpting of Crystalline Oxides : Toward Bulk Nanofabrication with Single Atomic Plane Precision,” pp. 5895–5900, 2015.

[86] R. M. Langford and a. K. Petford-Long, “Preparation of transmission electron microscopy cross-section specimens using focused ion beam milling,” *J. Vac. Sci. Technol. A Vacuum, Surfaces, Film.*, vol. 19, no. September 2000, p. 2186, 2001.

[87] R. M. Langford and C. Clinton, “In situ lift-out using a FIB-SEM system,” *Micron*, vol. 35, pp. 607–611, 2004.

[88] M. Duchamp, Q. Xu, and R. E. Dunin-Borkowski, “Convenient Preparation of High-Quality Specimens for Annealing Experiments in the Transmission Electron Microscope,” *Microsc. Microanal.*, vol. 20, no. 06, pp. 1638–1645, 2014.

[89] M. Canavan, D. Daly, A. Rummel, E. K. McCarthy, C. McAuley, and V. Nicolosi, “Novel in-situ lamella

fabrication technique for in-situ TEM," *Ultramicroscopy*, vol. 190, pp. 21–29, 2018.

[90] M. Schaffer, B. Schaffer, and Q. Ramasse, "Sample preparation for atomic-resolution STEM at low voltages by FIB," *Ultramicroscopy*, vol. 114, pp. 62–71, 2012.

[91] U. C. Berkeley and E. Leigh, "Electronic Thesis and Dissertations Growth and Characterization of α -PbO for Room Temperature Radiation Detection By Erin Leigh Ford A dissertation submitted in partial satisfaction of the requirements for the degree of Doctor of Philosophy in Engineering," 2014.

9 Appendix 1

S1. Crystalline BP to amorphous BP.

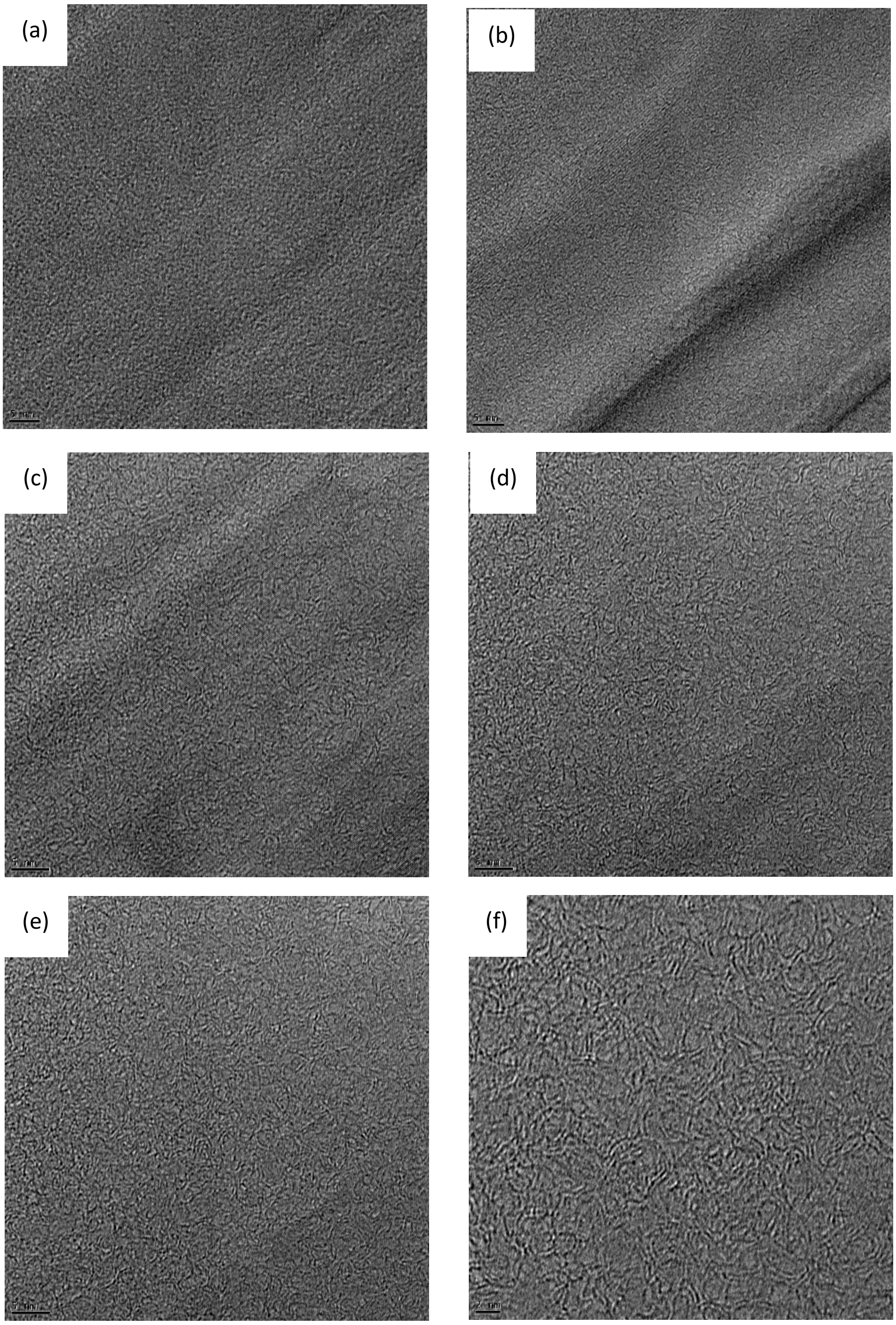

Figure S-1 (a) 300kV high resolution TEM series of a BP single flake heated to 425°C and exposed to beam over 10min time period. The BP flake over time (10 mins) being heated and exposed to the beam transforms from Crystalline BP to amorphous BP.

S2. Irradiation of BP sample with electron beam.

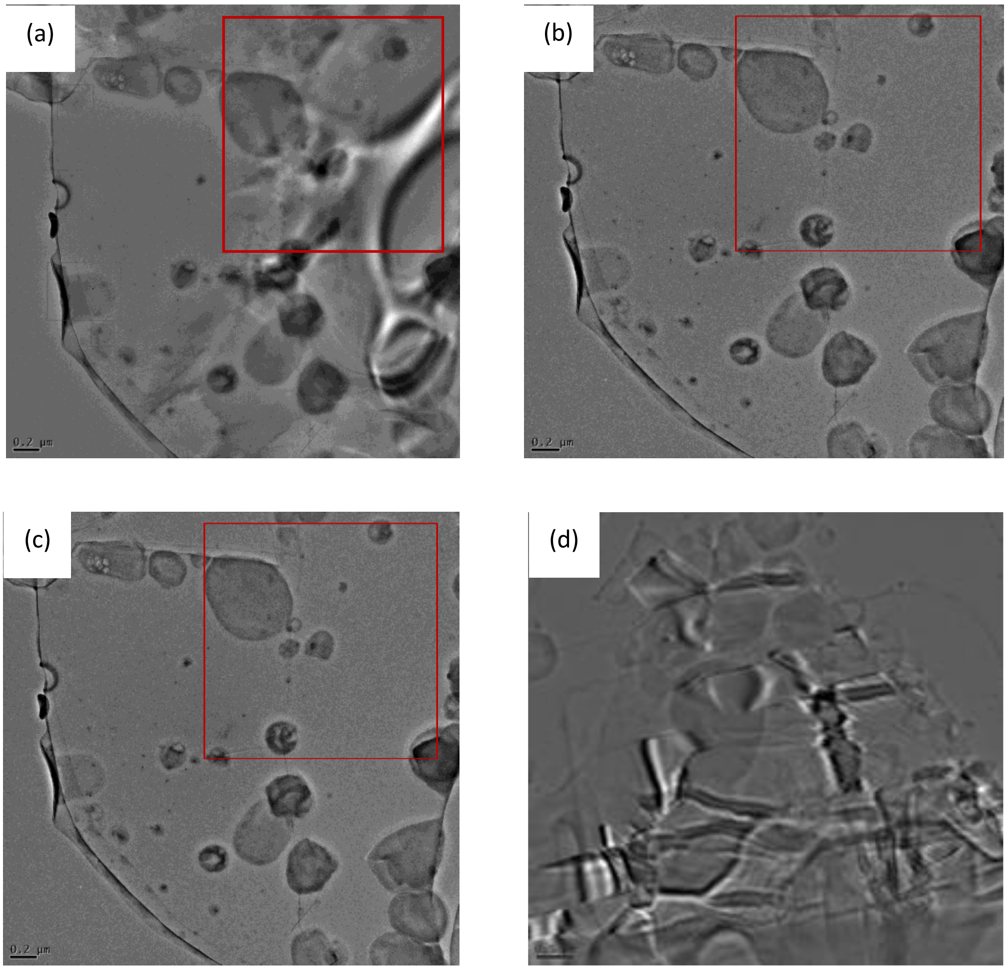

Figure S-2 (a) 300kV high resolution TEM image of a thick area of a BP flake irradiated by the beam in the select area indicated by red inset box while heating continuously at 450°C. (b) Shows the changes to the BP flake as it starts to show signs of change from a crystalline material to amorphous material over time. (C) Shows the same flake completely amorphous over time due to beam irradiation and heating, (d) 300kV high resolution TEM image of a new BP flake heated to 550°C not exposed to beam however completely amorphous.

S3. Fast Fourier transform analysis of HRTEM images

The fast Fourier transform (FFT) of HRTEM images have been analyzed for $PbCO_3$. The flakes were oriented to a particular zone axis where lattice spacing corresponding to 4.4 Å and 2.5 Å have been observed. The $PbCO_3$ flakes are found to be stable till at least 250 °C both in the *beam-off* and *beam-on* conditions. But we have observed slight expansion in the *d-spacing* with temperature after 250 °C. This is demonstrated in the figure S4. This observation lead us to do fast ramp rate till 250 °C and slower rate after 250 °C for the heating scheme for the *beam-on* condition.

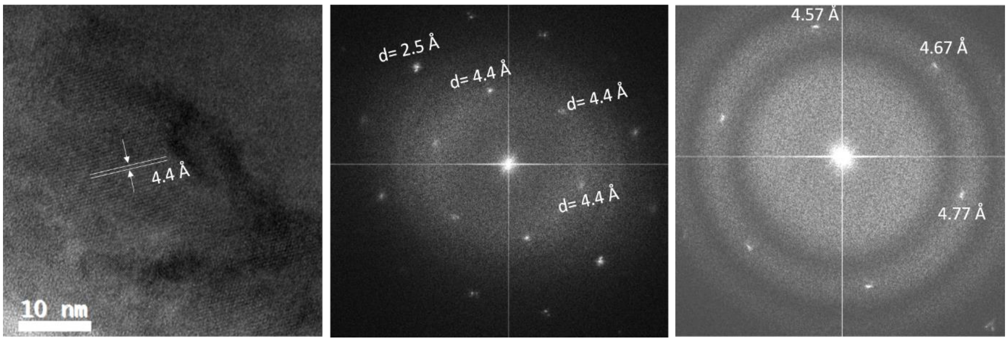

Figure S3: (a) The HRTEM image of $PbCO_3$ at room temperature, (b) The FFT of $PbCO_3$ HRTEM image at room temperature (c) The FFT of HRTEM image of $PbCO_3$ at 275 °C.

S4. Powder X-Ray diffraction

The powder x-ray diffraction pattern of $PbCO_3$ is given in figure S3.

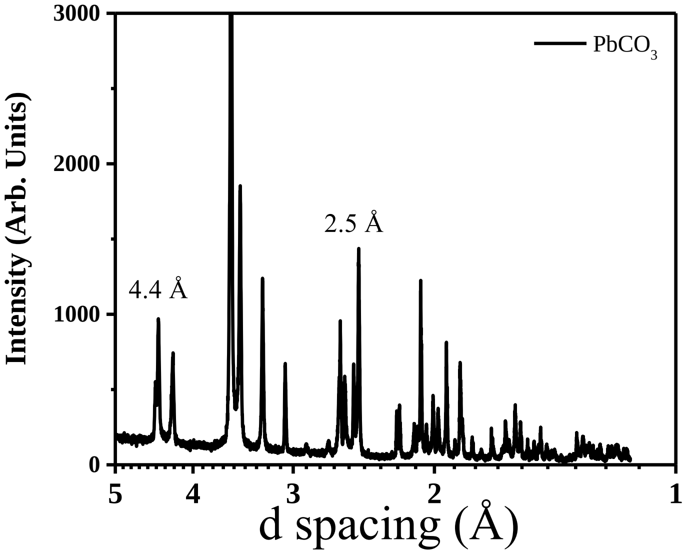

Figure S4: The powder x-ray diffraction pattern of $PbCO_3$

S5. Powder X-Ray diffraction for α-phase PbO

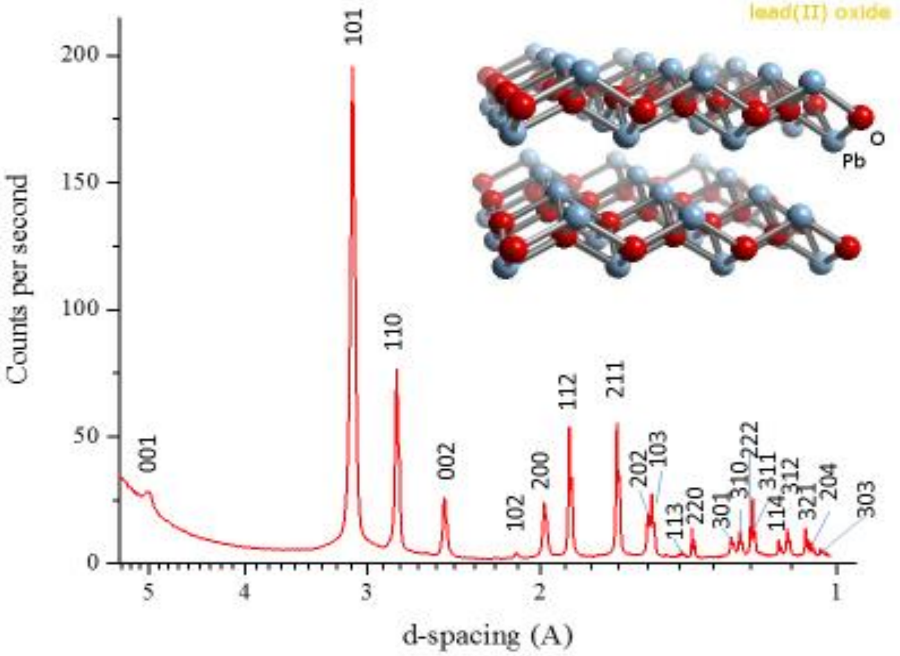

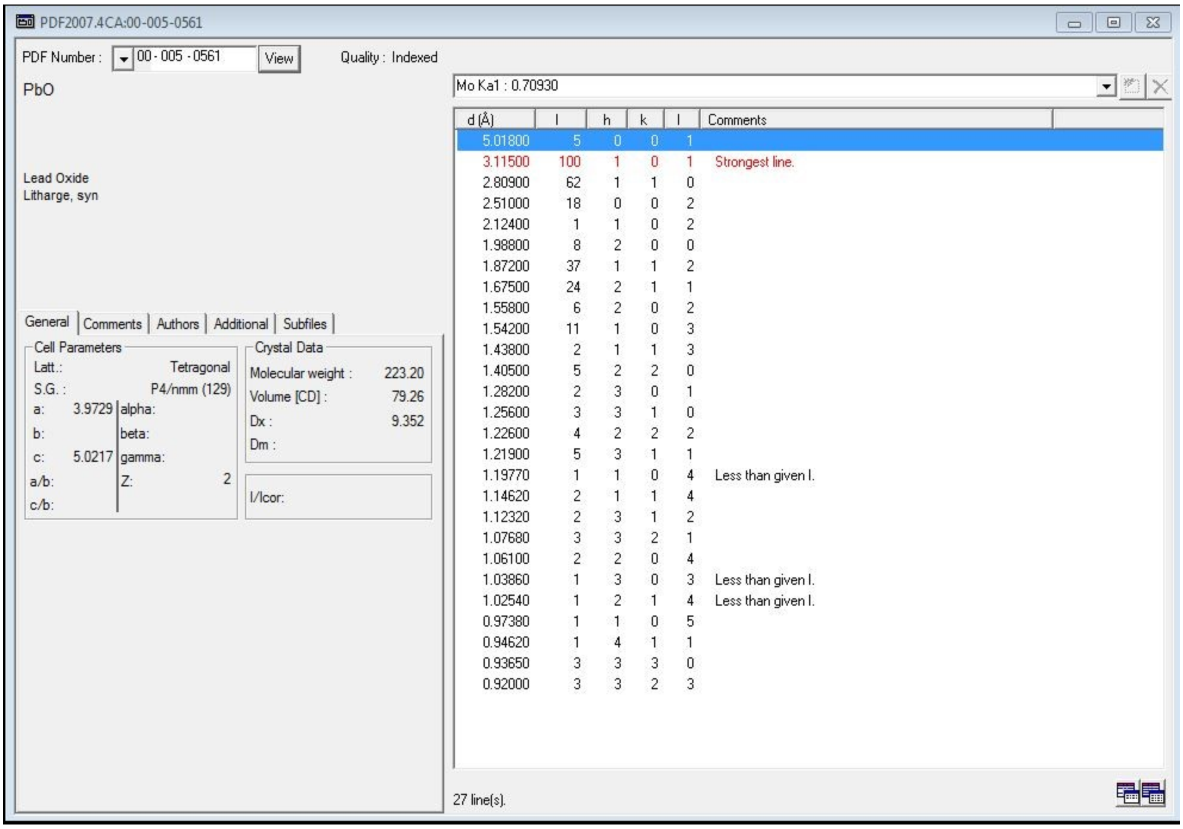

PDF Number : 00 - 005 - 0561

Quality : Indexed

PbO

Lead Oxide
Litharge, syn

Cell Parameters
Latt.: Tetragonal
S.G. : P4/nmm (129)
a: 3.9729
alpha:
b:
beta:
c: 5.0217
gamma:
a/b:
Z: 2
c/b:

Crystal Data
Molecular weight : 223.20
Volume [CD] : 79.26
Dx : 9.352
Dm :

I/Icor:

Mo Ka1 : 0.70930

d (Å)	I	h	k	l	Comments
5.01800	5	0	0	1	
3.11500	100	1	0	1	Strongest line.
2.80900	62	1	1	0	
2.51000	18	0	0	2	
2.12400	1	1	0	2	
1.98800	8	2	0	0	
1.87200	37	1	1	2	
1.67500	24	2	1	1	
1.55800	6	2	0	2	
1.54200	11	1	0	3	
1.43800	2	1	1	3	
1.40500	5	2	2	0	
1.28200	2	3	0	1	
1.25600	3	3	1	0	
1.22600	4	2	2	2	
1.21900	5	3	1	1	
1.19770	1	1	0	4	Less than given I.
1.14620	2	1	1	4	
1.12320	2	3	1	2	
1.07680	3	3	2	1	
1.06100	2	2	0	4	
1.03860	1	3	0	3	Less than given I.
1.02540	1	2	1	4	Less than given I.
0.97380	1	1	0	5	
0.94620	1	4	1	1	
0.93650	3	3	3	0	
0.92000	3	3	2	3	

27 line(s).

Figure S5: The powder x-ray diffraction pattern of α- phase Tetragonal and corresponding XRD analysis results.

S6. Powder X-Ray diffraction for β-phase PbO

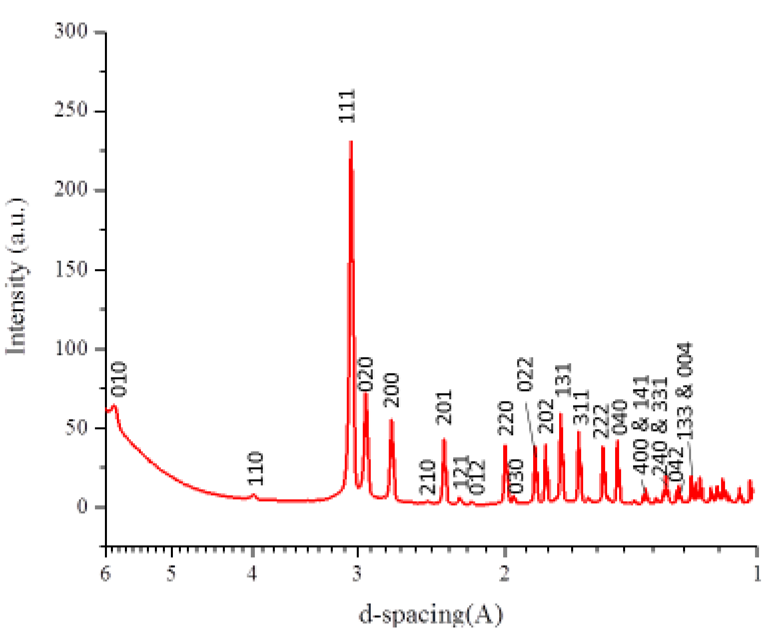

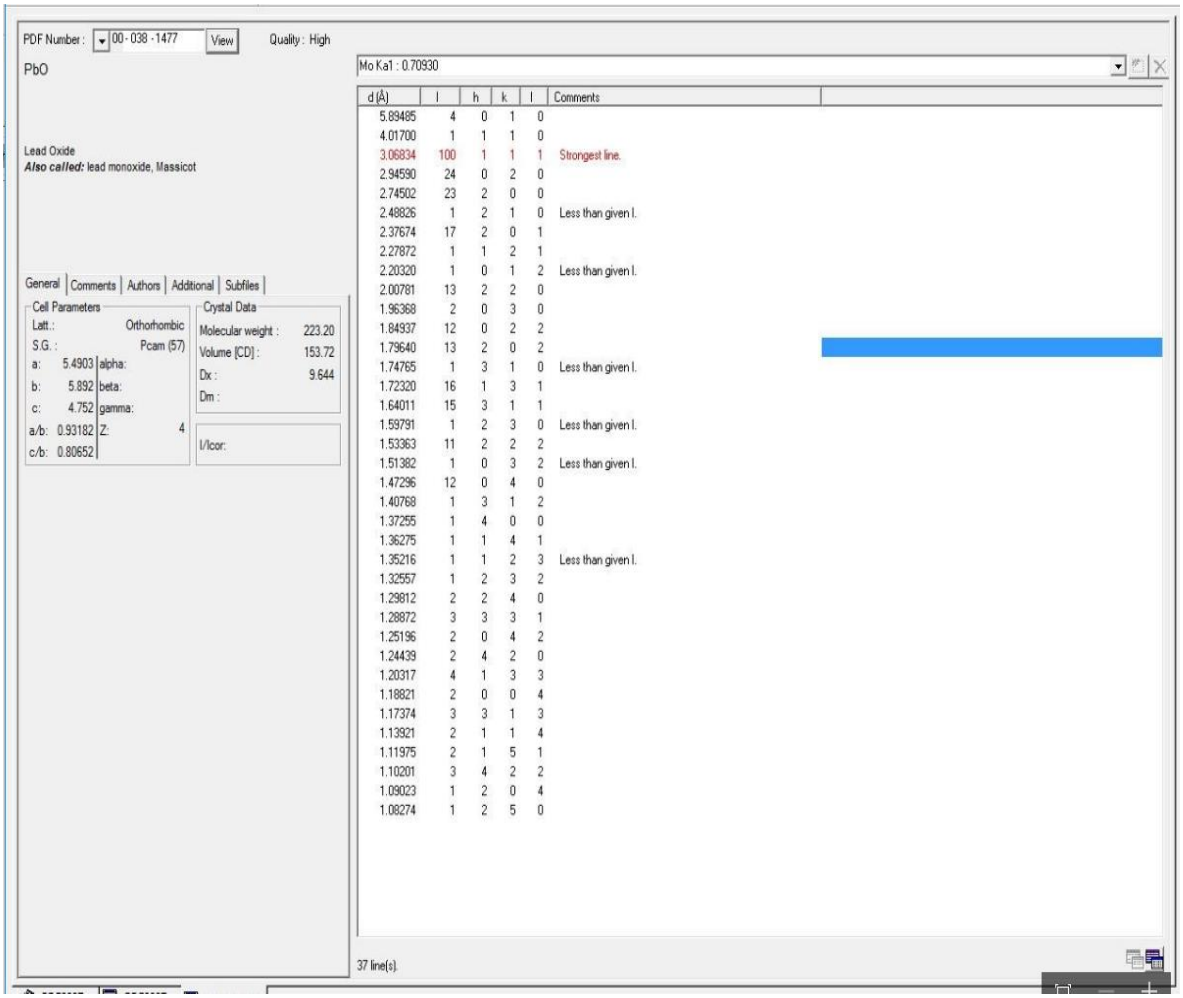

PDF Number : 00 - 038 - 1477

Quality : High

PbO

Lead Oxide

Also called: lead monoxide, Massicot

Cell Parameters

Latt.: Orthorhombic

S.G. : Pcam (57)

a: 5.4903

b: 5.892

c: 4.752

a/b: 0.93182

c/b: 0.80652

alpha:

beta:

gamma:

Z: 4

Crystal Data

Molecular weight : 223.20

Volume [CD] : 153.72

Dx : 9.644

Dm :

I/Icor:

Mo Ka1 : 0.70930

d (Å)	I	h	k	l	Comments
5.89485	4	0	1	0	
4.01700	1	1	1	0	
3.06834	100	1	1	1	Strongest line.
2.94590	24	0	2	0	
2.74502	23	2	0	0	
2.48826	1	2	1	0	Less than given I.
2.37674	17	2	0	1	
2.27872	1	1	2	1	
2.20320	1	0	1	2	Less than given I.
2.00781	13	2	2	0	
1.96368	2	0	3	0	
1.84937	12	0	2	2	
1.79640	13	2	0	2	
1.74765	1	3	1	0	Less than given I.
1.72320	16	1	3	1	
1.64011	15	3	1	1	
1.59791	1	2	3	0	Less than given I.
1.53363	11	2	2	2	
1.51382	1	0	3	2	Less than given I.
1.47296	12	0	4	0	
1.40768	1	3	1	2	
1.37255	1	4	0	0	
1.36275	1	1	4	1	
1.35216	1	1	2	3	Less than given I.
1.32557	1	2	3	2	
1.29812	2	2	4	0	
1.28872	3	3	3	1	
1.25196	2	0	4	2	
1.24439	2	4	2	0	
1.20317	4	1	3	3	
1.18821	2	0	0	4	
1.17374	3	3	1	3	
1.13921	2	1	1	4	
1.11975	2	1	5	1	
1.10201	3	4	2	2	
1.09023	1	2	0	4	
1.08274	1	2	5	0	

37 line(s)

Figure S6: The powder x-ray diffraction pattern of β- phase Tetragonal and corresponding XRD analysis results.